Biosynthesis of metal/metal-oxide nanoparticles and measurement of their physical, biophysical properties

Umesh Kumar

UNDER THE GUIDANCE OF

Dr. Archana Pundle
BIOCHEMICAL SCIENCES DIVISION
NATIONAL CHEMICAL LABORATORY
PUNE - 411008, INDIA

AND CO-GUIDANCE OF

Dr. Pankaj Poddar
PHYSICAL CHEMISTRY DIVISION
NATIONAL CHEMICAL LABORATORY
PUNE - 411008, INDIA

February 2011

Biosynthesis of metal/metal-oxide nanoparticles and measurement of their physical, biophysical properties

SUBMITTED TO THE

UNIVERSITY OF PUNE

FOR THE DEGREE OF

DOCTOR OF PHILOSOPHY

IN

BIOTECHNOLOGY

BY

Mr. Umesh Kumar

UNDER THE GUIDANCE OF

Dr. Archana Pundle

(Research guide)

SCIENTIST

BIOCHEMICAL SCIENCES DIVISION

NATIONAL CHEMICAL LABORATORY

PUNE - 411008

INDIA

Dr. Pankaj Poddar

(Research co-guide)

SCIENTIST

MATERIALS CHEMISTRY DIVISION

NATIONAL CHEMICAL LABORATORY

PUNE - 411008

CERTIFICATE

Certified that the work incorporated in the thesis entitled: "**Biosynthesis of metal/metal-oxide nanoparticles and measurement of their physical, biophysical properties**", submitted by Mr. Umesh Kumar, for the degree of Doctor of Philosophy, was carried out by the candidate under my supervision at the Division of Biochemical Sciences and Physical and Materials Chemistry Division, National Chemical Laboratory, Pune. Materials acquired from other sources have been duly acknowledged. To the best of my knowledge, the present work or any part thereof has not been submitted to any other University for the award of any other degree or diploma.

Date: Dr.(Mrs) Archana Pundle

Place: NCL, Pune   (Research guide)

CERTIFICATE

Certified that the work incorporated in the thesis entitled: "**Biosynthesis of metal/metal-oxide nanoparticles and measurement of their physical, biophysical properties**", submitted by Mr. Umesh Kumar, for the degree of Doctor of Philosophy, was carried out by the candidate under my supervision at the Division of Biochemical Sciences and Physical and Materials Chemistry Division, National Chemical Laboratory, Pune. Materials acquired from other sources have been duly acknowledged. To the best of my knowledge, the present work or any part thereof has not been submitted to any other University for the award of any other degree or diploma.

Date: Dr. Pankaj Poddar

Place: NCL, Pune   (Research Co-guide)

DECLARATION

I hereby declare that the work incorporated in this thesis entitled **"Biosynthesis of metal/metal-oxide nanoparticles and measurement of their physical, biophysical properties"** submitted for the degree of *Doctor of Philosophy in Biotechnology* has been carried out by me at the Biochemical Sciences and the Materials Chemistry Divisions of the National Chemical Laboratory, Pune, India under the joint supervision of Dr. (Mrs.) Archana Pundle and Dr. Pankaj Poddar. Materials acquired from other sources have been duly acknowledged in this thesis. The work is original and has not been submitted in part or full by me for award of any other degree or diploma in any other University.

Date: **Umesh Kumar**

Place: NCL, Pune   (Research Student)

Acknowledgement

It gives me a great pleasure to thank all those who were associated with me during my Ph.D. at National Chemical Laboratory. The work described in this thesis would not have been possible without these people because they were involved directly or indirectly. Therefore I would like to extend my sincere thanks and gratitude towards these people who were there with me during my tenure at National Chemical Laboratory.

First and foremost among them is my research advisor and research co-guide Dr. Pankaj Poddar whose constant support and guidance has been always precious to make this thesis possible. His valuable suggestions and fruitful discussions made significant contribution to make this thesis feasible. I am also thankful to him for providing me an opportunity to get hands on exposure to hi-tech instruments like Atomic Force microscopy, Ellipsometry, Dynamic light Scattering, Small angle X-ray scattering etc. which has opened a new horizon to my future research.

I would also like to thank my research guide Dr. Archana Pundle, without her support this thesis would not have completed. I am thankful for her regular guidance, encouragement, cooperation and appreciation. I would like to thank her deep from my heart for all the help and moral support that she has provided throughout, especially in latter part of my research work.

I express my gratitude to Dr. Absar Ahmad for providing me accessibility to his lab facilities even during odd hours as well as for our fruitful discussions. I thank Dr. Asmita Prabhune for encouragement and support during my work. My sincere thanks to Dr. B. L. V. Prasad and Prof. Satish Ogale for their continuous support, friendly nature, elderly advice and scientific interactions.

I would also like to extend my sincere thanks to Mrs. Suguna Adhyanthaya for helping me at NCL in all the official activities and for her elderly advice irrespective of my work commitments, thinking about my betterment always. Her help in TGA and

Table of Contents

Chapter 3: Measurement of biophysical properties of bacterial cells under stress due to the exposure to Cobalt acetate during microbial synthesis of Co_3O_4 nanoparticles

Chapter 4: Lysozyme mediated size controlled synthesis of antimicrobial, biocompatible noble metal (Au and Ag) nanoparticles

Chapter 5: Lysozyme mediated aqueous phase synthesis of chromium (IV) oxide at ambient conditions

Chapter 6: Conclusions

Annexure-1 Microbiological media and Phylogenetic tree

Annexure-2 Mammalian cell culture media

Annexure-3 List of Publications
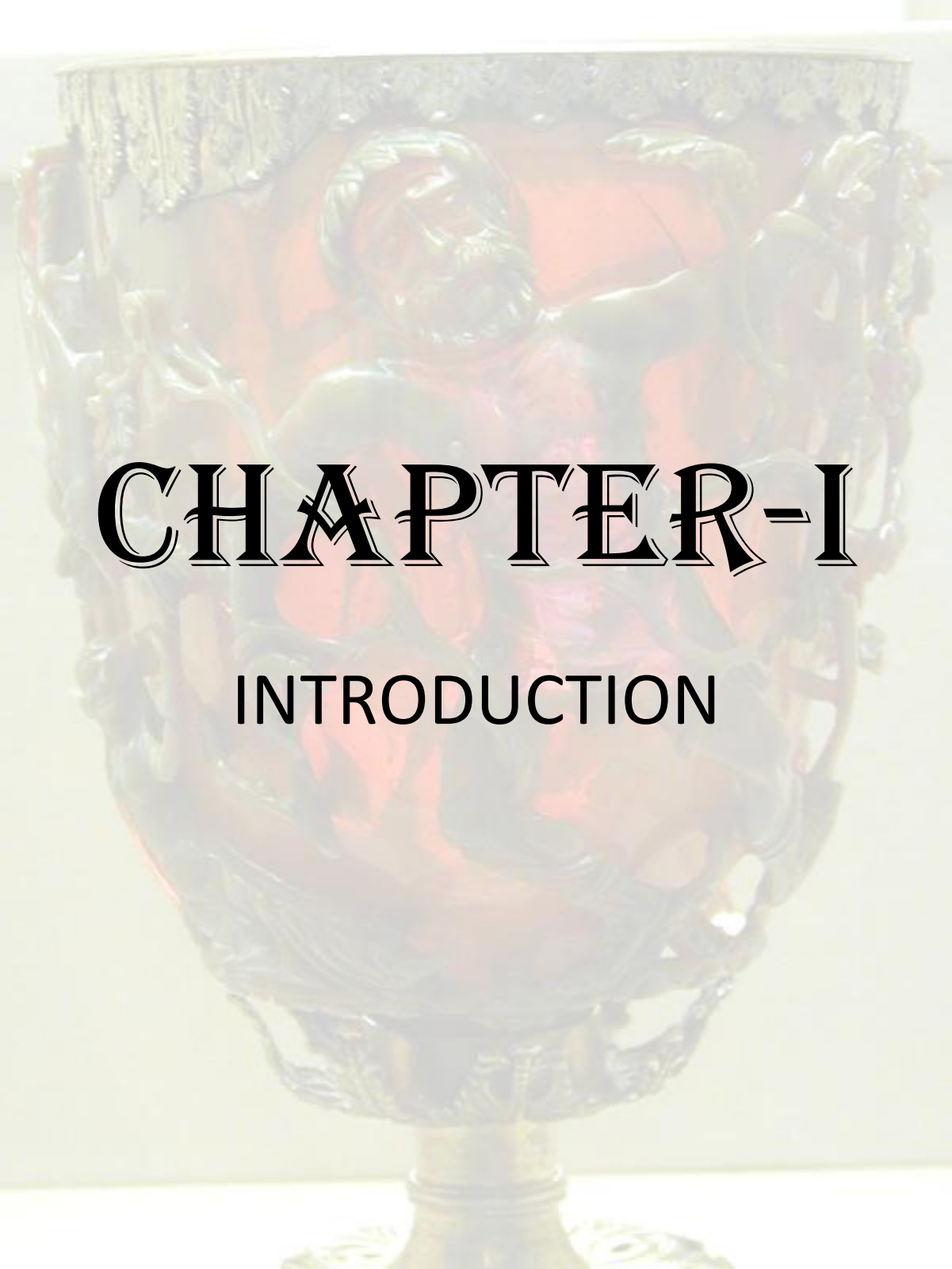
CHAPTER-I

INTRODUCTION

Introduction

(Images courtesy: Various sources at http://images.google.com)
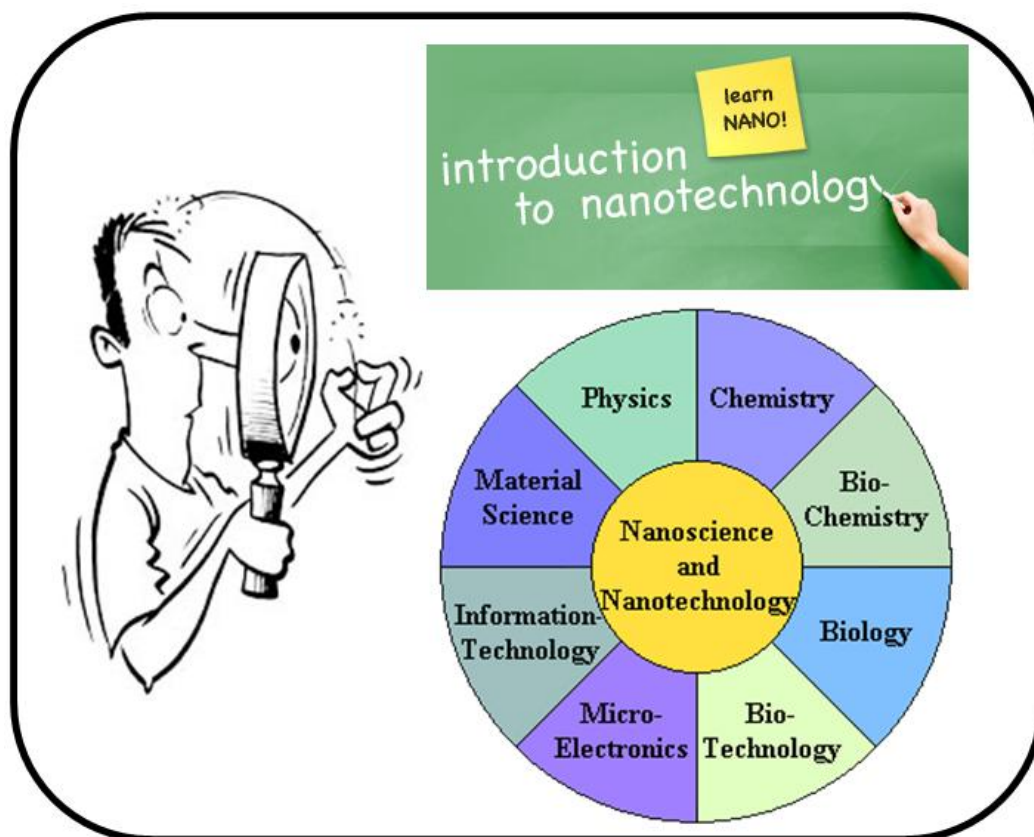
This chapter deals with brief introduction to the big realm of nanobiotechnology and the kind of work presented in this thesis which starts with the motivation for work, followed by an overview of biomineralization processes occurring in nature. The syntheses of various biomaterials in their natural habitats and their specific biological role has been discussed. Various biological and biomimetic approaches currently in use for the in silico synthesis of nanomaterials have also been emphasized. The chapter also briefly describes the rationale behind the new biological methods that we have used for the biosynthesis of metal/metal-oxide nanomaterials. Finally, an outline of the chapter-wise work described in this thesis has been presented.

1. INTRODUCTION TO NANOREGIME AND THE SCIENCE THERE EXISTS

Nanoscience is the study of phenomena and manipulation of materials at atomic, molecular and macromolecular scales, where properties differ significantly from their bulk counterparts. It deals with the study of the objects and systems in which at least one dimension is less than 100 nm.

Similarly, nanotechnology can be defined as the design, characterization, production and application of structures, devices and systems by controlling shape and size at the nanometer scale. This technology uses science on the nanoscale, occurring at the level of atoms and molecules. At this level, traditional boundaries between biology, chemistry and physics get merged or indistinguishable. It is a highly interdisciplinary area because it involves ideas integrated from many traditional disciplines e.g. physics, chemistry, biology, engineering, medicine and information technology etc. The primary concept was presented on December 29, 1959, when Richard Feynman presented a lecture entitled "There's Plenty of Room at the Bottom" at the annual meeting of the American Physical Society, the California Institute of Technology.[1]
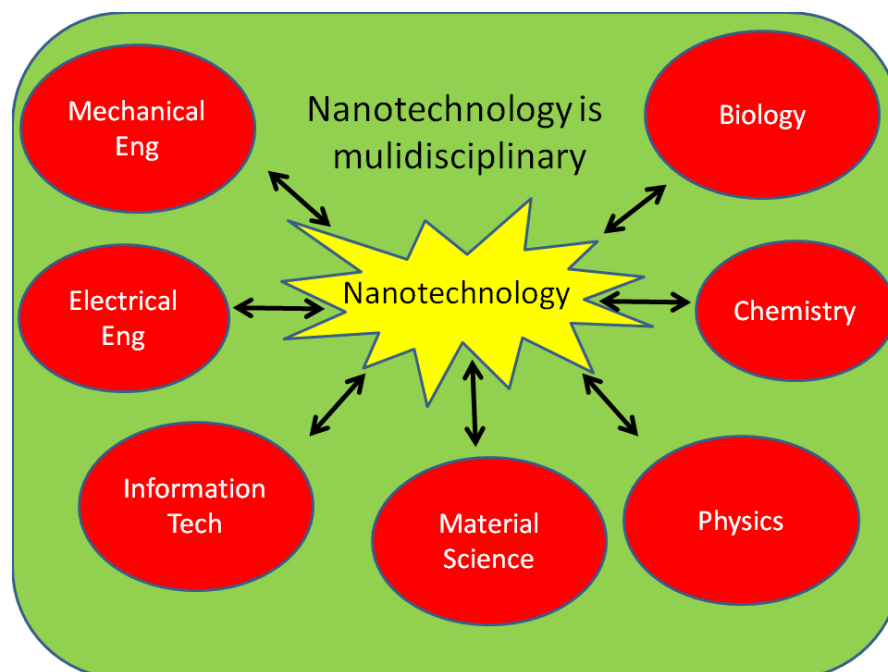
Figure 1.1: Schematic picture showing multidisciplinary nature of nanotechnology

1.1 THE "NANO"–"BIO" INTERFACE

Biosystems are governed by nanoscale processes and structures that have been optimized over millions of years. Biologists have been operating for many years at the molecular level, in the range of nanometers (DNA and proteins) to micrometers (cells). A typical protein like haemoglobin has a diameter of about 5 nm, the DNA's double helix is about 2 nm wide, and a mitochondrion spans a few hundred nanometers. Therefore, the study of any subcellular entity can be considered "nanobiology." Furthermore, the living cell along with its hundreds of nanomachines is considered, today, to be the ultimate nanoscale fabrication system.

1.2 NANOBIOTECHNOLOGY

The groundwork of each and every biological system is nanosized molecular building block and machinery that cooperates to produce living entities. These elements have ignited the imagination of nanotechnologists for many years and it is the combination of these two disciplines, nano and biotechnology, that has resulted in the birth of the new science of nanobiotechnology. Nanotechnology provides the tools and technology platform for transformation and investigation of biological systems, and biology offers inspirational models and bio-assembled components to nanotechnology.

There are two basic fabrication approaches for creating nanostructures: bottom-up and top-down. The bottom-up approach exploits biological structures and processes to create novel functional materials, biosensors, and bioelectronics for different applications. This field encompasses many disciplines, including material science, organic chemistry, chemical engineering, biochemistry, and molecular biology.

In the top-down approach, nanobiotechnology applies tools and processes of nano/microfabrication to build nanostructures and nanodevices. The tools that are used often involve optical and electron beam lithography and the processing of large materials into fine structures with defined surface features. One of the major differences in approach used for nanoparticles synthesis in nanotechnology and nanobiotechnology is that, in the former, the dominant approach is top-down, whereas in the latter, it is bottom-up. An example of the bottom-up approach is the pioneering work of two leading groups on biomolecular motor proteins.[2-7] In these

studies, naturally occurring motor proteins were engineered for compatibility with artificial interfaces to create new ways of joining proteins to synthetic nanomaterials. Unlike nonbiological systems that are fabricated top-down, the biological systems build up from the molecular level (bottom-up).
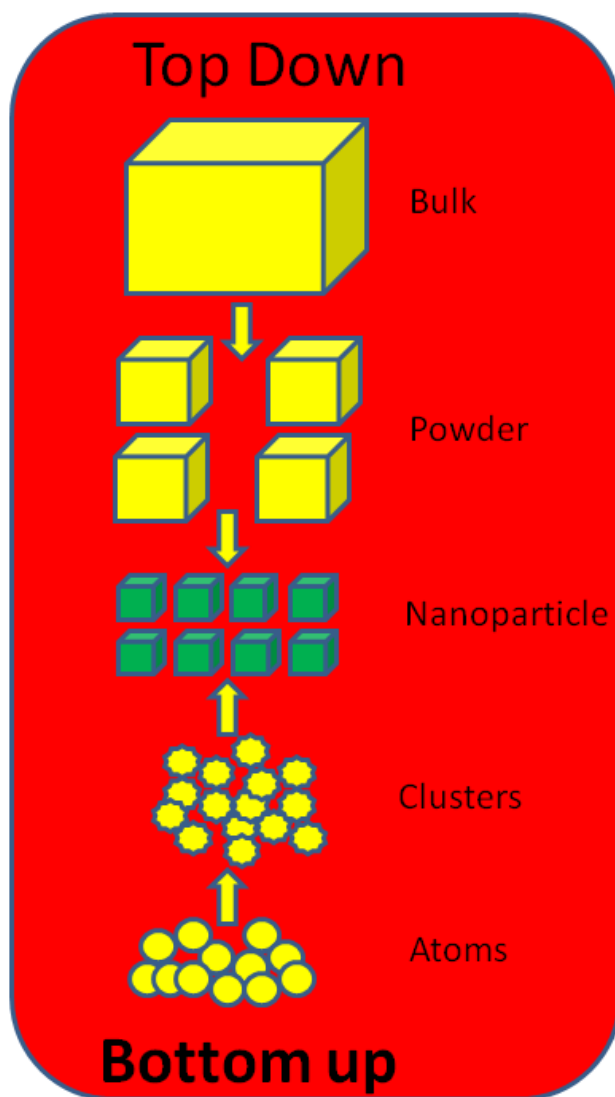
Figure 1.2: Schematic showing two basic approaches for nanoparticles synthesis

It is done this via collection of molecular tool kits of atomic resolution that are used to fabricate micro and macrostructure architectures. Biological nanotechnology, or nanobiotechnology can be viewed in many ways: one way is the incorporation of nanoscale machines into biological organisms for the ultimate purpose of improving the organism's quality of life. Another way is the use of biological "tool kits" to construct nano- to microstructures. However the broad perspective is probably the

one that will include both and will be defined as: **the engineering, construction, and manipulation of entities in the 1 to 100 nm range using biologically based approaches or for the benefit of biological systems**. The biological approaches can be either an inspired way of mimicking biological structures or the actual use of biological building blocks and building tools to assemble nanostructures. Our main emphasis will be on the different biological approaches to synthesize metal/metal oxide nanoparticles and their property measurements which will be discussed throughout this chapter.

Typical examples of bottom–up synthesis of nanomaterials can be observed in Nature, which have been discussed in the later part of this chapter. During efforts towards creation of miniaturized materials, it has been realized that materials in nano–dimensions usually exhibit properties that are very different from their bulk counterparts. Increasing knowledge about the unique properties of nanoparticles has led to renewed interest in their potential applications. Nanoparticles have been around for a long time; presumably the first nanoparticle was recognized in 1570 with aurum potable (potable gold) and luna potable (potable silver) which alchemists used as elixirs.[8-11] One of the oldest applications of nanoparticles that we come across in literature is the use of gold nanoparticles for staining glasses; a famous example is the Lycurgus cup that dates back to 4th century AD.[12-14] Nowadays it is becoming more and more evident in the form of potential applications of nanoparticles, which extend to wide-ranging areas such as catalysis[15,16], biosensors[17-20], diagnostics[21], cell labelling[22-24], solar cells[25,26], fuel cells[27], photonic band gap materials[28], single electron transistors[29,30], non-linear optical devices[2,31-33], information storage[34], refrigeration[35], chemical/optical computers[36], harder metals[37], surface enhanced Raman spectroscopy[38], self cleaning paints[39], environmental clean up[40-46], and improved national security [47,48] to name a few and the list goes on.[39] The realization of their various potential applications is only limited by our imagination.[49-54] A remarkable aspect of nanomaterials is that a number of factors can influence their physical, chemical, optical, electronic and magnetic properties. The factors that can strongly modulate their properties include their size[55-60], shape[61-63], surface composition[64-67], dielectric environment[68-71] and the interparticle interactions.[72-76] Such remarkable variations in properties of nanomaterials are due to their dimensions being comparable to the de Broglie wavelength of the charge carriers, which modify their properties significantly.[77,78] One of the readily

perceptible properties in case of metal nanoparticles is their colour. The colour of metal nanoparticles originates due to surface plasmons *i.e.* the coherent charge density oscillations.[79] Surface plasmon is a special phenomenon, which is observed in metal nanoparticles at nanoscale. It is a dimension below 100 nm, where properties such as melting point, colour (i.e. band gap and wavelength of optical transitions), ionisation potential, hardness, catalytic activity and selectivity, or magnetic properties such as coercivity, permeability and saturation magnetisation, which we are used to thinking of as constant, vary with size. We basically distinguish two types of variations as a function of size:

• Scalable effects: Energy levels or properties of surface atoms are different from bulk atoms. As the particle size increases, the surface-to-volume ratio decreases which is inversely proportional to the particle size. Thus, all properties which depend on the surface to-volume ratio keep changing and extrapolate slowly to bulk values.

• Quantum effects: When the molecular electronic wave function is delocalised over the entire particle then a small, molecule-like cluster has discrete energy levels so that it may be regarded like an atom (sometimes called a super atom). The simplest model for it is that of a particle in a box. Adding more atoms to the cluster changes the size of the box continuously so that the energy levels close up to some extent. More importantly, adding more atoms means adding more valence electrons to the system. Thus whenever a shell of sometimes multiple degenerate energy levels is filled the next electron has to be accommodated in the next shell of higher energy. The situation is analogous to the evolution of properties with increasing atomic number in the periodic table. Filled shells represent a particularly stable configuration. Properties such as ionisation potential and electron affinity are well known to display a discontinuous behaviour as one moves along the periodic table. For clusters consisting of atoms with strongly overlapping atomic orbitals, i.e. for metals and semiconductors the situation is analogous. As a consequence, the developments which were initially concerned with metal nanoparticles led to the realization that essentially all solid materials in nanoscale would be of interest.

The science of ceramic/oxide nanoparticles is no exception and this area of nanoscience is exciting due to the fact that many of the ceramic systems of interest have been studied extensively in the bulk form and therefore provide ready comparisons with nanoparticulate systems.[80] A beneficial consequence of the reduced size of oxide nanoparticles, and for that matter for all the nanoparticle

systems, is the large increase in the surface to volume ratio of the nanomaterials in comparison with their bulk counterparts. Because of the huge number of atoms at the surface and their limited availability within the lattice, the chemistry of oxide nanoparticles is greatly affected by the defect sites present both within the lattice (point defects) as well as on the surface (planar defects). Point defects arise either due to the absence of the constituent atoms/ions on the lattice sites or their presence in interstitial positions. Even the presence of foreign atoms/ions in the lattice causes point defects. These point defects result in the displacement of neighbouring atoms/ions because of the polarization in surrounding region, and hence modify the crystal lattice. However, since the creation of point defects is generally an endothermic process, the intrinsic defect concentration in binary oxides is extremely low (~ 10–5 at around 0.8 Tm). On the other hand, the surface of oxide nanocrystals constitutes considerable amount of planar two dimensional defects in the form of grain boundaries, stacking faults and crystallographic shear planes. These extrinsic defects lead to tilt boundaries (array of period space or edge dislocations), twist boundaries (array of screw dislocations), twin boundaries (a layer with mirror plane symmetry with respect to the rotation of one part of the crystal, on a specific plane, with respect to another) and/or antiphase boundaries (across which the sublattice occupation becomes interchanged) in nanooxides. The highly ionic nature of some materials, especially Co_3O_4, CrO_2, TiO_2, ZrO_2, MgO and Al_2O_3, further promote the formation of many stable defect sites, including edges, corners, and anion/cation vacancies. Different morphologies of oxide nanomaterials may also alter their surface chemistry and adsorption characteristics, hence imparting important properties.[46]

However, an intricate yet fascinating consequence of the size and defect dependent applicability of nanomaterials is that the properties of nanocrystals obtained by various routes cannot be generalized, since various synthesis routes may lead to altering defect conditions in these nanocrystals. The display of unique properties by the nanoparticles that can be controlled by many external and internal factors and the scope for diverse applications makes the synthesis of such nanomaterials extremely important and therefore a number of routes for synthesis of nanomaterials being evolved (Figure 1.3). So far synthesis of inorganic
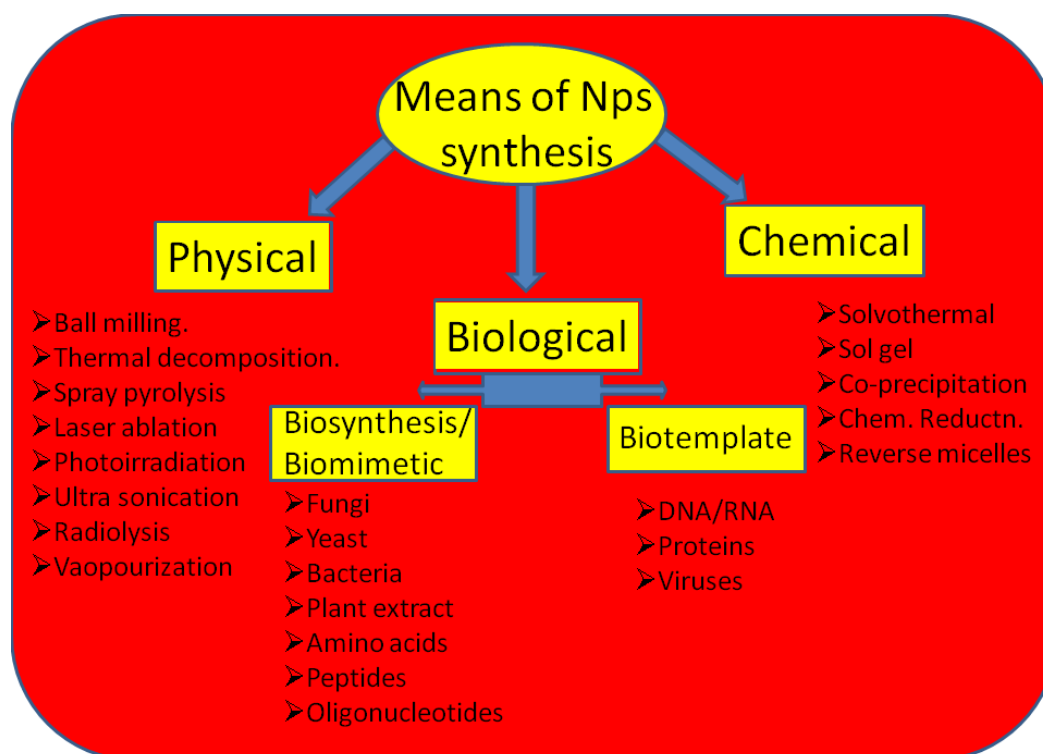
Figure 1.3: Schematic presentation showing different routes for nanoparticle synthesis

nanomaterials has been demonstrated mainly by physical and chemical means. Various physical routes leading to successful synthesis of nanophase materials, especially oxide powders are vapour condensation techniques[81-88], spray pyrolysis[89-94], thermochemical decomposition of metal–organic precursors in flame reactors[95-98] and other aerosol processes which are named after the energy sources applied to provide the high temperatures during gas–particle conversion. The Liquid phase chemical methods for the synthesis of inorganic nanoparticles including metal oxides have received wider acceptance than physical methods and are the most commonly followed route. This increasing interest in chemical processing of nanoscale particles of metal oxides and other materials is clearly indicated by the number of reports and reviews on this subject.[99-108] Chemically, inorganic nanoparticles can be synthesized by reduction or oxidation of metal ions or by precipitation of the necessary precursor ions in solution phase. The control on size, shape, stability and the assembly of nanoparticles is achieved by incorporating different capping agents, solvents and templates. Capping agents that have been used, range from simple ions to polymeric molecules and even biomolecules.[109-114] As a solvent, though water is largely used,

the use of organic solvents,[115,116] ionic liquids[117] and supercritical fluids[118,119] has also been demonstrated. Similarly many soft and rigid templates such as micelles,[120-122] polymeric molecules,[123,124] DNA,[125,126] Tobacco Mosaic Virus,[127-129] mesoporous materials and many more including preformed nanoparticles[130] have been employed to get control over the formation and assembly of nanoparticles. Evidently, nanoparticle synthesis has gained due focus and the scope for new synthesis methods has been increasing constantly with innovative contributions. Though the chemical and physical routes of nanomaterials synthesis have principally dominated the nanosphere, recently there is a growing attention towards the use of advantageous biological means for nanoparticle synthesis. The following sections of this chapter focus on biological routes to nanomaterials synthesis with brief introductions to:

1) Rationale behind thesis work

2) Biomineralization in natural environment

3) Biomimetic approaches for mimicking natural biomineralization

4) Imitating Nature's way of biomineralization *in situ*

1.3 Nature: Motivation for Nanomaterials Synthesis

The morphological diversity and complexity of naturally occurring forms and patterns has been the motivation for human to copy Nature and to adapt the ideas from Nature to achieve functional, aesthetic, and societal value.[131] Magnetotactic bacteria, for example, are able to form nanometre-sized, membrane-bound magnetic iron minerals, magnetite (Fe_3O_4) or greigite (Fe_3S_4), with narrow size distributions and high magnetic moments. However in vivo this synthesis is typically limited to certain materials which includes magnetite, silica, or calcium carbonate.

These materials combine complex morphology over several hierarchy levels with superior material properties and environment friendly synthesis and biocompatibility. This makes them very attractive archetypes for materials chemists. To mimic the synthesis of these material the goal is not to simply emulate a particular biological architecture or system, but to abstract the guiding principles and ideas and use such knowledge for the preparation of new synthetic materials.[132]

1.4 Biomineralization: A Phenomena that Existed in Nature since Ages

The course of evolution on our planet has resulted in the appearance, diversification, and proliferation of organisms capable of producing complex structures from hard inorganic materials, via processes collectively known as biomineralization.[133-136] For example, magnetotactic bacteria produce nanoparticles of Fe_3O_4 or Fe_3S_4 that have well-defined sizes and shapes that enable these microorganisms to utilize magnetic fields for alignment and migration.[134,135,137,138] Fish grow structures, known as otoliths or "ear stones", within the inner ear that assist in inertial sensing.[135,139] These otoliths are composed of the aragonite polymorph of calcium carbonate.[135,139] Remarkably the mollusks produce shells that contain a distinct crystalline form of calcium carbonate such as aragonite, or may contain segregated layers of calcite and aragonite.[133,140] In addition to the crystalline forms of calcium carbonate, an amorphous phase of this mineral is synthesized by sea urchins to produce spines (spicules).[141] Marine sponges produce silica spicules that have been demonstrated to possess light-guiding characteristics and may reach lengths up to 3 m.[135,142-146] The diatoms, a type of unicellular eukaryotic algae, produce intricately detailed silica cell walls, known as frustules, that are organized over multiple length scales.[134,135,147] In each of the examples listed above, specialized biomolecules have been found, or are thought, to play a major role in directing the formation of these often complex inorganic structures.[134,135]

Biominerals are most often considered in either their more traditional roles as critical structural components of organisms (e.g., teeth, the siliceous shell of diatoms) and important ion reservoirs for cellular function (Ca^{2+} and bone) or in their highly evolved functional roles (e.g., magnetotactic sensing, buoyancy/balance regulation). Increasingly, it is becoming apparent that biominerals also play an important protective role by acting as critical detoxification sinks within certain organisms. Thus, organisms ranging from protozoa to eukaryotes utilize the same principles of biomineralization (cellular processing, supramolecular organization, and interfacial recognition) to form such materials as Abalone nacre to efficiently remove potentially toxic species from their immediate environment. Thus the understanding how biological systems exert their nanoscale control over structural biominerals has revealed important biomimetic routes to novel materials synthesis.

A variety of minerals are synthesized in Nature and they can be traced to various groups of organisms including plants, animals and microorganisms (Table 1.1). The component that perhaps distinguishes natural materials from synthetic materials is the presence of biomacromolecules as an intimate mix with the mineral phases at all the different hierarchical levels, starting at the nanometer scale. It was recognized that many of these macromolecules have a common chemical attribute that they are rich in carboxyl groups.[148,149] These may be the constituents of protein and/or polysaccharide moieties. Many of these macromolecules also possess phosphate and/or sulfate groups in addition to the carboxyl groups. The presence of all these charged groups makes these macromolecules excellent candidates for interacting with the mineral ions in solution or with the surfaces of the solid phase.[148,149]

Table 1.1 Various biominerals and their roles in biological systems[150-155]

Biogenic minerals	Biological system	Biological location	Biological function
Calcium carbonate (calcite, vaterite, aragonite)	Plants, aves, mammals, many marine organisms, coccoliths	Mollusk shell, eye lens, crab cuticle, egg shells, leaves, inner ear	Exoskeleton, optical, mechanical strength, protection, gravity receptor, buoyancy device, calcium storage [156-160]
Calcium phosphate (hydroxyapatite, dahllite, octacalcium phosphate)	Mammals, fish, bivalves	Bone, teeth, scales, gills, gizzard plates, Mitochondria	Endoskeleton, ion store, cutting/grinding, protection

Iron oxides (magnetite, greigite, goethite, lepidocrocite,	Bacteria, algae, dinoflagellates, chitons, trouts, euglena, human brain, salmons	Intracellular, teeth, head, filaments, ferritin protein	Magnetotaxis, magnetic orientation, mechanical strength, iron
Sulfates (gypsum, celestite, barite)	Jellyfish, acantharia, loxodes, chara, photosynthetic	Statoconia, cellular, intracellular, tatoliths	Gravity receptor, skeleton, gravity device/receptor [173]
Silicon oxides (amorphous silica)	Diatoms, radiolarians, sponges, plants, microbes, etc.	Cell wall, cellular, leaves	Exoskeleton, protection, Mechanical support, plant nutrient, resistance against pests and predators [174]

The biological systems have been using biomineralization (Table 1.2) as a type of detoxification mechanism for noble metals for over 2.8 billion years[175], as witnessed by placer gold deposits around the world. Noble metals such as silver and gold are naturally found in sea water, soil, and rocks in nanogram to microgram levels. While silver and gold are not the most reactive metals on the periodic table, they are able to act as electron sinks disrupting vital respiratory enzymes and electron transport within organisms. Silver can also block the permeability of the outer membrane, inhibiting growth.[176,177] As a result, trace amounts of these metals can have detrimental effects on an organisms. Biomineralization detoxification of silver and gold metal ions can be accomplished by way of three different modes: intracellular, extracellular, and intercellular.

Table 1.2 Summary of noble metal biomineralization as a detoxification mechanism for nanoparticle synthesis

Organism	Species	Product	Size (nm)	Shape	Location
Actinomycete	*Rhodoccous* sp.	Au	5–16	Spherical	Intracellular
Bacteria	*Pseudomonas stutzeri* AG259	Ag	2–200	Hexagonal, triangular	Intracellular
Fungus	*Verticillium* sp.	Au	12–28	Spherical	Intracellular
Fungus	*Verticillium* sp.	Ag	13–27	Spherical	Intracellular
Fungus	*Fusarium oxysporum*	Au	20–40	Spherical, triangular	Extracellular
Fungus	*Fusarium oxysporum*	Ag	5–50	Spherical, triangular	Extracellular
Actinomycete	*Thermomono-spora* sp.	Au	7–12	Spherical	Extracellular
Plant	*Pelargonium graveolens*	Au	20–40	Rods, triangular, spherical	Extracellular
Plant	*Pelargonium graveolens*	Ag	16–40	Spherical, ellipsoidal	Extracellular
Plant	Alfalfa	Au	2–20	Spherical	Intercellular
Plant	Alfalfa	Ag	2–20	Spherical	Intercellular

1.5 Biomimetic mineralization

Harnessing nature's synthetic machinery is an exciting approach to nanosynthesis that embodies principles of green chemistry. It creates intricate nanostructures with tunable properties using materials found in local surroundings and it carefully crafts devices, protective armor, lighting, and energy vessels with highly efficient materials

use. Materials scientists, engineers, physicists, and chemists have turned to nature to understand the mechanisms and to develop clean, green nanomaterials through biomimetic and biosynthetic approaches. One of the key tenets of biology is the ability of biomolecules to self assemble into supramolecular structures. This intrinsic ability has piqued the interest of scientists and engineers to develop a bottom-up approach to nanofabrication. Biological self assembly occurs at the molecular scale and is often reversible, self-correcting, and self-healing. The shape and size of self assembled structures are intricately controlled on the nanoscale. Thus, understanding these mechanisms can open doors for development of a wide variety of new materials from self-healing fibres for wound repair to faster, smaller computer devices. Understanding how biology self-assembles structures can also lead to synthetic methods for creating supramolecular structures, using nature's blueprints to create synthetic nanomaterials.

Some organisms have the capability to take up minerals from their surrounding environment and create intricate inorganic-organic hybrid structures that possess remarkable nanoscale properties. Bone, teeth, and seashells are just a few examples that utilize calcium carbonate to make hard composites. Some unicellular organisms make exoskeletons: coccolithophores create exoskeletons using calcium carbonate much like seashells, and diatoms produce shells from amorphous silica. Calcium carbonate producing animals are under intense investigation in the hopes of producing artificial bone or dental composites.

Several methods exist for controlling the size and shape of nanoparticles. For example, nature creates nanoparticles of very defined shapes and sizes using genetic control. We can exploit similar biomechanisms to create nanoparticles using biological molecules or organisms as precursors or seeds for growth. To date, whole organism systems have been used to produce metallic nanoparticles, although some limited studies have begun to explore fabrication of Ge[178] in bioreactors or Ti from purified biological macromolecules.[179] Nevertheless, attempts have been made to ascertain which organic components of microorganism are responsible for directing crystal growth. Proteins, polysaccharides, lipids, peptides, and amino acids are among the most studied organic biomolecules responsible for directing crystal growth and can be considered capping agents in production of nanocrystals. Proteins and polysaccharides have been partially purified from the marine organisms that direct calcium carbonate crystallization in the production of exoskeletons. [180,181]

Proteins responsible for silica deposition in diatoms[182] and sponge spicules[183] have been well characterized, and in many cases recombinant proteins have been produced. These biological macromolecules are under genetic control and can potentially be used to fabricate novel nanostructures.

1.6 Biomineralization *in situ*: Nature's Way

The interest in inorganic nanoparticles is growing tremendously as they provide superior material properties with functional versatility. Due to their size features and advantages over available chemical imaging drugs and drug agents, the inorganic nanoparticles have been considered as potential tools for medical imaging as well as for treating diseases. Inorganic nanomaterials have been widely used for cellular delivery due to their versatile features like wide availability, rich functionality, good biocompatibility, capability of targeted drug delivery and controlled release of drugs.[184] For example mesoporous silica when combined with molecular machines prove to be excellent imaging and drug releasing systems. Gold nanoparticles have been used extensively in imaging, as drug carriers and in thermo therapy of biological targets[185]. Inorganic nanoparticles (such as metallic and semiconductor nanoparticles) exhibit intrinsic optical properties which may enhance the transparency of polymer- particle composites. For such reasons, inorganic nanoparticles have found special interest in studies devoted to optical properties in composites. For instance, size dependant colour of gold nanoparticles has been used to colour glass for centuries.[186]

1.7 Strategies used to synthesize nanoparticles

Traditionally nanoparticles were produced only by physical and chemical methods. Some of the commonly used physical and chemical methods are ion sputtering, solvothermal synthesis, reduction and sol gel technique. Basically there are two approaches for nanoparticle synthesis namely the Bottom up approach and the Top down approach. In the Top down approach, scientists try to formulate nanoparticles using larger ones to direct their assembly. The Bottom up approach is a process that builds towards larger more complex systems by starting at the molecular level and maintaining precise control of molecular structure.

1.7.1 Physical and chemical methods of nanoparticle synthesis

Some of the commonly used physical and chemical methods include:

a) Sol-gel technique, which is a wet chemical technique used for the fabrication of metal oxides from a chemical solution which acts as a precursor for integrated network (gel) of discrete particles or polymers. The precursor sol can be either deposited on the substrate to form a film, cast into a suitable container with desired shape or used to synthesize powders.

b) Solvothermal synthesis, which is a versatile low temperature route in which polar solvents under pressure and at temperatures above their boiling points are used. Under solvothermal conditions, the solubility of reactants increases significantly, enabling reaction to take place at lower temperature.

c) Chemical reduction, which is the reduction of an ionic salt in an appropriate medium in the presence of surfactant using reducing agents. Some of the commonly used reducing agents are sodium borohydride, hydrazine hydrate and sodium citrate.

d) Laser ablation, which is the process of removing material from a solid surface by irradiating with a laser beam. At low laser flux, the material is heated by absorbed laser energy and evaporates or sublimates. At higher flux, the material is converted to plasma. The depth over which laser energy is absorbed and the amount of material removed by single laser pulse depends on the material's optical properties and the laser wavelength. Carbon nanotubes can be produced by this method.

e) Inert gas condensation, where different metals are evaporated in separate crucibles inside an ultra high vacuum chamber filled with helium or argon gas at typical pressure of few hundred pascals. As a result of inter atomic collisions with gas atoms in chamber, the evaporated metal atoms lose their kinetic energy and condense in the form of small crystals which accumulate on liquid nitrogen filled cold finger. E.g. gold nanoparticles have been synthesized from gold wires.

1.7.2 Biosynthesis of nanoparticles

The need for biosynthesis of nanoparticles arose as the physical and chemical processes were costly. So in the search of for cheaper pathways for nanoparticle synthesis, scientists used microorganisms and then plant extracts for synthesis. Nature has devised various processes for the synthesis of nano- and micro scaled

inorganic materials which have contributed to the development of relatively new and largely unexplored area of research

based on the biosynthesis of nanomaterials.[187]

Biosynthesis of nanoparticles is a kind of bottom up approach where the main reaction occurring is reduction/oxidation. The microbial enzymes or the plant phytochemicals with anti oxidant or reducing properties are usually responsible for reduction of metal compounds into their respective nanoparticles.

In the preparation of nanoparticles, three main steps to be evaluated from a green chemistry perspective are, the choice of the solvent medium, the choice of an environmentally benign reducing agent and the choice of a non toxic material for the stabilization of the nanoparticles. Most of the synthetic methods reported to date rely heavily on organic solvents due to the hydrophobicity of the capping agents used.[188] Synthesis using microorganisms is in agreement with the green chemistry principles as

(i) microorganism **(ii)** the reducing agent and **(iii)** the capping agent employed in the reaction are eco-friendly.[189]

Often chemical synthesis methods lead to the presence of some toxic chemical species adsorbed on the surface of nanoparticles that may have adverse effects in medical applications[190]. This possibility when it comes to biosynthesized nanoparticles as they are eco friendly and biocompatible for pharmaceutical applications.

1.7.2.1 Use of organisms to synthesize nanoparticles

Biomimetics refers to applying biological principles for materials formation. One of the primary processes in biomimetics involves bioreduction. Initially bacteria were used to synthesize nanoparticles and this was later succeeded with the use of fungi, actinomycetes and plants.
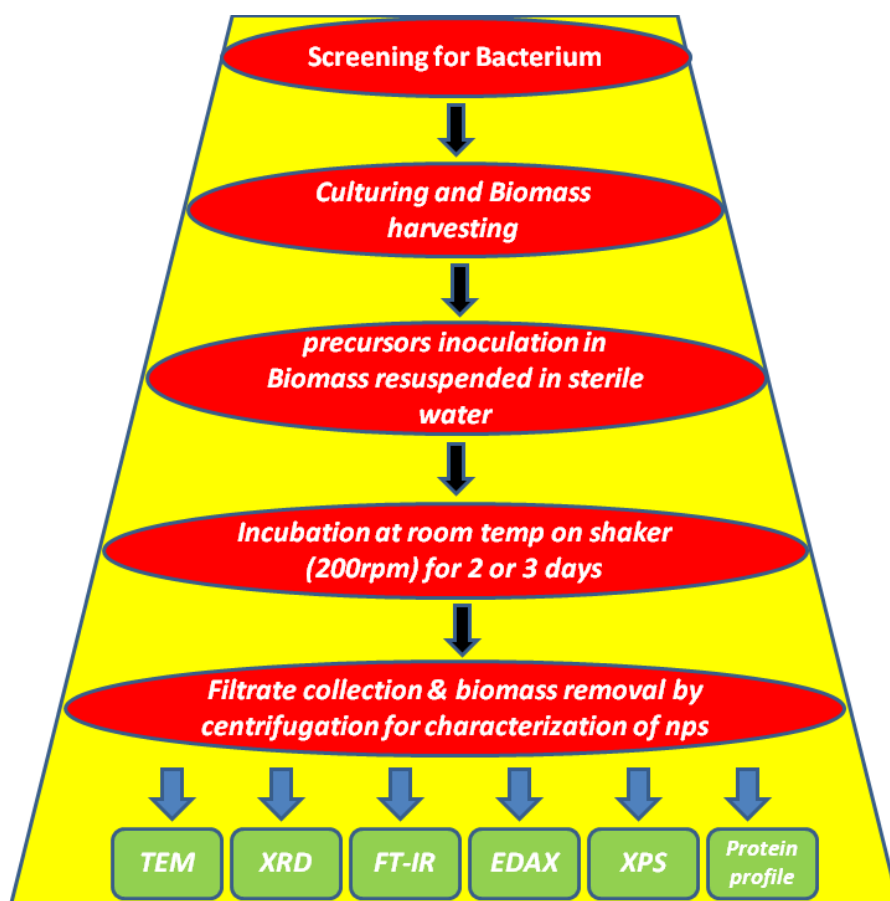
Figure 1.4: Schematic diagram showing different steps involved in biosynthesis of nanoparticles and their characterization

Here we have tried to list the names of nanomaterials synthesized by biosynthetic route using either whole organism or extracts (plants).

Table 1.3 Use of various biological entities in the production of nanoparticles

Biological entity	Nanoparticles	Size	Extracellular/ intracellular
Avena sativa (Plant)	Au	5–20 nm (at pH 3 and 4), 25–85 nm (at pH 2)	Intracellular
Azadirachta indica (Plant)	Ag, Au and Ag/Au	50–100 nm	Extracellular
Emblica Officinalis (Plant)	Ag and Au	(10–20 nm) and (15–25 nm)	Extracellular

Aloe vera (Plant)	Ag	15.2 ± 4.2 nm	
Alfalfa (Plant)	Ti/Ni bimetallic	1–4 nm	
Pelargonium graveolens (Plant)	Ag	16–40 nm	Extracellular
Cinnamomum camphora (Plant)	Au and Ag	55–80 nm	Extracellular
Tamarind Leaf Extract (Plant)	Au nanotriangles	20–40 nm	Extracellular
Aspergillus fumigatus (Fungus)	Ag	5–25 nm	Extracellular
Colletotrichum sp. (Fungus)	Au	20–40 nm	Extracellular
Verticillium. luteoalbum (Fungus)	Au	Few to 100 nm	Intracellular
Trichothecium sp. (Fungus)	Au		Extracellular And Intracellular
Verticillium sp. (Fungi)	Au and Ag	20 nm, 25 ± 12 nm	Intracellular
Fusarium oxysporum and	Magnetite	20–50 nm	Extracellular
Fusarium oxysporium	Ag,Au,CdS,ZrO$_2$,BaTiO$_3$,	Ranging from 3-40 nm	Extracellular
Candida glabrata (Yeast)	CdS	20 A°	Intracellular
MKY3 (Yeast)	Ag	2–5 nm	Extracellular
Schizosaccharomyces pombe (Yeast)	CdS	Different sizes	Intracellular
P. jadinii (Yeast)	Au	Few to 100 nm	Intracellular

Desulfovibrio desulfuricans	Palladium		
Magnetotactic bacteria	Magnetic (Fe$_3$O$_4$),		
Pseudomonas stutzeri	Ag	Up to 200 nm	
Rhodococcus sp.(Actinomycete)	Au	5–15 nm	Intracellular
Thermomonospora sp.	Au	8 nm	Extracellular
Plectonema boryanum UTEX485	Octahedral Au platlets	6 μM to 10 nm	At the cell wall

1.8 Outline of the Thesis

The work presented in this thesis describes the biosynthesis of metal/metal-oxide nanoparticles using both whole cell organism (*Brevibacterium casei*) and biomolecular approach in an attempt to extend the biological synthesis protocols towards a possibility of scale-up. An important outcome of this approach is that a range of metal/metal-oxide   (Co$_3$O$_4$, CrO$_2$, Au and Ag) nanoparticles can be synthesized using this route. These nanoparticles possess unusual yet interesting functional properties. An attempt has been made to probe the changes in biomechanical properties associated with bacterium (*Brevibacterium casei*) during cobalt oxide (Co$_3$O$_4$) nanoparticles synthesis using Atomic Force Microscopy. Further the lysozyme synthesized metal (gold and silver) nanoparticles have been shown to retain their antimicrobial activity after synthesis. They are tested and found to be biocompatible. The chapter-wise discussion of these studies is as follows:

Chapter 2 discusses the extracellular bacterial synthesis of Cobalt oxide (Co$_3$O$_4$) nanoparticles at room-temperature in aqueous environment. These sub–10 nm nanoparticles could be synthesized under ambient conditions by reaction of marine bacterium *Brevibacterium casei* with appropriate chemical precursors for 72 hours. The bacterial proteins involved in the oxidation of precursors to yield oxide

nanoparticles were investigated and involvement of low molecular weight proteins of *ca.* 30–65 kDa in the biosynthesis process was established. In addition, single crystalline, sub–10 nm cobalt oxide nanocrystals was observed for the first time in case of biologically synthesized spinel compounds.

Chapter 3 discusses the use of AFM force-distance curves on bacterial cells, to directly monitor (in real time) the changes in the surface-topography, surface-adhesion, indentation-depth, and Young's modulus of a metal-tolerant marine bacterium, *Brevibacterium casei*, isolated from the coast of the Arabian Sea, after its exposure to the Co^{2+} during the process of biosynthesis of nanoparticles. This chapter describes significant changes in the morphology as well as elastic and adhesive properties of the *Brevibacterium casei*, where an increase in the adhesive properties and the indentation depth of the bacterial surfaces and a decrease in the cell stiffness after several hours of exposure to the cobalt acetate were observed. We have discussed both qualitative and quantitative analysis of the force-spectroscopy data in detail in this chapter.

Chapter 4 discusses the lysozyme mediated size dependent synthesis of gold and silver nanocrystals at controlled pH and light conditions without using any known reducing agents. As-synthesized lysozyme capped gold nanoparticles prepared by this method are biocompatible and retain antibacterial property. Further we have shown the possible involvement of tyrosine and tryptophan residues and the use of Surface Enhanced Raman Spectroscopy (SERS) technique to precisely determine the functional groups responsible in the surface capping of gold and silver nanoparticles synthesized by the hen egg white lysozyme.

Chapter 5 discusses the lysozyme mediated synthesis of chromium oxide (CrO_2) nanocrystals in aqueous conditions without using any known reducing agents. Being metastable, presence of few nm thick layer of $Cr(OH)_3$ was observed at the surface of CrO_2. As-synthesized lysozyme capped nanoparticles prepared by this method are paramagnetic and sub 10 nm in size. In this synthesis procedure lysozyme acts both as reducing as well as capping agent.

Chapter 6 includes a brief summary of the thesis work and the scope for possible further research in these areas.

1.9 References

1. http://www.zyvex.com/nanotech/feynman.html.

2. Hess, H.; Vogel, V. *J Biotechnol* **2001**, *82*, 67.

3. Hess, H.; Bachand, G.; Vogel, V. *Chemistry* **2004**, *10*, 2110.

4. Hess, H.; Clemmens, J.; Brunner, C.; Doot, R.; Luna, S.; Ernst, K. H.; Vogel, V. *Nano Lett* **2005**, *5,* 629.

5. Montemagno, C. *J Nanotechnol* **1999**, *10,* 225.

6. Liu, H.; Schmidt, J. J.; Bachand, G. D. et al. *Nat Mater* **2002**, *1*, 173.

7. Xi, J.; Schmidt, J. J.; Montemagno, C. D. *Nat Mater* **2005**, *4*, 180.

8. Antonii, F. *Panacea Aurea–Auro Potabile*, Bibliopolio Frobeniano, Hamburg **1618**.

9. Kunckels, J. *Nuetliche Observationes oder Anmerkungen von Auro und Argento Potabili*, Schutzens, Hamburg **1676**.

10. Helcher, H. H. *Aurum Potabile oder Gold Tinstur*, J. Herbord Klossen, Breslau and Leipzig **1718**.

11. Ostwald, W. *Kolloid Z.* **1909**, *4*, 5.

12. Savage, G. *Glass and Glassware*, Octopus Book, London **1975**.

13. Wagner, F. E. *et al.*, *Nature* **2000**, *407*, 691.

14. Turkevich, J. *Gold Bull.* **1985**, *18*, 86.

15. Smalley, R. *Congressional Hearings*, **Summer 1999**.

16. Roucoux, A.; Schulz, J.; Patin, H. *Chem. Rev.* **2002**, *102*, 3757.

17. Lewis, L. N. *Chem. Rev.* **1993**, 93, 2693.

18. Niemeyer, C. M. *Angew. Chem. Int. Ed.* **2001**, *40*, 4128.

19. Niemeyer, C. M. *Angew. Chem. Int. Ed.* **2003**, *42*, 5974.

20. Parak, W. J. *et al.*, *Nanotechnology* **2003**, *14*, R15.

21. Caski, A.; Maubach, G.; Born, D.; Reichert, J.; Fritzsche, W. *Single Mol.* **2002**, *3*, 275.

22. Rosi, N. L.; Mirkin, C. A. *Chem. Rev.* **2005**, *105*, 1547.

23. Parak, W. J.; Pellegrino, T.; Plank, C. *Nanotechnology* **2005**, *16*, R9.

24. Bruchez, M.; Moronne, Jr. M.; Gin, P.; Weiss, S.; Alivisatos, A. P. *Science*

1998, *281*, 2013.

25. Chan, W. C. W.; Nie, S. M. *Science* **1998**, *281*, 2016.

26. Hagfeldt, A.; Graetzel, M. *Acc. Chem. Res.* **2000**, *33*, 269.

27. Bueno, J. T.; Shchukina, N.; Ramos, A. A. *Nature* **2004**, *430*, 326.

28. Fichtner, M. *Adv. Eng. Mater.* **2005**, *7*, 443.

29. Moran, C. E.; Steele, J. M.; Halas, N. J. *Nano Lett*. **2004**, *4*, 1497.

30. Simon, U. *Nanoparticles: From Theory to Application*, Schmid, G. (ed.) Wiley-VCH, Weinheim, Germany **2004**.

31. Edelstein, A. S.; Cammarata, R. C. (eds.) *Nanomaterials: Synthesis, Properties, and Applications*, Institute of Physics Publishing, Bristol, U.K. **1996**.

32. Maier, S. A.; Brongersma, M. L.; Kik, P. G.; Atwater, H. A. *Phys. Rev. B* **2002**, *65*, 193408.

33. Wang, Y. *Acc. Chem. Res.* **1991**, *24*, 133.

34. Yoffe, A. D. *Adv. Phys.* **1993**, *42*, 173.

35. Matejivic, E. *Annu. Rev. Mater. Sci*. **1985**, *15*, 483.

36. Shull, R. D.; McMichael, R. D.; Swartzendruber, L. J.; Benett, L. H. *Studies of Magnetic Properties of Fine Particles and Their Relevance to Materials Science*, Pormann, J. J.; Fiorani, D. (eds.) Elsevier Publishers, Amsterdam **1992**, p. 161.

37. Heath, J. R.; Kuekes, P. J.; Snider, G. S.; Williams, R. S. *Science* **1998**, *280*, 1716.

38. Andres, R. P. *et al.*, *J. Mater. Res.* **1989**, *4*, 704.

39. Li, X. *et al.*, *Langmuir* **2004**, *20*, 1298.

40. Roco, M. C.; Williams, R. S.; Alivisatos, P. (eds.) *Interagenecy Working Group in Nanoscience Engineering and Technology (IWGN) Workshop Report: Nanotechnology Research Directions; Vision for Nanotechnology R and D in the Next Decade*, Int. Tech. Research Institutes, WTEC Division, Loyola College **1999**.

41. Kiwi, J.; Gratzel, M. *Angew. Chemie. Int. Ed.* **1979**, *18*, 624.

42. Riegel, G.; Bolton, R. J. *J. Phys. Chem.* **1995**, *280*, 1716.

43. Boronina, T.; Klabunde, K. J.; Sergeev, G. B. *Environ. Sci.Technol.* **1995**, *29*, 1511.

44. Li, Y. X.; Klabunde, K. J. *Langmuir* **1991**, *7*, 1388.

45. Lucas, E.; Klabunde, K. J. *Nanostruct. Mater.* **1999**, *12*, 179.

46. Khaleel, A.; Kapoor, P.; Klabunde, K. J. *Nanostruct. Mater.* **1999**, *11*, 459.

47. Koper, O.; Lagadic, I.; Volodin, A.; Klabunde, K. J. *Chem. Mater.* **1997**, *9*, 2468.

48. Koper, O. B.; Lucas, E.; Klabunde, K. J. *J. Appl. Toxicol.* **1999**, *19*, 559.

49. Wagner, G. W.; Koper, O. B.; Lucas, E.; Decker, S.; Klabunde, K. J. *J. Phys. Chem. B* **2000**, *104*, 5118.

50. Rouvray, D. *Chem. Br.* **2000**, *36*, 46.

51. Lawton, G. *Chem. Ind. (London)* **2001**, 174.

52. Havancsak, K. *Mater. Sci. Forum* **2003**, *414*, 85.

53. Mazzola, L. *Nature Biotech.* **2003**, *21*, 1137.

54. Hayat, M. A. (ed.) *Colloidal Gold :Principles, Methods and Application*, Academic Press, San Diego **1989**, *Vol. 1*.

55. Alivisatos, P. *Nature Biotechnol.* **2004**, *22*, 47.

56. Buffat, P.; Borel, J. P. *Phys. Rev. A* **1976**, *13*, 2287.

57. Brust, M.; Kiely, C. J. *Colloids Surf. A: Physicochem. Eng. Asp.* **2002**, *202*, 175.

58. Link, S.; El-Sayed, M. A. *J. Phys. Chem. B* **1999**, *103*, 4212.

59. Dick, K.; Dhanasekaran, T.; Zhang, Z.; Meisel, D. *J. Am. Chem. Soc.*, **2002**, *124*, 2312.

60. Glinka, Y. D.; Lin, S. H.; Hwang, L. P.; Chen, Y. T.; Tolk, N. H. *Phys. Rev. B*, **2001**, *64*, 085421.

61. McHale, J. M.; Auroux, A.; Perotta, A. J.; Navrotsky, A. *Science* **1997**, *277*, 788.

62. El-Sayed, M. A. *Acc. Chem. Res.* **2001**, *34*, 257.

63. Link, S.; El-Sayed, M. A. *J. Phys. Chem. B* **1999**, *103*, 8410.

64. Burda, C.; Chen, X.; Narayanan, R.; El-Sayed, M. A. *Chem. Rev.* **2005**, *105*, 1025.

65. Chen, S. *et al.*, *Science* **1998**, *280*, 2098.

66. Chen, S.; Pei, R. *J. Am. Chem. Soc.* **2001**, *123*, 10607.

67. Zhang, P.; Sham, T. K. *Appl. Phys. Lett.* **2002**, *81*, 736.

68. Quinn, B. M.; Liljeroth, P.; Ruiz, V.; Laaksonen, T.; Kontturi, K. *J. Am. Chem. Soc.* **2003**, *125*, 6644.

69. Link, S.; Mohamed, M. B.; El-Sayed, M. A. *J. Phys. Chem. B* **1999**, *103*, 3073.

70. Templeton, A. C.; Pietron, J. J.; Murray, R. W.; Mulvaney, P. *J. Phys. Chem. B* **2000**, *104*, 564.

71. Itoh, T.; Asahi, T.; Masuhara, H. *Appl. Phys. Lett.* **2001**, *79*, 1667.

72. Yan, B.; Yang, Y.; Wang, Y. *J. Phys. Chem. B* **2003**, *107*, 9159.

73. Al-Rawashdeh, N.; Foss, C. A., Jr. *Nanostruct. Mater*. **1997**, *9*, 383.

74. Xu, H.; Bjerneld, E. J.; Kall, M.; Borjesson, L. *Phys. Rev. Lett.* **1999**, *83*, 4357.

75. Su, K. H. *et al.*, *Nano Lett.* **2003**, *3*, 1087.

76. Kelly, K. L.; Coronado, E.; Zhao, L. L.; Schatz, G. C. *J. Phys. Chem. B* **2003**, *107*, 668.

77. Schmid, G.; Simon, U. *Chem. Commun.* **2005**, *6*, 697.

78. Zhang, J. H. *Acc. Chem. Res.* **1997,** *30*, 423.

79. Raimondi, F.; Scherer, G. G.; Kotz, R.; Wokaun, A. *Angew. Chem. Int. Ed.* **2005**, *44*, 2190.

80. Kreibieg, U.; Vollmer, M. *Optical properties of metal clusters*, Springer, Berlin and New York **1995**.

81. Khallel, A.; Richards, R. M. *Nanoscale Materials in Chemistry* Klabunde, K. J. (ed.) John Wiley & Sons, New York **2001**, pp. 85–120.

82. El-Shall, M. S.; Slack, W.; Vann, W.; Kane, D.; Hanley, D. *J. Phys. Chem.* **1994**, *98*, 3067.

83. Edelstein, A. S.; Hadjipanayis, G. C.; Siegel, R. W. (eds.) *Nanophase Materials*, Kluwer Academic Publishers, Dordrecht **1994**, pp. 73–80.

84. Edelstein, A. S.; Hadjipanayis, G. C.; Siegel, R. W. (eds.) *Nanophase Materials*, Kluwer Academic Publishers, Dordrecht **1994**, pp. 85–88.

85. Tan, S.; Leo, N. T. *Trans. Nanostruct. Met. Soc. China* **1995**, *2*, 58.

86. Baraton, M. I.; El-Shall, M. S. *Nanostruct. Mater.* **1995**, *6*, 301.

87. Cow, G. M.; Gonsalves, K. E. (eds.) *Nanotechnology, Molecularly Designed Materials*, American Chemical Society, Washington, D.C. **1996**, pp. 79–99.

88. Siegel, R. W. *et al.*, *J. Mater. Res.* **1998**, *3*, 1367.

89. Huh, M. Y.; Kim, S. H.; Ahn, J. P.; Park, J. K.; Kim, B. K. *Nanostruct. Mater.* **1999**, *11*, 211.

90. Messing, G. L.; Gardner, T. *J. Am. Ceram. Soc. Bull.* **1984**, *64*, 1498.

91. Kodas, T. T. *Adv. Mater.* **1989**, *6*, 180.

92. Jayanthi, V.; Zhang, S. C.; Messing, G. L. *J. Aerosol Sci. Technol.* **1993**, *19*, 478.

93. Messing, G. L.; Zhang, S. C.; Jayanthi, V. *J. Am. Ceram. Soc.* **1993**, *76*, 2707.

94. Edelstein, A. S.; Hadjipanayis, G. C.; Siegel, R. W. (eds.) *Nanophase Materials*, Kluwer Academic Publishers, Dordrecht **1994**, pp. 109–116.

95. Janackovic, D.; Jokanovic, V.; Gvozdenovic, L. K.; Uskokovic, D. *Nanostruct. Mater.* **1998**, *10*, 341.

96. Ulrich, G. D.; Riehl, J. W. *J. Colloid Interface Sci. Technol.* **1982**, *87*, 257.

97. Cow, G. M.; Gonsalves, K. E. (eds.) *Nanotechnology, Molecularly Designed Materials*, American Chemical Society, Washington, D.C. **1996**, pp. 64–78.

98. Lindackers, D.; Janzen, C.; Rellinghaus, B.; Wassermann, E. F.; Roth, P. *Nanostruct. Mater.* **1998**, *10*, 1247.

99. Palkar, V. R. *Nanostruct. Mater.* **1999**, *11*, 369.

100. Barringer, E. A.; Bowen, H. K. *J. Am. Ceram. Soc.* **1982**, *65*, C199.

101. Segal, D. *Chemical Synthesis of Advanced Ceramic Materials*, Cambridge University Press, Cambridge **1989**.

102. Gesser, H. D.; Gosswami, P. C. *Chem. Rev.* **1989**, *89*, 765.

103. West, J. K. *Chem. Rev.* **1990**, *90*, 33.

104. Brinker, C. J.; Scherer, G. W. *Sol–Gel Science: The Physics and Chemistry of Sol–Gel Processing*, Academic Press, Boston **1990**.

105. Chandler, C. D.; Roger, C.; Smith, M. J. H. *Chem. Rev.* **1993**, *93*, 1205.

106. Klein, L. (ed.) *Sol–Gel Optics: Processing and Applications*, Kluwer, Boston **1993**.

107. Hench, L. L.; Avnir, D. *Acc. Chem. Res.* **1995**, *28*, 328.

108. Narula, C. K. *Ceramic Precursor Technology and Its Applications*, Marcel Decker, New York **1995**.

109. Interrante, L. V.; Smith, M. J. H. (eds.) *Chemistry of Advanced Materials: An Overview*, Wiley–VCH, New York **1998**.

110. Toshima, N.; Harada, M.; Yonezawa, T.; Kushihashi, K.; Asakura, K. *J. Phys. Chem.* **1991**, *95*, 7448.

111. Chaudret, B.; Bradley, J. S.; Mazel, R.; Roucau, C. *J. Am. Chem. Soc.* **1993**, *115*, 11638.

112. Toshima, N.; Wang, Y. *Adv. Mater.* **1994**, *6*, 245.

113. Naka, K.; Yaguchi, M.; Chujo, Y. *Chem. Mater.* **1999**, *11*, 849.

114. Warner, M. G.; Reed, S. M.; Hutchison, J. E. *Chem. Mater.* **2000**, *12*, 3316.

115. Tan, Y.; Dai, X.; Li, Y.; Zhu, D. *J. Mater. Chem.* **2003**, *13*, 1069.

116. Trivino, G. C.; Klabunde, K. J.; Dale, E. B. *Langmuir* **1987**, *3*, 986.

117. Brust, M.; Fink, J.; Bethell, D.; Schiffrin, D. J.; Kiely, C. J. *Chem. Commun.* **1995**, 1655.

118. Kim, K. S.; Demberelnyamba, D.; Lee, H. Langmuir **2004**, *20*, 556.

119. Ohde, H.; Hunt, F.; Wai, C. M. *Chem. Mater.* **2001**, *13*, 4130.

120. Viswanathan, R.; Lilly, G. D.; Gale, W. F.; Gupta, R. B. *Ind. Eng. Chem. Res.* **2003**, *42*, 5535.

121. Meyer, M.; Wallberg, C.; Kurihara, K.; Fendler, J. H. *Chem. Commun.* **1984**, 90.

123. Petit, C.; Jain, T. K.; Billoudet, F.; Pileni, M. P. *Langmuir* **1994**, *10*, 4446.

124. Forster, S.; Antonietti, M. *Adv. Mater.* **1998**, *10*, 195.

125. Minko, S.; Kiriy, A.; Gorodyska, G.; Stamm, M. *J. Am. Chem. Soc.* **2002**, *124*, 10192.

126. Zhang, M.; Drechsler, M.; Muller, A. H. E. *Chem. Mater.* **2004**, *16*, 537.

127. Braun, E.; Eichen, Y.; Sivan, U.; Yoseph, G. B. *Nature* **1998**, *391*, 775.

128. Richter, J. *et al.*, *Adv. Mater.* **2000**, *12*, 507.

129. Shenton, W.; Douglas, T.; Young, M.; Stubbs, G.; Mann, S. *Adv. Mater.* **1999**, *11*, 253.

130. Fowler, C. E.; Shenton, W.; Stubbs, G.; Mann, S. *Adv. Mater.* **2001**, *13*, 126.

131. Dujardin, E.; Peet, C.; Stubbs, G.; Culver, J. N.; Mann, S. *Nano Lett.* **2003**, *3*, 413.

132. Wiesner, J.; Wokaun, A. *Chem. Phys. Lett.* **1989**, *57*, 569.

133. Mann, S.; Angew. Chem., Int. Ed., **2000**, *39*, 3392–3406.

134. Dujardin, E. and Mann, S. Adv. Mater., **2002**, *14*, 775–788.

135. Lowenstam, H. A.; Weiner, S. *On Biomineralization*; Oxford University Press: New York, **1989**.

136. Baeuerlein, E. *Biomineralization, Progress in Biology, Molecular Biology, and Application*; Wiley-VCH Verlag GmbH & Co. KGaA: Weinheim, Germany, **2004**.

137. Baeuerlein, E. *Handbook of Biomineralization, Biological Aspects and Structure Formation*; Wiley-VCH Verlag GmbH & Co. KGaA: Weinheim, Germany, **2007**.

138. Mann, S. *Biomineralization*; Oxford University Press: Oxford, U.K., **2002**.

139. Bazylinski, D. A.; Frankel, R. B. *Nat. Rev. Microbiol.* **2004**, *2*, 217.

140. Komeili, A. *Annu. Rev. Biochem.* **2007**, *76*, 351.

141. Sollner, C.; Burghammer, M.; Busch-Nentwich, E.; Berger, J.; Schwarz, H.; Riekel, C.; Nicolson, T. *Science* **2003**, *302*, 282.

142. Addadi, L.; Joester, D.; Nudelman, F.; Weiner, S. *Chem.sEur. J.* **2006**, *12*, 981.

143. Addadi, L.; Raz, S.; Weiner, S. *Adv. Mater.* **2003**, *15*, 959.

144. Aizenberg, J.; Sundar, V. C.; Yablon, A. D.; Weaver, J. C.; Chen, G. *Proc. Natl. Acad. Sci. U.S.A.* **2004**, *101*, 3358.

145. Sundar, V. C.; Yablon, A. D.; Grazul, J. L.; Ilan, M.; Aizenberg, J. *Nature* **2003**, *424*, 899.

146. Muller, W. E. G.; Eckert, C.; Kropf, K.; Wang, X. H.; Schlomacher, U.; Seckert, C.; Wolf, S. E.; Tremel, W.; Schroder, H. C. *Cell Tissue Res.* **2007**, *329*, 363.

147. Muller, W. E. G.; Wendt, K.; Geppert, C.; Wiens, M.; Reiber, A.; Schroder, H. C. *Biosens. Bioelectron.* **2006**, *21*, 1149.

148. Cattaneo-Vietti, R.; Bavestrello, G.; Cerrano, C.; Sara, M.; Benatti, U.; Giovine, M.; Gaino, E. *Nature* **1996**, *383*, 397.

149. Round, F. E.; Crawford, R. M.; Mann, D. G. *The Diatoms: Biology and Morphology of the Genera*; Cambridge University Press: New York, 1990.

150. Addadi, L.; Weiner, S. *Angew. Chem. Int. Ed.* **1992**, *31*, 153.

151. Weiner, S.; Traub, W.; Lowenstam, H. A. *Biomineralization and Biological Metal Accumulation*, Westbroek, P.; Jong, E. W.; Dordrecht, R. (eds.) **1983**, p. 205.

152. Gower, L. A. *Variety of Biomineral Types and Biological Systems*, http://www.gower.mse.ufl.edu/research.html.

153. Mann, S. *Inorganic Materials*, 2nd edition, Bruce, D. W.; O'Hare, D. (eds.) John Wiley & Sons **1996**.

154. Cheavin, W. H. S. *Microscope* **1938**, *2*, 155.

155. Monje, P.V.; Baran, E. J. *J. Plant Physiol.* **2004**, *161*, 121.

156. Arnott, H.J. *Biological Mineralization and Demineralization,* Nancollas, G. H. (ed.) Springer Verlag, Berlin **1982**, pp. 199–218.

157. Monje, P. V.; Baran, E. J. *Advances in Plant Physiology*, Vol. 7, Hemantaranjan, H. (ed.) Scientific Publishers, Jodhpur **2004** pp. 403–419.

158. Wal, P. V. D.; Jong, E. W. D.; Westbrock, P.; Bruijn, W. C. D.; Stapel A. A. H. *J. Ultrastructure. Res.* **1983**, *85*, 139.

159. Marsh, M. E. *Biomineralization*, Baeuerlein, E. (ed.) Wiley–VCH, Weinheim, Germany **2000**, p. 251–268.

160. Frankel, R. B.; Bicudo, C. E. M. *Biophys. J.* **1986**, *50*, 375.

161. Mann, S.; Sparks, N. H.; Walker, M. M.; Kirschvink, J. L. *J. Exp. Biol.* **1988**, *140*, 35.

162. Kirschvink, A. K.; Woodford, B. J. *Proc. Natl. Acad. Sci. USA* **1992**, *89*, 7683.

163. Kirschvink, J. L.; Dobson, J.; Grassi, P. P. *Brain Res. Bull.* **1996**, *39*, 255.

164. Walker, M. M. *et al.*, *Nature* **1997**, *390*, 371.

165. Devouard, B. *et al.*, Am. *Mineral.* **1998**, *83*, 1387.

166. Grassi, P. P. S.; Wessiken, R.; Dobson, J. *Biochem. Biophys. Acta* **1999**, *1426*, 212.

167. Grassi, P. P. S.; Dobson, J. *BioMetals* **1999**, *12*, 67.

168. Araujo, F. F. T. D.; Pires, M. A.; Bazylinski, D. A.; Frankel, R. B. *Biomineralization*, Baeuerlein , E. (ed.) Wiley–VCH, Weinheim, Germany **2000**, p. 41–43.

169. Diebel, C. E.; Proksch, R.; Green, C. R.; Neilson, P.; Walker, M. M. *Nature* **2000**, *406*, 299.

170. Posfai M. *et al.*, *Eur. J. Mineral.* **2001**, *13*, 691.

171. Josifovska M. G.; McClean R. G.; Schofield M. A.; Sommer C. V.; Kean W. F. *Eur. J. Mineral.* **2001**, *13*, 863.

172. Baurerlein, E. *Angew. Chem. Int. Ed.* **2003**, *42*, 614.

173. Monje, P. V.; Baran, E. J.; *J. Plant Physiol.* **2000**, *157*, 457.

174. Mann S (1992) Nature 357:358

175. Slocik JM, Knecht MR, Wright DW In: Nalwa HS (ed) Encyclopedia of nanoscience and nanotechnology, **2004,** vol 1. American Scientific, p 293

176. Li X-Z, Nikaido H, Williams KE *J Bacteriol* **1997**, *179*, 6127.

177. Rorrer, G. L.; Chang, C. H.; Liu, S. H.; Jeffryes, C.; Jiao, J.; Hedberg, J. A. *J. Nanosci. Nanotechnol.* **2005**, *5*, 41.

178. Curnow, P.; Bessette, P. H.; Kisailus, D.; Murr, M. M.; Daugherty, P. S.; Morse, D. E. *J. Am. Chem. Soc.* **2005**, *127*, 15749.

179. Smith, B. L.; Paloczi, G. T.; Hansma, P. K.; Levine, R. P. *J. Cryst. Growth* **2000**, *211*, 116.

180. Walters, D. A.; Smith, B. L.; Belcher, A. M.; Paloczi, G. T.; Stucky, G. D.; Morse, D. E.; Hansma, P. K. *Biophys. J.* **1997**, *72*, 1425.

181. Kroger, N.; Lehmann, G.; Rachel, R.; Sumper, M. *Eur. J. Biochem.* **1997**, *250*, 99.

182. Shimizu, K.; Cha, J.; Stucky, G. D.; Morse, D. E. *Proc. Natl. Acad. Sci. U.S.A.* **1998**, *95*, 6234.

183. Xu, Z.P.; Zeng, Q.H.; Lu, G.Q. & Yu, A.B. *Chem. Engineering Sc* **2006,** *61*, 1027.

184. Cheon, J. & Horace, G. *J. Mater. Chem.* **2009,** *19,* 6249.

185. Caseri, W. *Chem. Engineering Commun.* **2009,** 196 *(5)*, 549.

186. Mohanpuria, P.; Rana, K.N. & Yadav, S.K *J. Nano. Res.* **2008**, *10*, 507.

187. Raveendran, P.; Fu, J. & Wallen., S.L. *J. Am. Chem. Soc.* **2003,** 125 *(46)*, 13940.

188. Li, S.; Shen, Y.; Xie,A.; Yu, X.; Qui, L.; Zhang, L. & Zhang, Q. Green Chemistry **2007,** *9*, 852.

189. Parashar, U.K.; Saxena, S.P. & Srivastava, A. *Digest journal of nanomaterials and biostructures* **2009,** 4 *(1)*, 159.

190. Parashar, V.; Prashar, R.; Sharma, B. & Pandey, A.C. *Digest journal of nanomaterials and biostructures* **2009**, 4 *(1),* 45.
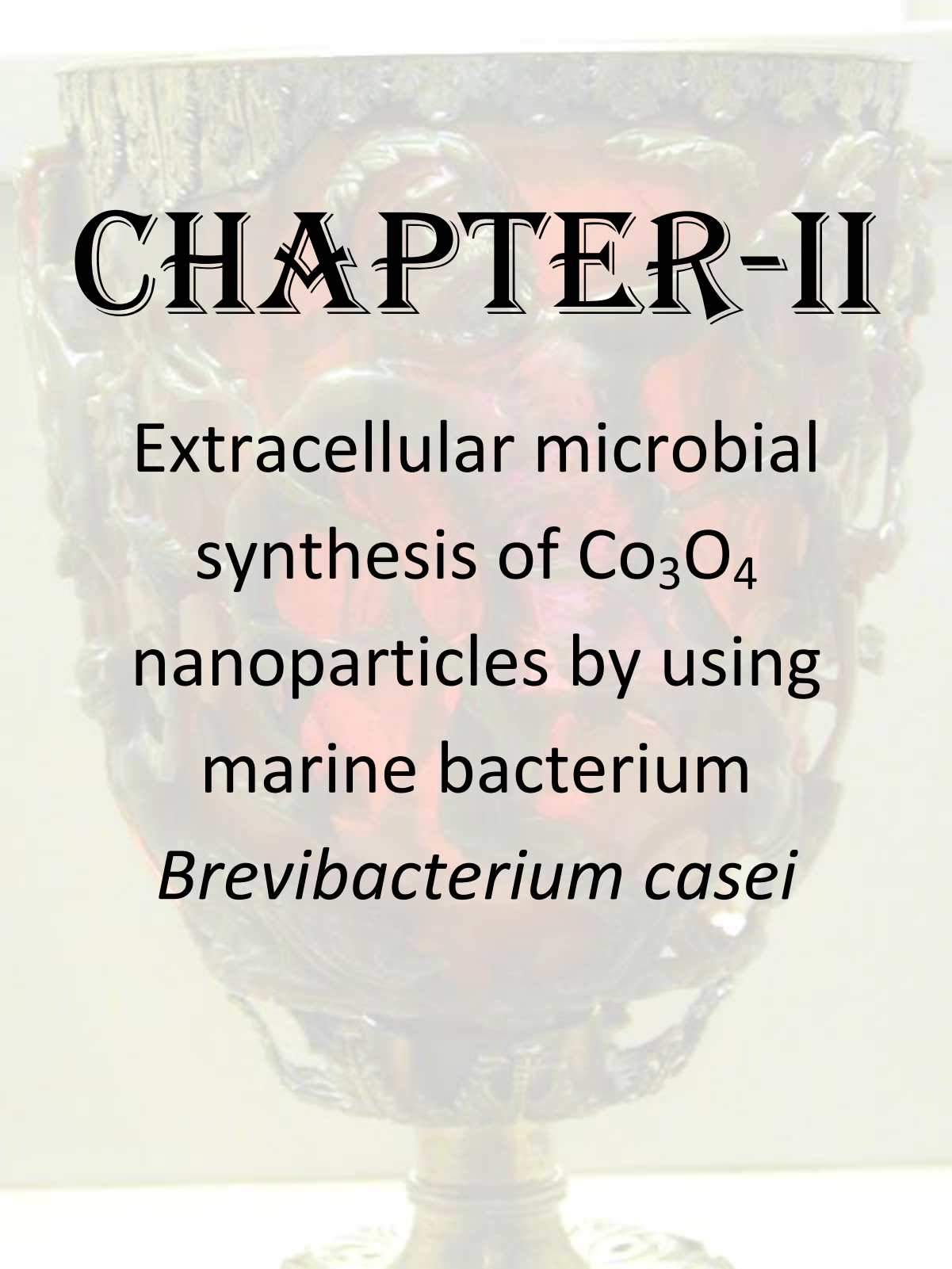
CHAPTER-II

Extracellular microbial synthesis of Co$_3$O$_4$ nanoparticles by using marine bacterium *Brevibacterium casei*

Extracellular microbial synthesis of Co_3O_4 nanoparticles using marine bacterium *Brevibacterium casei*
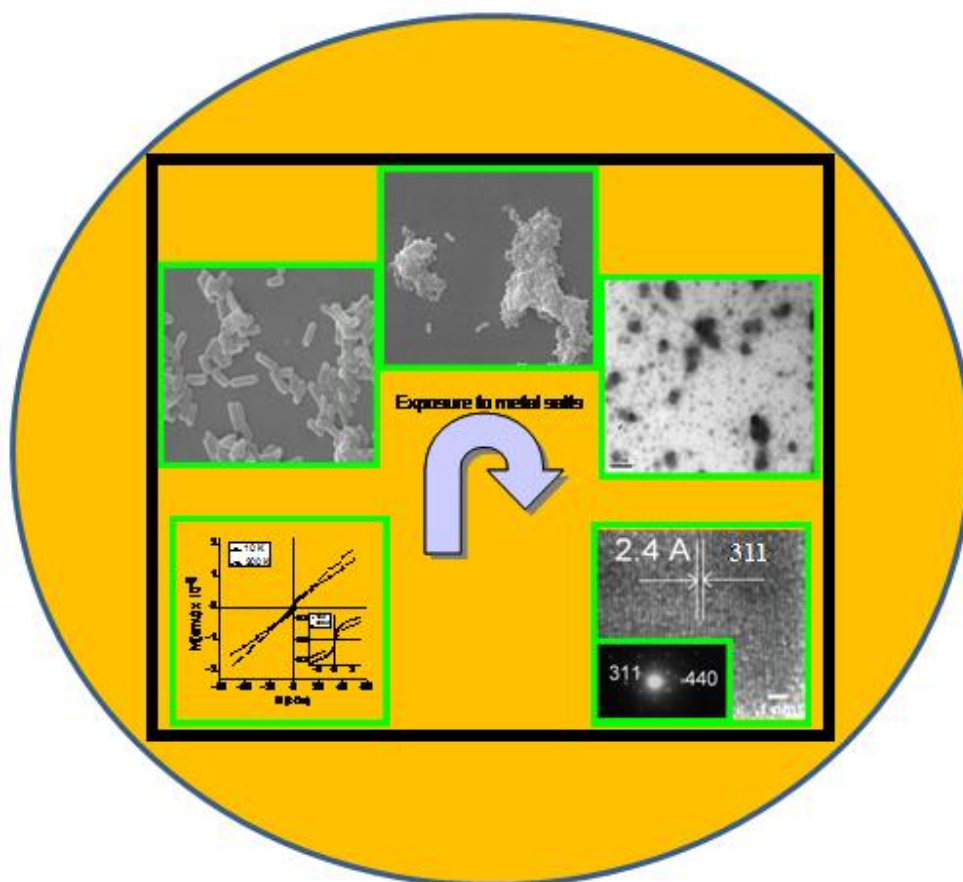
Co_3O_4, which crystallizes in spinel phase at temperatures much higher than ambient temperatures, orders antiferromagnetically below its Neel temperature (~40K), However, in nano size, it shows ferromagnetic ordering due to surface canting, disorder, imperfect oxygen atom coordination etc. Here, for the first time, we report the synthesis of single-crystalline, ferromagnetic Co_3O_4 nanoparticles functionalized with proteins (size 5-7 nm) using cobalt acetate as precursor at room temperature in aqueous medium by a metal-tolerant marine bacterium isolated from the coast of the Arabian Sea. Energetically unfavourable change in the oxidation state of cobalt atoms from (+2 to +3) during synthesis by the bacterial strain was evidenced by X-ray photoelectron spectroscopy. The effect on the morphology of bacterial cells after exposure to the cobalt acetate was imaged by scanning electron microscopy showing cooperative, self-organized, structured aggregate formation, possibly due to the inter-

bacterial communication under external stress. This chapter describes a new method for the synthesis of Co_3O_4 nanopoarticles under ambient conditions with the using bacteria; *Brevibacterium casei*. The oxidation of the precursor, which results in Co_3O_4 nanocrystals formation, passivated by protein; is hypothesized to be mediated by the oxido-reductase and hydrolases class of enzymes. Different experimental techniques have been used to thoroughly characterize this material and their details are discussed in this chapter.

2.1 Introduction

It is well known that biological systems can synthesize number of metal or metal-containing particles in the nanometer size range[1]. For example, many multicellular organisms use inorganic materials (such as calcium carbonate or silica) in combination with an organic matrix (proteins, lipids or polysaccharides) to produce hard materials, such as skeletal units, teeth and bones. Single-celled organisms can also produce mineral structures that form inorganic materials either intracellularly or extracellularly; examples include magnetotactic bacteria, which produce magnetite (Fe_3O_4) or greigite (Fe_3S_4) and diatoms, which produce siliceous materials. These particulate systems can be used as precursors for the manufacturing the functional materials[2]. Furthermore, microbial activity is known to be responsible for the transformation of at least one third of the elements in the periodic table[3]. These transformations are the results of assimilatory, dissimilatory, or detoxification processes and form the cornerstones of many biogeochemical cycles involving change in the valence states (i.e. oxidation/reduction) or chemical form (i.e. solid, liquid, gas) of elements[3]. Metals play an integral role in the life- processes of microorganisms. Some metals, such as calcium, cobalt, iron, potassium, sodium etc. are as essential as nutrients and are required since they function as the catalysts for biochemical reactions, stabilizer of protein structures and bacterial cell walls, serve in maintaining osmotic balance, involve in redox processes or stabilize various enzymes and DNA through electrostatic forces[4]. Marine water and sediments contain lot of metal salts which are naturally present or they enter into the marine environment as contaminants through dumping of huge amount of industrial and domestic wastes containing salts of lead, arsenic, cadmium, nickel, cobalt, mercury, silver etc[5]. Therefore, high metal tolerance, among marine bacteria, is a common

phenomenon which makes them ideal candidates for exploring metal/metal-oxide nanoparticle synthesis in the laboratory environment[6].

Very recently, the microbial syntheses of inorganic materials including noble metals, alloys, binary oxides as well as ternary oxides using fungi, yeast, bacteria and variety of other microorganisms has gained popularity[7-9]. The reason being, their obvious advantages over the traditional wet-chemical methods, wherein, the synthesis methodology often requires expensive organometallic precursors, high temperature, pressure and hazardous chemicals and solvents. On the other hand, the reduction of metal ions by microbes in nature occurs under ambient conditions. In this "green synthesis route", as-synthesized particle surface is inherently functionalized by the proteins which give them specific advantages. Due to this inherent and robust bio-fuctionalization, the as-synthesized particles form stable suspension in the aqueous medium and further coating of bio-molecules becomes easier. The protein layer also prevents particles surfaces from fusing together directly, although, the particles tend to agglomerate due to the protein-protein interactions. In contrast to the surfactant passivated magnetic nanoparticles synthesized by traditional methods, the protein functionalized particles are more likely to behave as isolated particles due to relatively thicker coating of proteins preventing interparticle interactions. These particles can be easily dried out of aqueous medium to form powder and can be resuspended without agglomeration.

Similar to any other synthesis route, the microbial synthesis comes with several challenges such as- better control over size and shape, scaling-up of the synthesis of nanomaterials as well as synthesis of complex oxide materials with desired phases which need to be addressed and solved. Chemical synthesis of nanomaterials, on the other hand, has already advanced to provide excellent control over size and shape. Another challenge, in case of microbial technique, is to fully understand the synthesis mechanism at the molecular level, which eventually may help in providing better control over size and shapes as well as crystallinity in future.

In this chapter, learning from nature's own sustainable way of remediation of the metal ions, we have shown the utilization of ability of a marine bacterial culture in the laboratory environment to synthesize spinel structured, crystalline Co_3O_4 nanoparticles. This sample of marine water was obtained from the Arabian sea-coast. Out of 15 bacterial strains isolated from the marine-water and sediment sample, only three bacterial strains showed resistance to cobalt after exposing them to cobalt-

acetate which is used as a precursor in this study for the synthesis of Co_3O_4 nanoparticles. Further, only one strain gave us the visible indication of formation of nanoparticles i.e appearance of turbidity and other two did not give any positive indication. The Co_3O_4 particles formed by this method are inherently passivated by the bacterial proteins. Co_3O_4 is known to have a normal cubic spinel structure and is antiferromagnetic in the bulk form with the Neel temperature T_N between 30-40 K[10]. However, in the nano-regime, uncompensated spins at the particle surfaces can become a large fraction of the total number of spins thereby giving overall ferromagnetic-type behaviour. Magnetic nanoparticles have aroused enormous interest owing to their unique size and shape dependent properties and potential applications e.g., magnetocaloric refrigeration, read-head sensors, magnetic storage media, as filler materials in polymers in electromagnetic shielding applications, magnetorheological devices etc[11-15]. There are various wet-chemical methods reported to synthesize the Co_3O_4 nanoparticles, however, to the best of our knowledge, there is no report on the microbial synthesis of Co_3O_4. We believe that any previous attempts for the microbial synthesis of this material (or even cobalt-nanoparticles) could have failed due to the toxicity of the cobalt ions towards previously used bacterial, fungi cultures. Moreover, it should be noted that when it comes to the microbial synthesis of the magnetic nanoparticles, γ-Fe_2O_3 and Fe_3O_4 are the only materials which are previously reported in the literature[7]. According to the current understanding, in most of these biosynthesis processes, precursor salts are either hydrolyzed or reduced, and the proteins responsible for these processes are generally cationic in nature.[16] Heavy metals are disseminated through the environment as part of a natural planetary biogeochemical activity and have been adopted by the biological systems because of their catalytic versatility but their reactivity turns them toxic even at very low concentrations. Their toxicity in connection with their nonspecific intake by different channels and transporters has forced the organisms living in contact with these metals to develop systems to tightly control metal-ion homeostasis and resistance[17]. Heavy metal resistance in bacteria is the result of multiple resistance systems; different mechanisms displayed by different organisms, probably depend on the niche from which the organism has been isolated. Different mechanisms are responsible for conferring cobalt resistance. The first mechanism includes the members of the resistance-nodulation cell division (RND) protein family which helps in export of superfluous cations. This system is known as

the CzcCBA efflux system which is responsible for efflux of Co^{2+}, Zn^{2+}, Cd^{2+}, and Ni^{2+}. Similar to CzcCBA, two different homologous systems have been reported, i.e., Cnr operon and *rcnA* locus which confers resistance to cobalt and nickel[18,19] and ncc locus which confers resistance to cobalt, nickel, and cadmium[20]. The second mechanism is cation diffusion facilitator (CDF family) which serves as secondary cation filters in bacteria. Primary substrates of CDF proteins are Zn^{2+}, Co^{2+}, Ni^{2+}, Cd^{2+}, and Fe^{2+}.[21] In all these mechanisms, it has been proposed that Co^{2+} is the ion moiety which goes inside the cell and comes out through efflux pump.

The possible proteins/enzymes involved in the process of Co_3O_4 nanoparticles synthesis have been analyzed by SDS-PAGE and the over expression of few new proteins was observed. The molecular weight of these proteins resembled with those of oxidases and reductases, and was in accordance with the earlier reports[16,22]. The presence of protein coating on the resultant nanoparticles has been confirmed by FTIR spectroscopy. The formation of Co_3O_4 is comprehensively and conclusively proven by XPS, XRD, TEM and HRTEM studies.

2.2 Materials and methods

2.2.1 Isolation of the bacterial strains (*Brevibacterium casei*) from the Arabian sea-coast

The marine-water and sediment samples were collected from the coastal areas of the Arabian sea near the Sindhudurg district, India. For this purpose, surface-water samples (approximately 300 ml) were collected in the sterile plastic bottles from 3-4 places of the site and sediment samples were collected on the beach from depth of 1 foot. These samples were processed in the laboratory after 10-12 hours and stored at 4 °C until further use. Various media were used for the isolation of marine strains including the "Zobell marine medium" (Annexure-1) (HiMedia Labs Pvt. Ltd, Mumbai, India) and the "Minimal medium" (MM). All the samples were pooled together and mixed thoroughly. From this pooled main sample, three subsamples were used for further processing. Individual samples were also processed in the same manner. From the undiluted and serially diluted (10^{-2}, 10^{-4}, 10^{-6}, 10^{-8}) subsamples, 100 μl aliquots was plated on each medium. All the media plates were incubated at 28 °C for seven days. The colony morphotypes on each plate were observed after

every 24 hour interval. As many as 15 bacterial strains isolated from the marine water and sediment samples were selected for further use. The growth pattern of the bacterial strains was checked on the "Zobell marine medium" containing cobalt to select the cobalt resistant bacterium for the nanoparticle synthesis. The "minimum inhibitory concentration" (MIC) of cobalt for all the bacterial strains was determined using the "double-dilution method"[23]. It was observed that three strains showed higher MIC (1024 μg/ml) and therefore selected for the synthesis of cobalt-oxide nanoparticles.

2.2.2 Biosynthesis of Co_3O_4 nanoparticles using *Brevibacterium casei*

After isolation and identification of three bacterial strains, the bacterial cells were grown in Zobell broth (100 ml) for 24 hours at room temperature. Once the bacterial-growth attains log phase, cells were harvested by centrifugation at 6000 rpm for 10 minutes and washed twice with autoclaved-water maintaining the sterile condition. After washing, the cell pellet was resuspended in 100 ml aqueous solution of 1mM cobalt acetate. The reaction-flask was kept on the shaker at room temperature for 72 hours at 200 rpm. After three days, visible indication of nanoparticles formation i.e. appearance of turbidity was noticed in case of only one strain and other two strains did not give any positive indication. The bacterial isolate (AP6) showing positive results was identified by 16S rRNA oligonucleotide cataloguing technique. Phylogenetic analysis of the 16S rRNA gene sequence of AP6 revealed an affiliation of the strain with *Brevibacterium casei* (Annexure-1). The reaction mixture was centrifuged at 6000 rpm for 10 minutes and the supernatant was used for further characterization by using different characterization techniques such as UV-vis spectrophotometer, FTIR, TEM, SEM, XRD, XPS and HRTEM. Part of the sample was also calcined at 200 °C for 2 hours to remove the excess protein. In control experiment, the harvested bacterial biomass was resuspended in autoclaved deionized water in the absence of cobalt acetate and the filtrate obtained thereafter was characterized for the presence of cobalt oxide (Co_3O_4) nanoparticles. Formation of nanoparticles was not observed in this reaction as expected. In another experiment, the oxidation of (Co^{2+}) cobalt acetate in autoclaved deionized water in

the absence of bacterial biomass was studied by TEM and FTIR. This control experiment was also negative as no nanoparticles were detected.

2.2.3 Morphological studies of *Brevibacterium casei* by SEM while interacting with precursor salt to synthesize Co_3O_4 nanoparticles

Morphological status of bacterial cells before and after exposure to cobalt acetate was examined by carrying out SEM studies. The bacterial SEM samples were prepared by removing the bacterial cells samples at regular intervals of 24 h, 48 h and 72 h from the reaction flask after exposing them to the precursor salt. Respective control samples were also prepared in the similar way but without exposing the cells to the precursor salt. In all the cases, the cells were washed twice with double distilled water by centrifuging at 6000 rpm for 10 minutes which was followed by resuspending them in water for sample preparation and dropcasting on the glass cover-slips. The cells were then treated with 2% gluteraldehyde at 4 °C for 2 hours. These cells were further treated with the "phosphate buffer saline" (PBS, pH=7.2, 0.1M) twice for 20 minutes each. These cells were then exposed to different grades of ethanol (i.e 30%. 70% and 100%) each for 20 seconds. After that the cells were finally air dried and coated with gold for SEM imaging.

2.2.4 Magnetic measurements

To check the magnetic properties of the Co_3O_4 nanoparticles magnetization vs magnetic field loop measurements for as-synthesized and calcined samples were carried out at 10 and 300 K. For these measurements, Magnetic Property Measurement System (MPMS) from Quantum Design Inc., USA equipped with SQUID magnetometer and superconducting magnet was used. For this purpose, the sample was wrapped in the Teflon tape and packed inside the gelatin capsule.

2.2.5 Protein profile studies

To identify the bacterial protein(s) responsible for oxidation of the Co^{2+} the extracellular protein profile of the bacterial culture supernatant was checked for the induction of new protein/s upon 1mM cobalt acetate exposure. Proteins formed were analyzed by running 10% SDS-PAGE (Sodium Dodecyl Sulphate Polyacrylamide

Gel Electrophoresis). The 24 h grown bacterial biomass was suspended in 100 ml of sterile distilled water containing 1 mM cobalt acetate. This cell suspension was kept at room temperature and 200 rpm for 72 h. The supernatant containing the extracellular proteins secreted by the bacteria in presence of salt precursor, cobalt acetate, were separated from the bacterial biomass by centrifugation at 6000 rpm for 10 minutes. This cell free solution or supernatant was then lyophilized and concentrated. In a separate set of experiments, all the conditions were kept same except for addition of salt precursor. The cell free supernatant obtained in this case also were concentrated as stated above. The proteins obtained this way were analyzed by 10% SDS-PAGE, at pH 8.5 and run along with the standard molecular weight markers according to the procedure published by Laemmli[24]. The polyacrylamide gels were stained using silver staining protocol to visualise the protein bands.

2.3 Material characterization

FTIR spectroscopy measurement for as prepared and calcined Co_3O_4 nanocrystalline powder was taken in KBr pellet using a Perkin–Elmer Spectrum One instrument. Spectrometer operated in the diffuse reflectance mode at a resolution of 2 cm^{-1}. SEM measurements on bacterial cells were performed on a Leica Stereoscan-440 instrument equipped with a Phoenix EDAX attachment operated at 20 kV. Samples for the Transmission Electron Microscopy (TEM) were prepared by drop coating the nanoparticles solution on carbon-coated copper grids. Selected area electron diffraction (SAED) as well as High Resolution Transmission Electron Microscopy (HRTEM) measurements were also carried out from the same TEM grid. TEM measurements were performed on a JEOL model 1200EX instrument operated at an accelerating voltage of 120 kV. HRTEM measurements were carried out on a JEOL–JEM-2010 UHR instrument operated at a lattice image resolution of 0.14 nm. X-Ray Diffraction (XRD) measurements of drop coated films of reaction products on glass substrate were carried out on a PHILIPS X'PERT PRO instrument equipped with X'celerator- a fast solid-state detector on dropcoated sample on glass substrate. The sample was scanned using X'celerator with a total number of active channels of 121. Iron-filtered Cu Kα radiation (=1.5406 Å) was used. XRD patterns were recorded in the 2θ range of 20°- 80° with a step size of 0.02° and a time of 5 seconds per step. X-

ray photoemission spectroscopy (XPS) measurements of films of the nanocoparticles casted on to Si substrates were carried out on a VG MicroTech ESCA 3000 instrument at a pressure $<1\times10^{-9}$ Torr with an overall resolution of 1 eV. The spectra was recorded with unmonochromatic Mg K alpha radiation (photon energy = 1253.6 eV) at a pass energy of 50 eV and electron take off angle (angle between electron emission direction and surface plane) of 60°. Thermogravimetric analysis for biologically synthesized Co_3O_4 nanocrystals was performed on Diamond Q5000 by Perkin-Elmer by applying scan rate 100 °C min^{-1} under the flow of nitrogen. For these measurements, samples were dried under the lamp to obtain it in powder form.

2.4 Results and Discussions

2.4.1 Transmission electron microscopic analysis

To analyze the size and shape of the particles in a broader range, TEM investigation were performed (figure 2.1) on both as-synthesized (panel A) and calcined nanoparticles (panel B). The top panel shows that the as-synthesized particles seem to agglomerate due to protein-functionalized surfaces with average size of the quasi-spherical particles around 6 nm. The robust protein coating, on one hand, helps the agglomeration due to the interprotein linkage and, on the other hand, prevents the Co_3O_4 particles surfaces to fuse together to have exchange interaction, thereby keeping their identity as an isolated intact nanoparticle. After mild calcination (200 °C for 2 h), it appears that the particles get further agglomerated, and the size of these agglomerates increases to around 50 nm as at this temperature proteins start
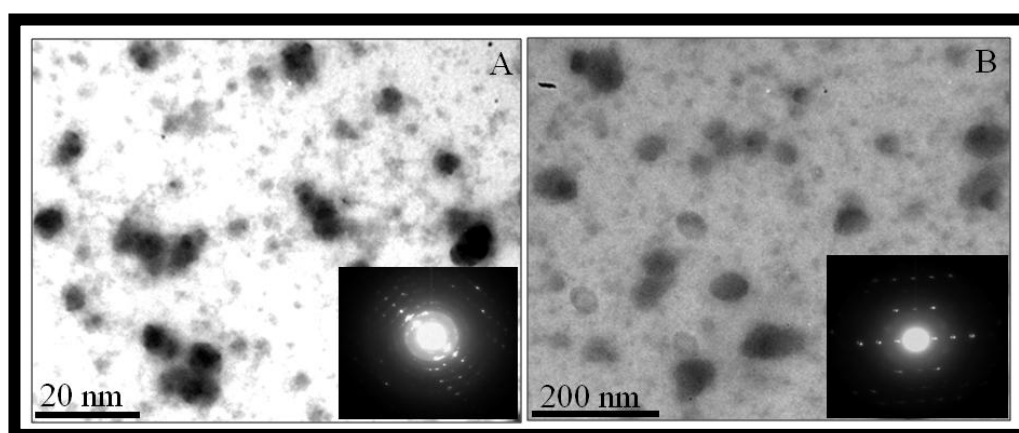
Figure 2.1: TEM micrographs of as-synthesized (panel A) and calcined (panel B) Co$_3$O$_4$ nanoparticles. Inset shows selected area diffraction (SAED) patterns

degrading and clumping together. We believe that inside the agglomerated mass the Co_3O_4 nanoparticle surfaces still remain isolated due to the coating and actual particle sizes are much smaller. The selected area electron diffraction (SAED) patterns presented in the insets of both the panels show a dot pattern indicating very good single crystallinity, consistent with the XRD patterns.

2.4.2 X-ray diffraction spectra analysis

It is interesting to note that the XRD pattern for the as-synthesized sample (curve 1) shows only two well-defined peaks corresponding to [220] and [440] planes. The peak corresponding to [220] is most intense in this case. However, for a nontextured, polycrystalline sample, the [331] peak situated at $2\theta = 36.7°$ shows the highest intensity, and the peak situated at [220] is the second highest intense peak (PCPDF# 78-1970, 43-1003). The absence of [331] as well other (relatively less intense) peaks indicates highly oriented growth of the nanocrystals toward [220] plane. After calcination (curve 2), we find that the peak at [440] becomes more pronounced, and another peak corresponding to the [400] plane emerges. The lattice constant (8.0 Å) calculated from our XRD data matches with the value reported in literature for bulk Co_3O_4[10].
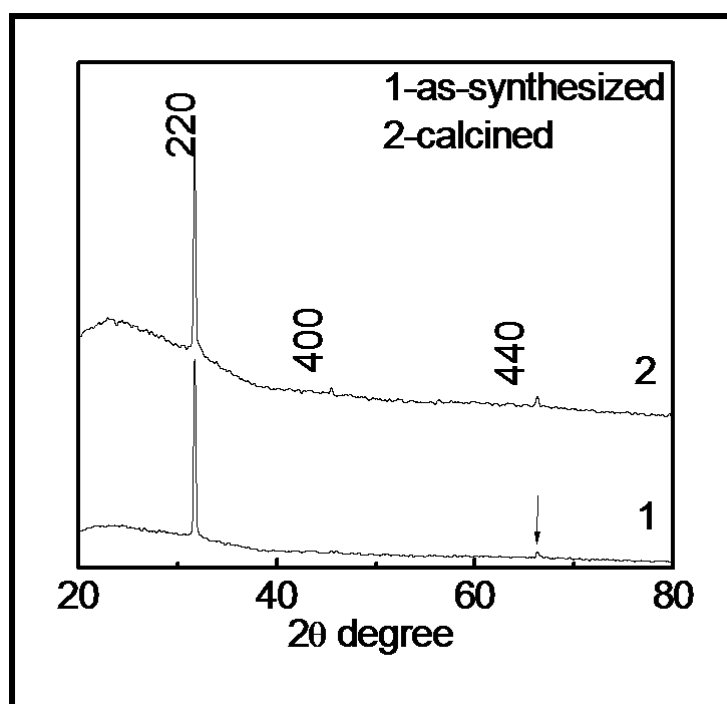
Figure 2.2: Powder XRD pattern of as-synthesized (curve 1) and calcined (curve 2) Co_3O_4 nanoparticles

2.4.3 HRTEM analysis

To confirm the crystallinity and shape of the particles, high-resolution transmission electron microscopy (HR-TEM) investigation were performed on as-synthesized particle (figure 2.3), where HR image (A) and SAED pattern (B) could be seen. In figure A, highly crystalline lattice was seen clearly even for as-synthesized particles with lattice-plane corresponding to [311] with *d* value of 2.4 Å (highest intense) which was not seen in the XRD pattern (Figure 2.2). The SAED image (B) shows a nice dot pattern indexed for [400] and [440] planes. In figure 2.3C-E, HR-TEM images and SAED pattern for the calcined particles were shown. Here, C and D again show highly crystalline particles with lattice planes [311] and [220] corresponding to the most intense and second most intense peaks reported for bulk Co_3O_4. The SAED pattern (E) could be indexed for [331] and [440]. Here it is quite interesting to note that phase formed by the microbial method is quite pure as any indication of CoO phase was not observed. This is probably due to the fact that at
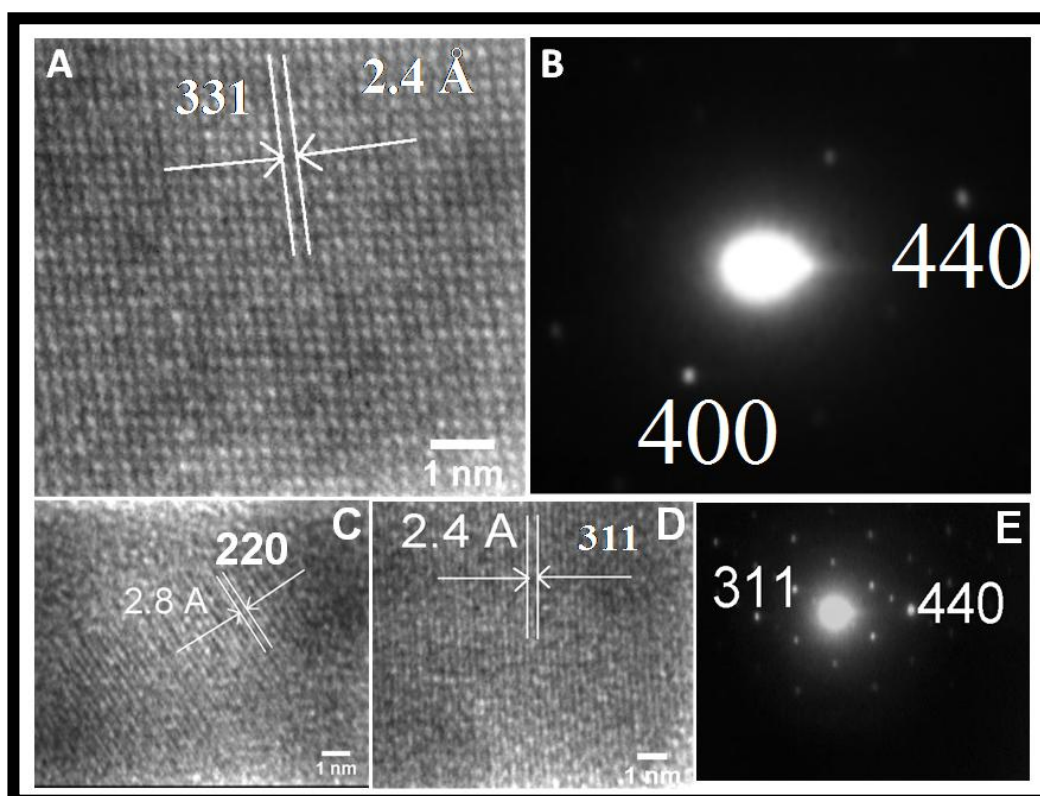
Figure 2.3: HR-TEM images and selected area diffraction (SAED) patterns for as-synthesized Co_3O_4 nanoparticles (panels A & B) and for calcined nanoparticles (panels C, D & E)

room temperature the formation of Co_3O_4 is thermodynamically favorable,[25] and only after heating Co_3O_4 above 930 °C (in reducing environment), it gets transformed into CoO phase[25].

2.4.4 X-ray Photo-electron Spectroscopy (XPS) analysis.

To investigate the purity of Co_3O_4 phase as well as presence of proteins, X-ray photoemission spectroscopy measurements were performed, which is a highly surface sensitive technique. As-obtained XPS core level spectra were background corrected using the Shirley algorithm, and chemically distinct species were resolved using a nonlinear least-squares fitting procedure. The core level binding energies (BE) were aligned with the carbon binding energy of 285 eV. In Figure 2.4, the
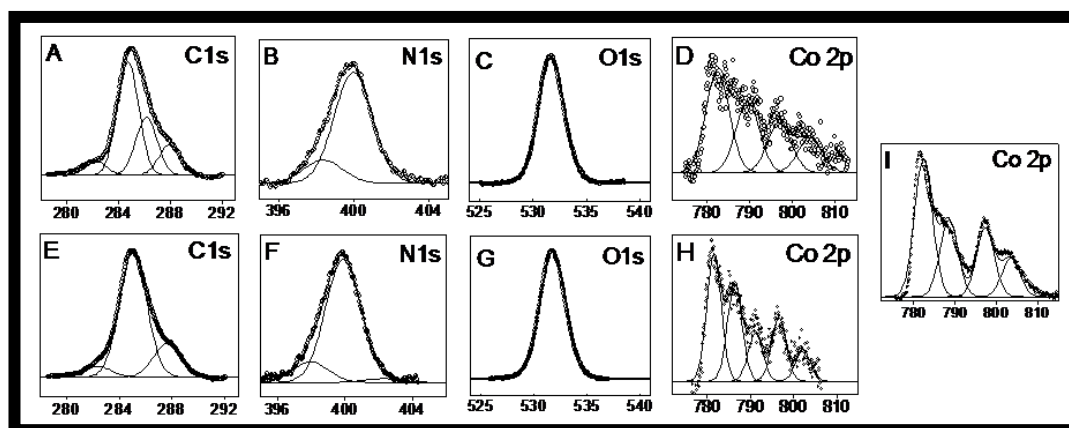
Figure 2.4: XPS spectra of as-synthesized (A-D), calcined (E-H) Co_3O_4 nanoparticles and cobalt-acetate (I). The solid lines show deconvoluted curve-fits

background-corrected XPS spectra for as-synthesized (panels A-D) and calcined (panels E-H) Co_3O_4 nanoparticles were compared. In (Figure 2.4A), the carbon 1s core level spectra shows well-defined (deconvoluted) peaks at the binding energies 282, 285, 286, and 288 eV, where the peak at 285 eV is due to the C 1s core level transition originating from hydrocarbon chains and subsequent peaks situated at 286 and 288 eV are due to the presence of R-carbon and -COOH groups present in the proteins, respectively[26]. The peak at lower binding energy of ~282 eV indicates the presence of aromatic carbon due to the protein. It should be noted that after calcination (panel E) the peak at 286 eV disappears due to the partial removal/degradation of the proteins. Panels B and F show N 1s core level spectra for as-synthesized and calcined samples where the peak at 398 eV is due to the N 1s core

level transitions and the peak at 400 eV is due to possible cationic state of nitrogen present in protein-nanoparticle complex. The peaks at 532 eV shown in panels C and G correspond to the O 1s core level transition. The peaks shown in panels D and H correspond to Co 2p core level spectra indicating the presence of four peaks at BE around 782, 788, 797, and 803 eV. Among these peaks, the peaks at binding energies 782 and 797 eV are due to spin–orbit splitting in the 2p level—$2p^{3/2}$ and $2p^{1/2}$ correspondingly with an energy gap of 15 eV. It should be noted here that shift of the peaks $2p^{3/2}$ and $2p^{1/2}$ from 778 and 793 eV correspondingly to the higher binding energies indicates absence of cobalt metal[27]. The remaining peaks at 789 and 804 eV are satellite peaks which are weaker in intensity[28,29]. For the octahedrally coordinated cobaltous ion (Co^{2+}), the $2p^{3/2}$ peak is split by nearly 6.2 eV to form a satellite peak at 788.2 eV and for the tetrahedrally coordinated one; the splitting is around 5.3 eV to form the satellite peak at 787.3 eV[28,29]. In our case, these two satellite peaks are seen as a broad peak situated at around 788 eV. On the other hand, for Co $2p^{1/2}$ levels, both 6- and 4-fold coordination ions have about 6.2 eV satellite splitting which gives the satellite peak at around 803.2 eV as seen in our case also. Overall, the cobalt 2p spectrum for Co_3O_4 is considered to be the sum of spectra of Co^{2+} and Co^{3+}. A comparison between the panels D and H show that after calcination (panel H) the peaks become more intense. To further investigate the presence of Co^{3+} in microbial synthesized Co_3O_4, we decided to compare D and H with the XPS spectra of cobalt acetate shown in panel I. In sharp contrast, we can see that the peaks in the precursor molecule (due to just Co^{2+}) are quite sharp in comparison to D and H where the peaks are quite broad, which indicates that the peak broadening in D and H is due to the contribution from Co^{3+} as well as due to the change in the chemical environment. Here it is worth mentioning that, in contrast to other neighbouring spinels such as Fe_3O_4 and Mn_3O_4; Co_3O_4 is thermodynamically stable at room temperature (surfaces of Fe_3O_4 and Mn_3O_4 readily convert to Fe_2O_3 and Mn_2O_3, respectively). In the case of Fe_3O_4 and Mn_3O_4, XPS may not show a contribution from Fe^{3+} and Mn^{3+}; however, on the other hand, Co_3O_4, being a stable phase, does show a peak corresponding to Co^{3+} as discussed above [28,29]. Another reason behind the contribution of Co^{3+} is that Co^{2+} are located at the tetrahedral sites (A) giving net magnetic moment, and Co^{3+} (diamagnetic) occupy octahedral B-sites; therefore, due to the absence of any interaction between both of these ions in photoelectron

emission process, they should give intrinsically different spectral lines which are seen as a broadened peak in our case[28,29].

2.4.5 FTIR spectra and SDS-PAGE analysis
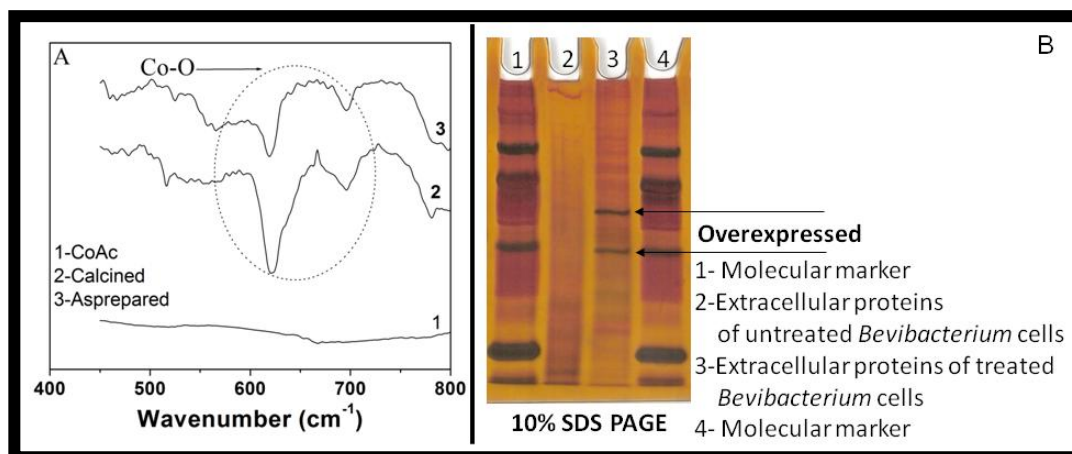
Figure 2.5: Graph showing FTIR spectra of precursor (1), calcined (2) and asprepared (3) taken in diffuse reflectance mode (A). Protein profile of extracellular proteins from *Brevibacterium casei* obtained by running 10% SDS

In order to determine the presence of bond between cobalt and oxygen (Co-O) in Co_3O_4 nanoparticles FTIR was taken for asprepared and calcined samples. Figure 2.5 A shows the FTIR spectrum recorded from the cell free extracellular supernatant, collected after 72 h of reaction between *Brevibacterium casei*. and precursor salt (cobalt acetate). In figure 2.5 A, curve-2 and 3 shows the FTIR spectra recorded from the calcined and as synthesized sample of Co_3O_4 nanoparticles respectively while curve-1 is FTIR spectra recorded from cobalt acetate alone. As expected, curve-1 does not show any Co-O vibration band specific to Co_3O_4. The stretching of Co-O bond in Co_3O_4 is usually seen at around 583 cm^{-1} and 664 cm^{-1}, whereas in this case, these peaks are shifted to 620 cm^{-1}and 695 cm^{-1} respectively[30,31]. This may be due to the change in the chemical environment because of the proteins present in the samples. Further to investigate the protein/proteins responsible for nanoparticles synthesis 10% SDS Polyacrylamide gel electrophoresis was performed for both supernantants collected from treated and untreated cells. Figure 2.5 B shows the SDS-PAGE profile obtained from the extracellular protein of *Brevibacterium casei*. culture supernatant in absence (lane-2) and presence (lane-3) of cobalt acetate. In comparison with the control (lane-2), it can be clearly observed that there are two

proteins which are overexpressed, (lane-3) that could have resulted due to the stress created by the addition of cobalt acetate to the bacterial biomass. When compared with standard protein molecular weight markers (lane-1) the molecular weight of these over expressed proteins were found to be ~ 30 and 65 kDa.

2.4.6 Bacterial morphological studies before and after exposure to precursor salt (cobalt acetate) by SEM in real time

To explore the fate of bacterial cells after their exposure to metal salts, SEM images were captured for control (without salt exposure) and cobalt acetate treated *Brevibacterium casei* cells after 24, 48, and 72 h. The results are presented in figures 2.6. In the case of control samples, it can be observed that morphology of cells remain unaltered even after 72 h (Figures 2.6A, B, D and F). On the other hand, the bacterial cells which were exposed to the precursor salt solution tend to aggregate or form clusters (Figures 2.6C, E and G), and this tendency increases gradually until 72 h compared to control cells where individual cells are clearly visible even after 72 h. This behaviour can be attributed to a kind of stress response where many bacterial strains produce excess extracellular exopolysaccharide, slime, or form capsule to protect themselves against metal ions. These capsule, slime, and bacterial acidic exopolysaccharide are known to bind and concentrate metal ions and are therefore thought to play a role in the ameliorating metal toxicity[32,33]. These secondary metabolites enforce isolated cells to clump together to form aggregates[34]. It is believed that in these self-organized colonies bacteria can be more resistive to the external stress in comparison to the suspension. Once under the external stress (such as metal ions, food scarcity, antibiotics, adverse environmental conditions, etc.) the bacteria communicate with each other following various mechanisms to cope and survive by exhibiting sophisticated cooperative structural assemblies to behave like a multicellular organism. The organizational behaviour which is a protective mechanism shown by microbes while under stress is mediated by the long-range biochemical interactions such as quoram sensing, chemotactic signaling, collective activation/ deactivation of genes, and sometimes exchange of genetic material[35,36].
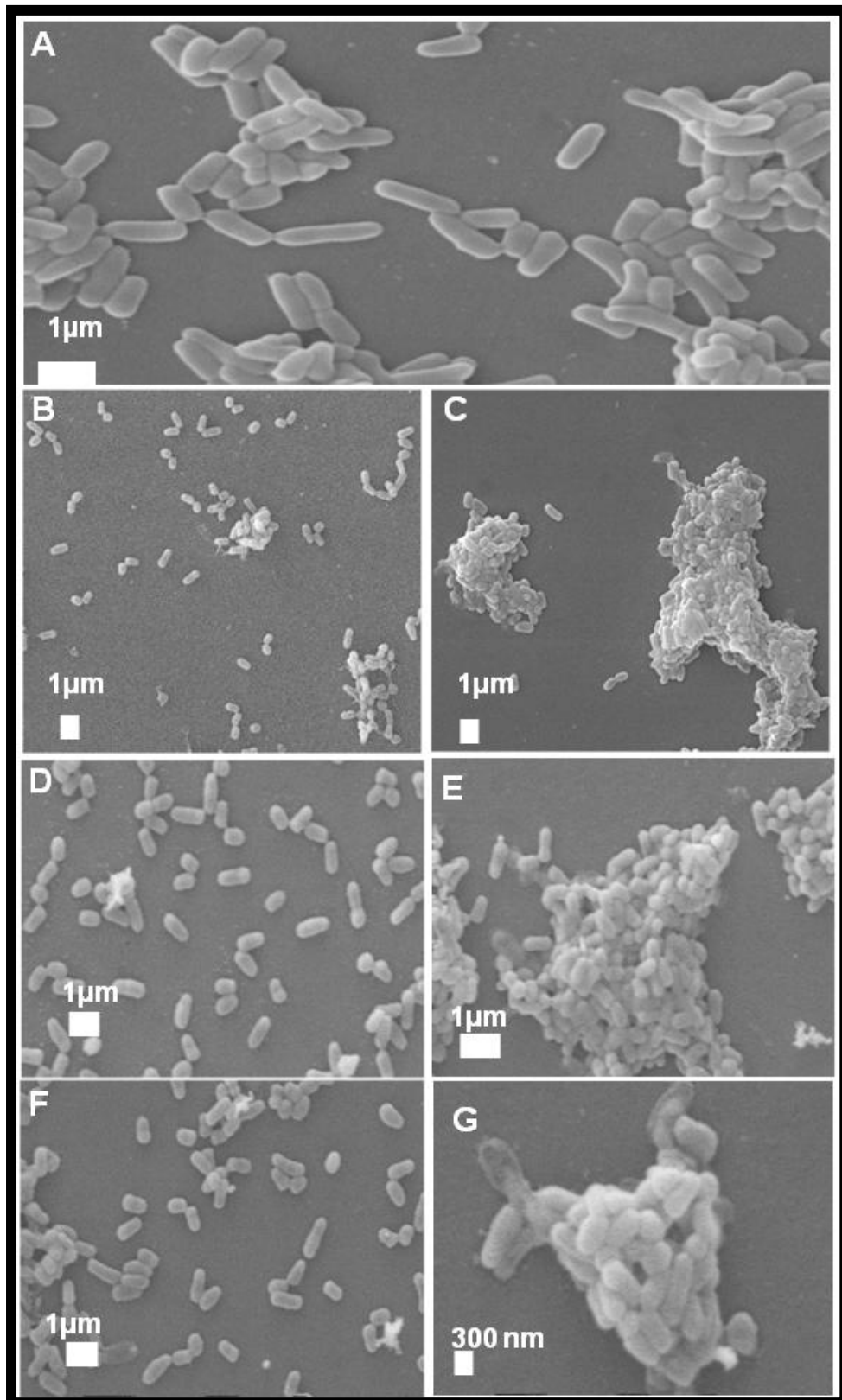
Figure 2.6: SEM images showing morphology of "control" bacterial sample (panel A). Left panel (B, D and F) and right panel (C, E and G) shows real time SEM images of same bacterial cells before and after exposure to cobalt acetate at 24 h, 48 h and 72 h respectively

2.4.7 Magnetic property measurements of Co_3O_4 nanoparticles

It is interesting to check the magnetic properties of the microbially synthesized Co_3O_4 nanoparticles. As discussed above, Co_3O_4 is known to have a normal cubic spinel structure and is antiferromagnetic in the bulk form with a Neel temperature T_N between 30 and 40 K[10]. However, in the nanosize, uncompensated spins at the particle surfaces can become a large fraction of the total number of spins thereby giving overall ferromagnetic-type behaviour, confirming that we performed magnetization vs magnetic field loop measurements at 10 and 300 K for as-synthesized and calcined samples. However, the as-synthesized sample shows dominantly diamagnetic background due to the protein and water content. The *M-H* loop on calcined sample (Figure 2.7) shows nonlinear reversible behaviour at 10 and 300 K with increase in the moment at 10 K. The *M-H* curves do not show any saturation until the highest applied field of 50 kOe which is due to the surface spin disorder, canting, etc. The reason of nonzero net moment and ferromagnetic-type behaviour in nanosize is mainly due to the nonzero moments of Co^{3+} at octahedral sites which is in turn due to the lattice defects (missing oxygen atoms) as well as the distortion of the crystal symmetry. Other reasons for nonzero magnetic moment in antiferromagnetic nanoparticles can be attributed to uncompensated spins, spin disorder, and canted spins at the surface of the particles[36].
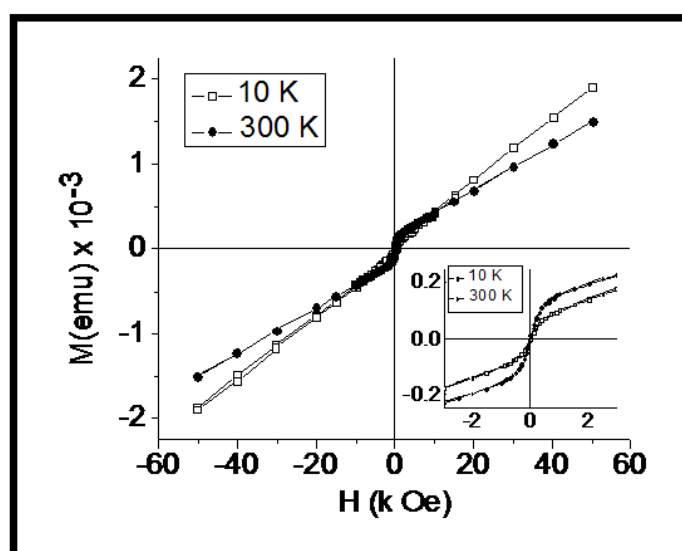
Figure 2.7: Graph showing magnetization vs magnetic field measurements of biologically synthesized Co_3O_4 (calcined) nanocrystals at 10K and 300K. The inset shows zoom view

2.5 Conclusion

Here we report for the first time that Co^{2+} was supplied to the biological system in the form of cobalt acetate, but the nanoparticles formed showed the presence of both Co^{2+} and Co^{3+} as discussed earlier. This change in oxidation state requires the presence of *Brevibacterium casei* which has been supported by our XPS studies. We believe that the change in oxidation state is either due to one of the mechanisms discussed above or because of a totally new hitherto unknown mechanism working in *Brevibacterium casei*. Such type of oxidation mechanism has been reported for other metals as well; for example, arsenite oxidase converts As(III) to As(V) and arsenate reductase converts As(V) to As(III)[37].

2.6 References

1. Dickson, D.P.E. Nanostructured magnetism in living systems. *J. Magn. Magn. Mater.* **1999,** *203*, 46–49.

2. Mann, S. (ed.) *Biomimetic Materials Chemistry* **1996,** VCH Publishers.

3. Stolz, J. F.; Basu, P.; Oremland, R.S. *Int. J. Microbiol.* **2002**, *5*, 201.

4. Bruins, M. R.; Kapil, S.; Oehm, F. W. *Ecotox. Environ. Safe.* **2000,** *45*, 198.

5. "Our Planet, Our Health"; Report of the World Health Organization on Health and Environment, Oxford University Press, Oxford, **1992**.

6. Sabry, S. A.; Ghozlan, H. A.; Abou-Zeid, D. M. *J. Appl. Microbiol.* **1997**, *82*, 245.

7. Bharde, A.; Wani, A.; Shouche, Y.; Pattayil, A. J.; Prasad, B. L. V.; Sastry, M. *J. Am. Chem. Soc.* **2005**, *127*, 9326.

8. Bansal, V.; Poddar, P.; Ahmad, A.; Sastry, M. *J. Am. Chem. Soc.* **2006**, *128*, 11958.

9. Kowshik, M.; Ashtaputre, S.; Kharrazi, S.; Vogel W.; Urban J.; Kulkarni S. K.; Paknikar K. M. *Nanotechnol.* **2003,** *14*, 95.

10. Roth, W. L.; *J. Phys. Chem. Solids.* **1964**, *25*, 1.

11. Poddar, P.; Sahoo, Y.; Srikanth, H.; Prasad, P. N. *App. Phys. Lett.* **2005,** *87*, 062506.

12. Poddar, P.; Fried, T.; Markovich, G.; Sharoni, A.; Katz, D.; Wizansky T.; Milo, O. *Eur Phys Lett.* **2003**, *64*, 98.

13. Poddar, P.; Fried, T.; Markovich, G. *Phys. Rev. B* **2002**, *65*, 172405.

14. Poddar, P.; Wilson, J. L.; Srikanth, H.; Yoo, Y. H.; Wereley, N. M.; Kotha, S.; Barghouty, L.; Radhakrishnan, R. *J. Nanosci. Nanotech.* **2004**, *4*, 192.

15. Poddar, P.; Wilson, J. L.; Srikanth, H.; Morrison, S. A., Carpenter, E. E. *Nanotechnol.* **2004**, *15*, S570.

16. Bharde, A.; Wani, A.; Shouche, Y.; Joy, P. A.; Prasad B. L. V.; Sastry, M. *J. Am. Chem. Soc*. **2005,** *127*, 9326.

17. Checa, S. K.; Espariz, M.; Audero, M. E.; Botta, P. E.; Spinelli, S. V.; Soncini, F. C. *Mol. Microbiol.* **2007**, *63*, 1307.

18. Rodrigue, A.; Effantin, G.; Mandrand-Berthelot M. A. *J Bacteriol.* **2005**, *187*, 2912.

19. Liesegang, H.; Lemke, K.; Siddiqui, R A.; Schlegel, H. G. *J. Bacteriol.* **1993**, *175*, 767.

20. Schmidt, T.; Schlegel, H. G. *J Bacteriol.* **1994,** *176*, 7045.

21. Nies, D. H. *FEMS Microbiol. Rev.* **2003**, *27*, 313.

22. Bharde, A.; Sastry, M. *J. Nanosci. Nanotechnol*. **2007.**

23. Dhakephalker, P. K.; Chopade B. A. *BioMetals.* **1994**, *7*, 67.

24. Laemmli, U. K. *Nature*. **1970**, *227*, 680.

25. Wu, R. J.; Wu, J. G.; Tsai, T. K.; Yeh, C. T. *Sensor Actuat B-chem.* **2006**, *120*, 104.

26. Bansal, V.; Rautaray, D.; Bharde, A.; Ahire, K.; Sanyal, A.; Ahmad, A.; Sastry, M. *J. Mater. Chem.* **2005**, *15*, 2583.

27. Girardon, J.; Lermontov, A. S.; Gengembre, L.; Chernavskii, P. A.; Griboval-Constant, A.; Khodakov, A. Y. *J. Cata.* **2005**, *230*, 339.

28. Oku, M.; Hirokawa, K. *J. Electron Spectrosc relat Phenom.* **1976**, *8*, 475.

29. Hirokawa, K.; Honda, F.; Oku, M.; *J. Electron Spectrosc Relat Phenom.* **1975**, *6*, 333.

30. Cao, A.M.; Hu, J.S.; Liang, H.P.; Song, W.G.; Wan L.J.; He, X.L.; Gao, X. G; Xia, S.H. *J. Phys. Chem. B* **2006**, *110*, 15858.

31. He, T.; Chen, D.; Jiao, X. *Chem. Mater.* **2004**, *16*, 737.

32. Zhang, Y.; Jock, S.; Geider K. *Mol Gen Genet.* **2001**, *264*, 732.

33. Richau, J. A.; Choquenet, D.; Fialho, A. M; Correia, I. *Res. Microbiol.* **1997**, *148*, 251.

34. Tang, Y. J.; Ashcroft, J. M.; Chen, D.; Min,G.; Kim,C. H.; Murkhejee,B.; Larabell,C.; Keasling, J. D; Chen, F. F. *Nano Lett.* **2007**, *7*, 754

35. Jacob, E. B.; Becker, I.; Shapira, Y.; Levine H. *Trends Microbiol.* **2004**, *12*, 366.

36. Jacob, E. B.; Cohen, I.; Golding, I.; Gutnick, D. L.; Tcherpakov, M.; Helbing, D.; Ron, I. G.; *Physica A.* **2000,** *282*, 247.

37. Mukhopadhyay, R.; Rosen, B. P.; Phung, L. T.; Silver, S. *FEMS Microbiol. Rev.* **2002**, *26*, 311.

CHAPTER-III

Measurement of biophysical properties of bacterial cells under stress due to the exposure of Cobalt acetate during microbial synthesis of Co_3O_4 nanoparticles

Measurement of biophysical properties of bacterial cells under stress due to the exposure of Cobalt acetate during microbial synthesis of Co$_3$O$_4$ nanoparticles
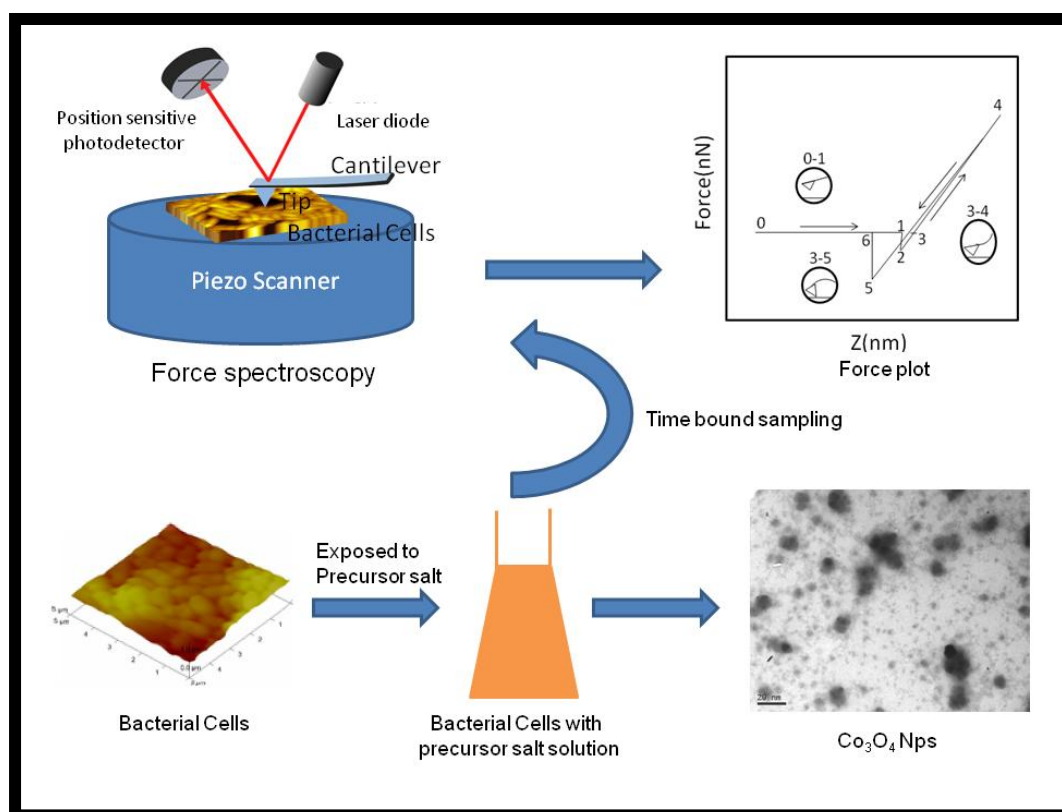
In this chapter we have shown, the use of AFM force-distance curves on bacterial cells, to directly monitor the real time changes in the surface-topography, surface-adhesion, indentation-depth, and Young's modulus of a metal-tolerant marine bacterium, *Brevibacterium casei,* isolated from the coast of the Arabian Sea after its exposure to the Co^{2+} during the process of biosynthesis of nanoparticles. This chapter describes significant changes in the morphology as well as elastic and adhesive properties of the *Brevibacterium casei*, where an increase in the adhesive properties and the indentation depth of the bacterial surfaces and a decrease in the cell stiffness after several hours of exposure to the cobalt acetate were observed. We have discussed both qualitative and quantitative analysis of the force-spectroscopy data in details in this chapter.

3.1 Introduction

A new microscopy technique, namely atomic force microscopy (AFM), emerged in the late 1990s and offered great promise for high-resolution imaging and enabling imaging under physiological conditions[1,2]. Three intrinsic advantages of this technology have attracted much attention of researchers interested in cellular biology and cellular physical chemistry. First, AFM offers high resolution. Molecular resolution, for instance, at a sub-nanometer level, was achieved for inorganic crystals[3] as well as protein crystals[4]. Applications of AFM in cellular structure characterization also proved to be very encouraging[5-7]. Important structural features, such as stress fibers, were visualized[8]. Second, time-dependent imaging in near-physiological media enabled many dynamic processes to be visualized *in situ* and in real time, such as the identification of a new membrane structure by Jena *et al.*, "the porosome", first in the apical plasma membrane of pancreatic acinar cells and subsequently in neurons, where secretory vesicles specifically dock and fuse[9-11]. Other examples include the activation of human platelets[12], the transport of intracellular particles[13], and the spreading of a Kupffer cell[14]. Third, AFM enables physical property measurements locally and globally on a single cell. For example, measuring adhesion between an AFM tip and cellular receptor, or single molecular forces[15,16], enables the mapping of the distribution of heat shock proteins (HSP) on human umbilical venous endothelial cells (HUVECs)[17].

These kind of studies were done in force spectroscopy mode which is used to measure interaction force and physical properties of biological samples. In this mode, the cantilever deflection (i.e. force signal) is recorded as a function of its vertical displacement (i.e. distance signal) as the tip approaches toward and retracts from the sample to obtain a force–distance curve (Figure 3.1). Moreover, spatial resolution can be achieved by generating a force–volume image through acquiring force – distance curves at multi-locations. The new frontier in this area is using specifically functionalized AFM tips to study protein unfolding/folding mechanisms and recognize molecular groups on cell surface[18,19]. Because of the above-mentioned unique features AFM has been used in the investigation of microbiological samples since the late 1980s, and it has become a rapidly growing field in the past decade[20-23]. Recently, atomic force microscopy (AFM) has turned out to be the instrument of

choice to image cells in their physiological environment both statically and dynamically. AFM is currently the only technique that can image the surface of a living cell down to molecular level resolution and in real time. Thus its importance in the surface science of cellular systems is well beyond being just a complementary technique to electron microscopy for topographical mapping.

The main advantage of using AFM at a relatively lower resolution (micrometer level) is that the dynamic events, such as the cell growth, budding processes, and changes in the cell surface morphology resulting from the treatment with external agents (e.g., enzymes and antibiotics), can be directly tracked in real time, providing a wealth of information. In this technique, either the bacterium is attached to the AFM tip[24] or the tip is used to probe the bacterium[25]. Additionally, using force spectroscopy (force distance curves), it is possible to precisely get quantitative information about elasticity, plasticity, adhesiveness, and the indentation-depth of the materials, including polymers, biological materials, thin films, etc. at the nanolevel[26]. In simpler words, it is a record of the controlled approach and interaction of the tip and sample where the force involved such as the electrostatic, magnetostatic, van-der Waals, capillary, and adhesive forces, etc. can be probed at a level down to the pico-Newton. As we indicated earlier, the potential of AFM for stable imaging as well as the acquisition of force-distance curves on the living cells for extended time periods facilitates the study of dynamic processes due to the external stimuli, which is not possible by any other method. Simply, we can say that AFM technique relies on a basic principle where a sample attached to a piezoelectric positioner is rastered beneath a sharp tip attached to a sensitive cantilever spring. Undulations in the surface lead to the deflection of the cantilever, which is monitored optically using a photodiode. Usually a feedback loop is employed, which keeps the cantilever deflection constant and the corresponding movement of the piezoelectric positioner thus generating the image[27-29]. There are several reports in the literature, where the force-distance spectroscopy has been extensively and successfully used to locally measure the elastic properties of cellular systems using it as a nanoindentation technique[30-36]. It is now understood that the stiffness of a cell surface, as observed by the indentation with an AFM tip, may originate from various sources such as (a) the cell wall itself and/or (b) underlying structures (cytoskeleton etc.) and/or (c) the pressure difference between the cell

interior and the exterior. Arnoldi et al. presented a theoretical model taking into account different contributions to measure the cell stiffness by osmotic pressure inside the bacterium (turgor pressure), the bending elasticity of the cell wall, and the surface tension. The application of this model to the indentation curves on the bacterium *Magnetospirillum gryphiswaldense* showed that the measured cell response is dominated by the turgor pressure of 105 Pa. Similar values of the turgor pressure were also found for the *Pseudomonas aeruginosa* and *Enterococcus hirae* bacteria[37]. It is reported in the literature that for the live mammalian cells, for example, liver endothelial cells, the typical values of the elastic modulus are around 2 kPa and more than 100 kPa for the glutaraldehyde fixed cells[38]. Various groups have seen a similar effect for the *E. coli* K12 strains, where a 4-fold increase in the cell stiffness was found due to the cell fixation.10 Higher values of the Young's modulus were also reported for isolated sheaths of the archeaon *Methanospirrilum hungatei* GP1 (20-40 GPa)[39]. In fact the force-plot measurements can also be used to differentiate between the normal cells and the cancerous cells[40]. It was reported that in the case of living lung carcinoma cells, Young's modulus ranges from 0.013 to 0.1 MPa[31] whereas in the human platelets this value is in the range of 1-50 kPa[32]. In the case of prokaryotic cells such as *B. subtillis,* the value of Young's modulus is as high as 50 MPa whereas in case of eukaryotic cells such as *S. cerevisiae*, it is up to 110 MPa[41].

Hence due to the sensitive nature of this technique, we have used this technique to answer a few of the fundamental questions related to the cell-mechanism during the biosynthesis after exposure to the Co^{2+}. Below we present our results on the force-distance spectroscopy to understand the effect of Co^{2+} exposure during the synthesis of Co_3O_4 nanocrystals on the *Brevibacterium* cells. A detailed quantitative and qualitative analysis of the changes in the nanomechanical properties of cells such as Young's modulus, indentation depth, and adhesiveness is discussed in this chapter.

3.2 Materials and methods

For the atomic force microscopy measurements, the bacterial cells grown in Zobell medium were harvested after incubation of 24 hours at 27 ℃ and 200 rpm. These

cells were washed twice with Millipore water followed by centrifuging the cells at 6000 rpm for 5 min. Finally these cells were resuspended in Millipore water and drop-casted on the freshly cleaved mica substrates for the AFM measurements. For the real time observation of the Co^{2+} toxicity effects on the cells, the cells were incubated with an aqueous solution of cobalt acetate. In this case the concentration of the cobalt acetate was similar to the concentration used in our earlier study for the synthesis of Co_3O_4 nanoparticles using the *Brevibacterium casie* culture (Previous chapter). The cells were drop casted on the mica surfaces after 24, 48, and 72 hour of incubation to study a time dependent effect on the cell physiology, and these results were compared with those of the untreated cells (control i.e. 0 hour). Therefore this study truly represents the changes in the morphology and mechanical properties during as well as after the biosynthesis of the Co_3O_4 nanoparticles. Here the 0 hour measurement corresponds to the time prior to reaction, the sample taken after 24 hour of incubation corresponds to the measurements "during" the synthesis process and the corresponding surface changes on bacterial cells, and the 48 h sample represent the time-scale after completion of the synthesis process and reflects the corresponding surface changes. Lastly, the 72 hour sample corresponds to the time interval well beyond the formation of nanoparticles. The atomic force microscopy measurements were performed using a Multimode scanning probe microscope equipped with a Nanoscope IV controller from Veeco Instrument Inc., Santa Barbara, CA. All the AFM measurements were carried out under ambient conditions using the soft tapping mode AFM probes model-Multi75Al purchased from Budget Sensors, with proper precautions to avoid drying of the cells. The radii of tips used in this study were less than 100 nm, and their height was 17 μm. The probe used had a resonant frequency of 75 kHz with a 30 nm thick aluminum reflex coating on the back side of the cantilever of the length 225 μm, and it was characterized for the force constant using the thermal noise method[42] using a Nanoscope V controller from Veeco Instruments. The measured force constant was around 1.86 N/m (soft enough for the biological cells). It is worth mentioning here that it is important to measure the exact value of the force constant to convert the cantilever deflection and tip-sample distance curve into the force-distance curve. The soft cantilevers are susceptible to thermal fluctuations, which can be measured and analyzed (cantilever movement) by AFM. The thermal noise spectrum is a plot of cantilever fluctuations

as a function of frequency; usually the greatest amplitude will be seen around the cantilever resonance frequency, where there will be a maximum energy transfer. The amplitude of fluctuations at a given temperature depends entirely upon the spring-constant of the cantilever[43]; therefore, the thermal resonance curve can be fitted into a Lorentz function which allows calculation of the spring-constant. The deflection sensitivity of the cantilever was calibrated at the end of the measurements by drawing a line parallel to the 2-4 segment of a typical force plot curve (figure 3.1), where the tip is already in contact with the hard surface, obtained on a freshly cleaned silicon substrate which converts the cantilever deflection value, which is
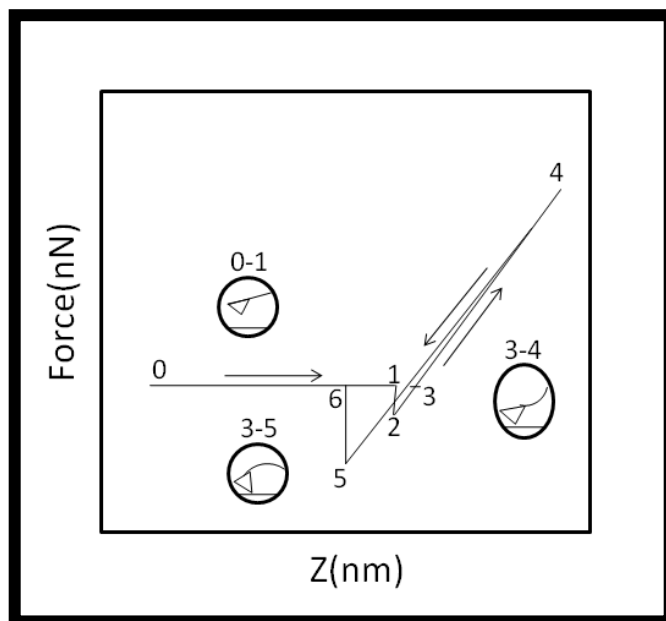
Figure-3.1: Schematic diagram of typical force plot curve showing its different parts

generated in Volt units from the photodiode detectors, to distance units (the actual cantilever deflection in nanometers). The calibration on the hard surface ensured that the indentation depth is zero while doing the deflection sensitivity measurements. As we know that deflection sensitivity is different for each cantilever and changes with the cantilever length, thickness, coating, and contamination, etc. Besides this cantilever sensitivity also depends on the position of the laser light on the cantilever as well as the quality of the laser beam reflection (spot size, shape) from the cantilever. Therefore all the necessary precautions were taken to have reproducible deflection sensitivity.

3.3 Results and discussion

The loading and unloading cycles during force-distance measurements were shown as schematic diagram in figure 3.1. The region "0-1" of the schematic diagram, when the tip starts approaching the sample surface and the separation between them is approximately 10-100 μm, there is no interaction between the tip and the sample. Typically, for a tip-sample separation of a few micrometers to few tens of nanometers, the long-range electrostatic forces contribute to the approach part of a force-distance curve. When the separation reduces to below few tens of nanometers, magnetostatic, van-der Waals, capillary, and other short-range forces play a predominant role shown by region 0-1 in the schematic diagram just before the jump into contact point. At around position 1, when the tip-sample separation is hardly a few atomic distances, the tip comes into contact with the sample. Position 1 is also called the jump-into-contact point, where the tip is pulled toward the sample due to the capillary, van der Waals forces. The segment "3-4" of the schematic diagram represents the event when the tip presses the sample surface and the cantilever bends upward. This region is very informative as it gives an idea of the stiffness (Young' modulus, elastic or plastic response, and viscoelastic response etc.) of the sample. The segment "4-6" indicates that the tip is lifting-off the sample surface (a few atomic distances to nanometers). This region gives an idea about the adhesive properties of the sample which can be specific (ligand-receptor) or nonspecific (chemical affinity, surface coatings etc.). Precisely the segment "5-6" of the figure 3.1 shows the point where the tip leaves contact with the surface. This is also known as jump-off contact. It gives an idea of the adhesive forces, as we shall discuss ahead in this chapter[41]. It can be noticed that almost each part of the force-distance curves carries significant and precise information about the tip-sample interaction. Surface topography of the untreated cells assembled on the mica surface in 5 μm range using the cantilever deflection image (error signal mode) was shown in figure 3.2 (left panel), where a nice closed packed structure of the microbial cells without any visible surface deformation or damage was observed. In the right panel of the same figure, the section analysis of the untreated cells was shown. It is well known fact that, in the microbial imaging due to roughness of the samples, the deflection image provides much detailed information in comparison to the height image; therefore we
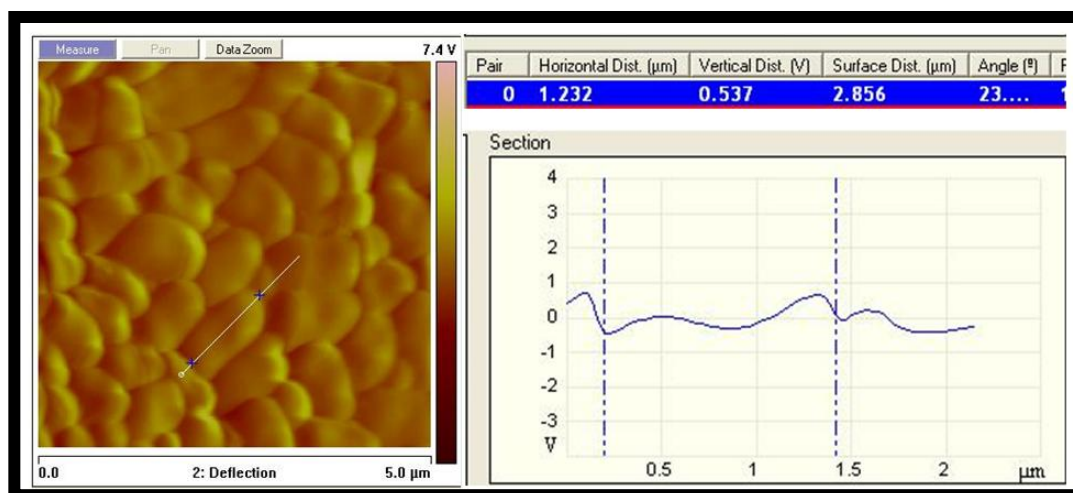
Figure 3.2: Deflection image of untreated *Brevibacterium* cells (0 h) where size of typical bacterial cell is measured

chose to present our data only the deflection images. The surface topography of the cells incubated with the cobalt acetate is shown in figure 3.3; left, middle, and the right panels depict the topography (deflection) images after 24, 48, and 72 hours. The image after 72 hours was not captured as this is the maximum time required for the
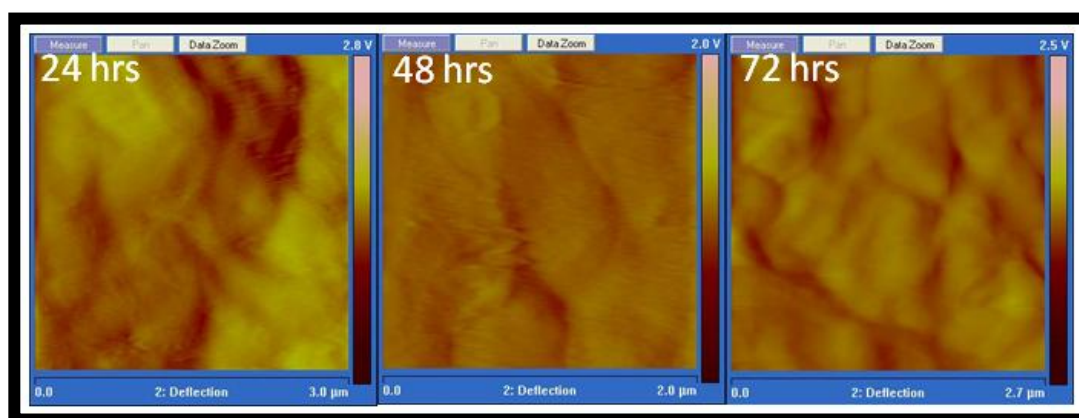
Figure 3.3: Deflection image of *Brevibacterium* cells treated with 1mM cobalt acetate solution after 24, 48 and 72 hrs

complete synthesis of Co_3O_4 nanoparticles. In comparison to the earlier image of the untreated cells (figure 3.2), a remarkable deformation in the cellular structure, particularly with respect to aggregation of the cells, which increases as a function of time (from 24 to 72 hours) due to the increasing exposure to Co^{2+} was clearly

observed. In earlier chapter the mechanism behind the aggregation and deformation of the cells in response to the precursor salt, 1mM cobalt acetate, was explained in detail. We believe that this is a kind of stress response where many bacterial strains produce excess extracellular exopolysaccharide or slime or form capsules to protect themselves against the metal ions. Capsules, slime, and bacterial acidic exoploysaccharide are known to bind and concentrate metal ions and are therefore thought to play a considerable role in ameliorating metal toxicity. These secondary metabolites enforce isolated cells to clump together to form aggregates. It is believed that in these self-organized colonies bacteria can be more resistive to the external stress in comparison to the cells in suspension. Once under the external stress such as metal ions, food scarcity, antibiotics, adverse environmental conditions etc. the bacteria communicate with each other following various mechanisms to cope and survive by exhibiting sophisticated cooperative structural assemblies to behave like a multicellular organism. This organizational behaviour which is a protective mechanism shown by microbes while under stress, is mediated by series of biochemical interactions such as quoram sensing, chemotactic signaling, collective activation/deactivation of genes, and sometimes the exchange of genetic material. To further explore the effect of the exposure of the cells to the Co^{2+} such as presence of exopolysaccharide at the cell surfaces leading to their aggregation as mentioned above and to see the change in their nanomechanical behaviour due to the deformation during the microbial synthesis of Co_3O_4 nanoparticles, force-distance spectroscopy measurements were performed on several cell samples taken both during and after the synthesis of nanoparticles. For this purpose, the desired bacterial cell was focussed after getting the topography image (figure 3.3) and the force-distance data was collected at the center of each cell. Results on the cells treated with 1 mM cobalt acetate for 24, 48, and 72 hours are presented in figure 3.4; obtained keeping the speed of loading and unloading at 598 nm/s, which is acceptable for the cellular systems. It should be noted that too high speed may lead to the distortion of elastic response. The force-distance curves are also influenced by the time of interaction and the load as well as the physicochemical and mechanical changes of the cell surfaces caused by the cell immobilization. Taking these factors into account, we performed the force-distance measurements on the control (figure 3.4, top-left panel) samples and all the AFM parameters were kept unchanged (interaction time,

protocol for cell immobilization, load etc.). Spring-constant value of 1.86 N/m is used to convert the cantilever deflection (nm) versus tip-sample distance (nm) curves into the force (nN)-distance (nm) curves. The force exerted on the sample during force measurements can be calculated using the relation

$$F = kd \qquad (1)$$

where k is the spring constant of the cantilever and d is the deflection produced by the cantilever as a consequence of interaction between the tip and the sample surface. The x-axis in these curves presents the distance travelled by the piezotube toward the sample, and the y-axis shows the force experienced by the cantilever after interacting with cells (in nano- Newtons). Details of the information represented by various parts of the force-distance curve (loading-unloading cycles) were discussed earlier in figure 3.1. From the "contact" regions of all the force-distance curves shown in the figure 3.4, it was noticed that there is a significant difference between the approach and retract branches of the curves apart from being slightly nonlinear. For ideal elastic or hard surface there should not be any deviation or hysteresis in the contact region. Hence the approach and withdrawal contact lines must overlap and the retract curve should also cross the zero force level at the point where the approach curve touches the zero force point after jumping to contact the surface[31]. However, if the surface of the sample is plastically deformable then during approach of the AFM tip, the sample undergoes a deformation, and in the retract cycle, the sample does not regain its original shape. It is considered that most of the samples show a mixed (plastic and elastic) behaviour and the approach and retract curves rarely overlap on each other as seen in the present case. This can also happen due to a small hysteresis in the piezo in Z movement. In this case, the deviation in both the curves is due to the plasticity (irreversible deformation) of the cell surfaces, which is also visible from the indent left at the cell surface after the measurement. The best way to check the instrument related artifact is to carry out the force-distance measurements on the hard surface. We performed this measurement on the silicon surface and did observe only a small hysteresis in the contact region.[16] Therefore we conclude that, in case of *Brevibacterium*, the deviations in both the curves are primarily due to the plasticity (irreversible deformation) of the cell surfaces. Additionally, the fact that the retrace curve is falling behind the trace curve also proves the plastic behaviour of cells. It
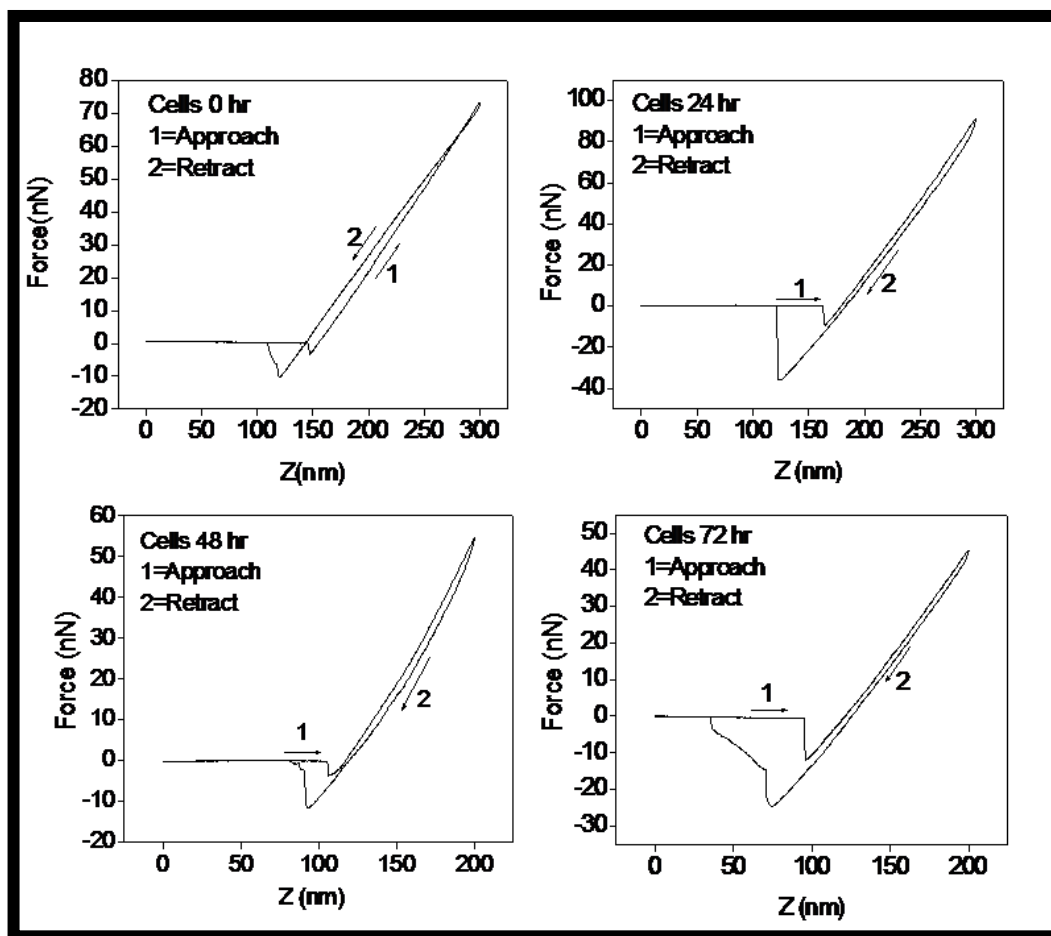
Figure 3.4: The force-distance curves obtained with control (0hr) and treated *Brevibacterium* cells (24, 48 and 72 hr)

should be noted that usually microbial cells do not show such type of behaviour due to the presence of a rigid cell wall. However in this case, due to exposure to the metal ions during Co_3O_4 nanoparticles synthesis and due to drying or dehydration during sample preparation, the cells might show such type of plastic behaviour of their surfaces. This is for the first time where a clear change in the topography of the microbial cells as well as their mechanical behaviour has been observed during nanoparticles synthesis. The nonlinearity in the contact region is again the signature of the presence of the soft and deformable sample where the contact region of the curve is a convolution of the viscoelesatic property of the sample and that of the cantilever, as against the nondeformable tip or samples, the contact region should be perfectly linear[44]. Another important feature about the curves presented in figure 3.4 is the onset of the "jump-into the surface" region, which is characterized by the point

where the gradient of the attractive force exceeds the spring constant[31]. This feature is due to the attractive forces such as capillary forces and van der Waals forces between the tip and the sample surface. These are mostly present under ambient conditions, as we discussed earlier. Some groups have reported not to observe the "jump-to-contact" region in their force-distance curves of the bacterial cells. However, we believe that their observation is due to the dominant electrostatic repulsion where both the bacterial cells and the AFM tip were probably negatively charged, thereby masking the effect of the capillary forces[45]. In fact, in almost all the cases under normal relative humidity, the capillary forces are also strong enough to mask the van der Waals forces. The absolute linearity of the approach or retract curve in the noncontact region of the force curve shows absence of any long-range attractive or repulsive forces in case of *Brevibacterium* cells used for Co_3O_4 nanoparticles synthesis.

3.3.1 Calculation of adhesive force and adhesion energy on microbial cell surface

An additional hysteresis behaviour seen in figure 3.4 is discussed in this section. This is observed as a large difference in horizontal (Z) position of the jump-to-contact and jump-off contact points (also shown as regions 2 and 6 in the figure 3.1), which shows up due to the tip-sample interaction and is a signature of the presence of strong adhesion forces between tip and cellular surface probably originating from the exopolysaccharide and other biomolecules at the surface. In normal imaging, this adhesion loop is usually checked (on hard surface) to estimate the cleanliness of the tip, and it should be minimized. However, in the present case, we have used it to provide a quantitative evaluation of the variation of the adhesive forces at the cell surfaces during the exposure to the Co^{2+} in biosynthesis. In fact, the area under the adhesion loop (in the absence of Z-piezohysteresis) represents the work done in the approach-retract cycle against the tip-sample interaction. The amount of force required to snap the tip off the cell surface is given by the force just before the jump-off contact and gives a measurement of the maximum tip-sample adhesion. However, the measured adhesion force also depends on the time scale of the retraction; that is, the faster the curve, the lower the adhesion. In present case, the time taken for the

retract curve was around 0.3 s, which is quite reasonable. The adhesive force calculated by the force plot comes out to be 10, 40, 15, and 25 nN after 0 (control), 24, 48, and 72 hours of exposure of the cells to metal ions during the microbial synthesis of Co_3O_4 nanoparticles, respectively. We calculated the adhesion energy for various samples by calculating the area under the force-distance curve below the zero force line of the adhesion loop (refer to the schematic diagram shown in figure 3.1), and these values were 0 h = -177.073 × 10-18 J, 24 h = -1211.45 × 10-18 J, 48 h = -197.01 × 10-18 J, and 72 h = -1067.49 × 10-18 J. It is clear that the adhesive force and adhesive energy show an enhancement during the biosynthesis after the exposure of the bacterial cells to the metal ions, which is probably due to the presence of an increasing amount of exopolysaccharide and other biomolecules at the surface as the microbial reaction proceeds. To assess whether the cells have undergone physiological changes upon treatment with the cobalt acetate as reaction time evolves during the synthesis of Co_3O_4 nanoparticles, it is required now to do further quantitative analysis to calculate the indentation depth from the force spectroscopy data on the treated cells at 0, 24, 48, and 72 hours. The indentation made by the tip on the cell surface during the force measurements is quantified by the indentation depth, δ, which can be calculated following the schematic presentation shown in figure 3.5 using the relation :

$$\delta = d_1 - d_2 \qquad\qquad (2)$$
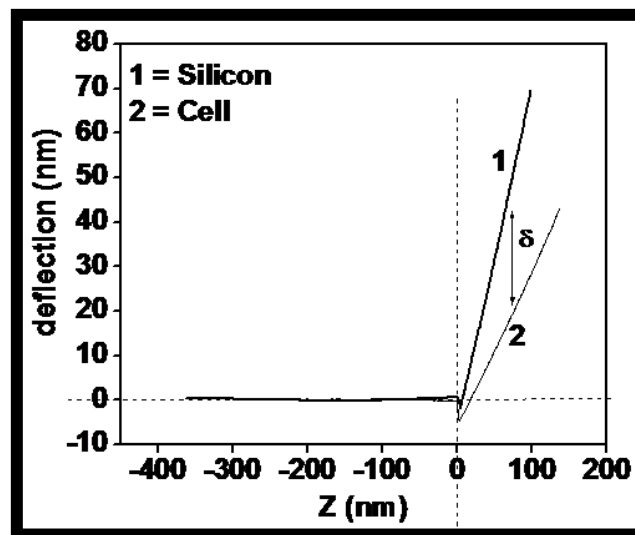
Figure 3.5: Schematic picture showing the method used for indentation depth calculation

where d_1 and d_2 correspond to the deflections produced by the approach curves on a hard surface such as silicon (where the indentation would be essentially zero) and a sample of interest, respectively[41]. In the schematic diagram shown in figure 3.5, we have explained the procedure that we followed to calculate the indentation depth at various load values in the contact region. In this method, as a first step, the offsets in the deflection and the stresses on the cantilever were taken into consideration. In the second step, the point at which jump into contact occurs due to the instability between the tip and the sample is made common for both the silicon reference and the sample, as shown in schematic figure 3.5. Indentation depth versus force curves (cantilever deflection) for various time-scales of Co^{2+} ion exposure during the synthesis was shown in figure 3.6. It is clear that the indentation depth inside the
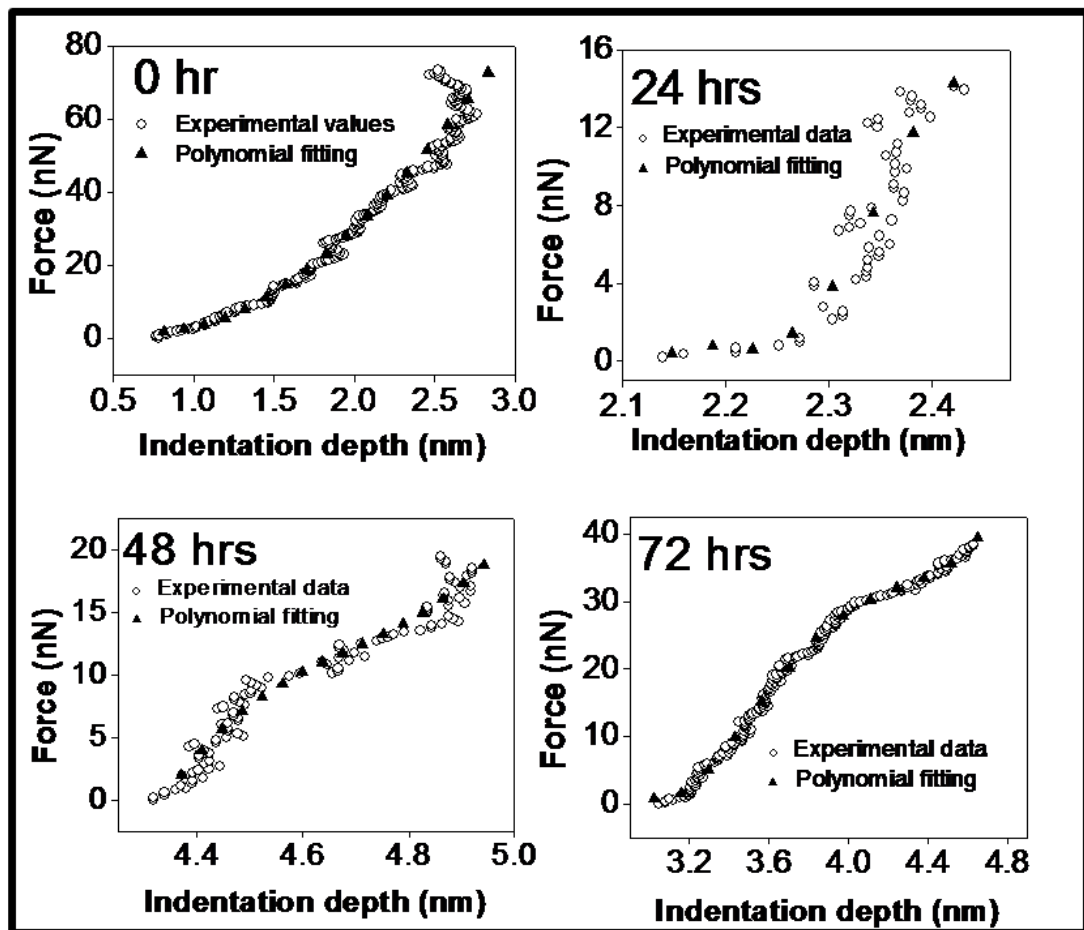
Figure 3.6: Loading force as a function of indentation depth for 0 hr, 24 hrs, 48 hrs and 72 hrs and their polynomial fits as calculated from the force-distance curves

cells generally increases with increasing force applied at the cell surface. It is interesting to know however that, for a typical applied force (say 10 nN), the indentation depth calculated for the untreated cells (0 hour) is smallest and the indentation depth shows an overall increasing trend as the reaction progresses, which is probably due to an overall decrease in the stiffness of the cell surface during the synthesis as the exposure time to the metal ions increases.

These results clearly indicate a sharp change in the nanomechanical properties of cells after exposing them to the toxic environment of transition metal ions. As already mentioned, the nanomechanical properties of cells such as Young's modulus are extremely sensitive to the surrounding environment; therefore, next, we calculated the Young's modulus values for each step, before, during, and after the synthesis of Co_3O_4 nanoparticles (various levels of exposure to the metal ions) using the Hertz model[46,47]. A more generalized model given by Sneddon et al. is an extension of the Hertz model which takes into account the contribution from the deformable tip[41]. The Hertz model is a good choice for calculating the Young's modulus of cells, as this model assumes that it is the sample alone undergoing deformation during the tip-sample interaction rather than the tip itself which is very stiff in comparison to the biological material, as the Young's modulus for the AFM tips for silicon or silicon nitride is several orders of magnitude higher than that for cells.

3.3.2 Calculation of Young's modulus

Assuming the tip shape to be spherical or paraboloid, the Young's modulus, *E*, according to the Hertz model is given by the relation :

$$E = \frac{(1-\sigma^2)}{4R^{\frac{1}{2}} \delta^{\frac{3}{2}}} \qquad (3)$$

where F is the force experienced by the cantilever and the indentation depth, δ, can be obtained from equations 1 and 2, respectively. R is the radius of curvature of the tip used for the force measurement (estimated to be around 100 nm), and σ is Poisson's ratio. The value of Poisson's ratio always comes in the range from 0 to 0.5, but for the biological cells, σ typically lies in a range from 0.3 to 0.5.[47,48]. In the present case, we have taken Poisson's ratio as 0.5, assuming the cells to be incompressible during the force measurements. The calculated values of the Young's modulus using eq (3) at various levels of reaction as a function of indentation depth, is shown in figure 3.7. It should be noted that as the biological cells are inhomogeneous systems, their elastic properties varies with the indentation depth of
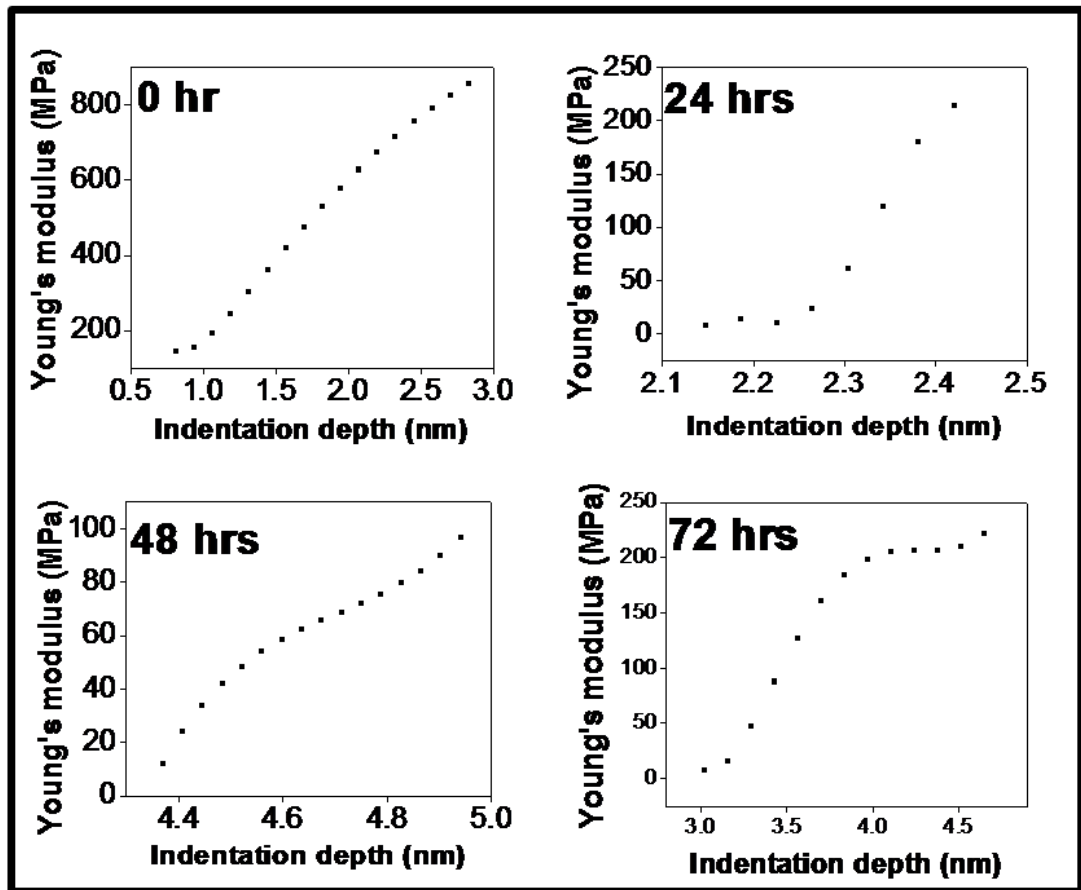

Figure 3.7: Typical Young's moduli values as a function of indentation depth calculated using the Hertz model for 0, 24, 48 and 72 hrs

the material. From figure 3.7, we infer that for the control sample (0 hour) the Young's modulus shows a gradual increase as a function of indentation depth as

compared to the rest of the curves (for 24, 48, and 72 hours after the reaction starts). It is also evident that, for larger indentation depth values, an approach toward a plateau in the Young's modulus values is seen for almost all the four cases. Usually this situation arises when the applied load is proportional to the deformation produced in the sample, indicating that the region is in the elastic limit. In this region, the calculated values for Young's modulus for 0, 24, 48, and 72 h of reaction are 769.28 (73.07 MPa, 170.921 (38.93 MPa, 82.860 (20.42 MPa, and 209.526 (6.14 MPa, respectively, which shows mostly a decreasing trend in elasticity of the cells as the reaction progresses. As we discussed earlier, it is believed that the Young's modulus of a cell surface may originate from various sources such as (a) the cell wall itself and/or (b) underlying structures (cytoskeleton etc.) and/or (c) a pressure difference between the cell interior and the exterior (turgor pressure). The metabolic processes inside the cells and at the cell surface might be greatly affected by the presence of Co^{2+}, leading to the loss of turgor pressure and change in the elastic properties of the cell wall itself as well. As seen in the topographical images of the cells, we can conclude that these factors collectively lead to an overall drop in the elasticity in case of *Brevibacterium* cells, although the approach to the plateau of Young's modulus as a function of indentation depth is faster in the 0 and 24 hours samples. This saturation point is different for each sample depending upon their exposure to the Co^{2+}, probably due to the clumping of cells during the microbial synthesis of Co_3O_4 nanoparticles. Unexpected high values of Young's modulus for the 0 h sample (before reaction) indicate that the turgor pressure is maintained. As the reaction progresses, we notice a decrease in the Young's modulus values and softness of the sample, which is probably due to loss of turgidity during the synthesis process.

3.4 Conclusion

In summary, our force-spectroscopy measurements on the microbial cells show an overall decrease in the Young's modulus value and an increase in the adhesiveness due to the secretion of the proteins and other biomolecules at the cell surfaces during interaction of the cells with the cobalt acetate during the synthesis of Co_3O_4 nanoparticles. We believe that this is a kind of study where a detailed quantitative

and qualitative analysis before, during, and after the microbial synthesis of Co_3O_4 nanoparticles indicates the sensitivity of the micromechanical properties of cells to the surrounding toxic environment.

3.5 References

1. Binnig, G.; Quate, C. F.; Gerber, C. *Phys. Re*v. *Lett.* **1986**, *56*, 930.

2. Drake, B.; Prater, C. B.; Weisenhorn, A. L.; Gould, S. A. C.; Albrecht, T. R.; Quate, C. F.; Cannell, D. S.; Hansma, H. G.; Hansma, P. K. *Science* **1989**, *243*, 1586.

3. Ohnesorge, F.; Binnig, G. *Science* **1993**, *260*, 1451.

4. Muller, D. J.; Buldt, G.; Engel, A. *J. Mol. Biol.* **1995**, *249*, 239.

5. Butt, H. J.; Downing, K. H.; Hansma, P. K. *Biophys. J.* **1990**, *58*, 1473.

6. Radmacher, M.; Tillamnn, R. W.; Fritz, M.; Gaub, H. E. *Science* **1992**, *257*, 1900.

7. Haberle, W.; Horber, J. K. H.; Binnig, G. Force Microscopy on Living Cells **1991**.

8. Hofmann, U. G.; Rotsch, C.; Parak, W. J.; Radmacher, M. *J. Struct. Biol.* **1997**, *119*, 84.

9. Schneider, S. W.; Sritharan, K. C.; Geibel, J. P.; Oberleithner, H.; Jena, B. P. *Proc. Natl. Acad. Sci. U.S.A.* **1997**, *94*, 316.

10. Jena, B. P. *J. Cell. Mol. Med.* **2004**, *8*, 1.

11. Jena, B. P. *Mol. Cells* **2008**, *26*, 517.

12. Fritz, M.; Radmacher, M.; Petersen, N.; Gaub, H. E. *J. Vac. Sci. Technol. B* **1994**, *12*, 1526.

13. Schoenenberger, C. A.; Hoh, J. H. *Biophys. J.* **1994**, *67*, 929.

14. Rotsch, C.; Braet, F.; Wisse, E.; Radmacher, M. *Cell Biol. Int.* **1997**, *21*, 685.

15. Ebner, A.; Madl, J.; Kienberger, F.; Chtcheglova, L. A.; Puntheeranurak, T.; Zhu, R.; Tang, J. L.; Gruber, H. J.; Schutz, G. J.; Hinterdorfer, P. *Curr. Nanosci.* **2007**, *3*, 49.

16. Dufrene, Y. F.; Hinterdorfer, P. *Pflugers Arch.* **2008**, *456*, 237.

17. Pfister, G.; Stroh, C. M.; Perschinka, H.; Kind, M.; Knoflach, M.; Hinterdorfer, P.; Wick, G. *J. Cell Sci.* **2005**, *118*, 1587.

18. Dufrene, Y. F. *Analyst.* **2008a,** *133*, 297.

19. Muller, D.J.; Krieg, M.; Alsteens, D.; Dufrene, Y. F. *Curr Opi Microbiol.* **2009**, *20*, 4.

20. Dufrene, Y. F. *Curr Opin Microbiol.* **2003,** *6*, 317.

21. Dupres, V.; Alsteens, D.; Andre, G.; Verbelen, C.; Dufrene, Y. F. *Nano Today.* **2009,** *4*, 262.

22. Hinterdorfer, P.; Dufrene, Y. F. *Nat Methods.* **2006,** *3*, 347.

23. Morris, V. J.; Kirby, A. R.; Gunning, A. P. *Imperial College Press, London.* **1999**.

24. Razatos, A. P.; et al. *Abs. Pap. Am. Chem. Soc.* **1998**, *216*, U271.

25. Velegol, S. B.; Logan, B. E. *Langmuir* **2002**, *18* (13), 5256.

26. Butt, H. J.; Cappella, B.; Kappl, M. *Surf. Sci. Rep.* **2005**, *59* (1-6), 1.

27. Binnig, G.; Quate, C.; Gerber, G. *Phys. Rev. Lett.* **1986**, *56*, 930.

28. Binnig, G.; Rohrer, H. *Helv. Phys. Acta* **1982**, *55*, 726.

29. Ralston, J.; Larson, I.; Rutland, M. W.; Feiler, A. A.; Kleijn, M. *Pure Appl. Chem.* **2005**, *77* (12), 2149.

30. Burnham, N. A.; Colton, R. J. *J. Vacuum Sci. Technol. A* **1989**, *7*, 2906.

31. Weisenhorn, A. L.; Khorsandi, M.; Kasas, S.; Gotzos, V.; Butt, H. *Nanotechnology* **1993**, *4*, 106.

32. Radmacher, M.; Fritz, M.; Kacher, C. M.; Cleveland, J. P.; Hansma, P. K. *Biophys. J.* **1996**, *70* (1), 556.

33. Tomasetti, E.; Legras, R.; Nysten, B. *Nanotechnology* **1998**, *9*, 305.

34. Rotsch, C.; Jacobson, K.; Radmacher, M. *Proc. Natl. Acad. Sci.U.S.A.* **1999**, *96* (3), 921.

35. Matzke, R.; Jacobson, K.; Radmacher, M. *Nat. Cell Biol.* **2001**, *3* (6), 607.

36. Radmacher, M. *At. Force Microsc. Cell Biol.* **2002**, *68*, 67.

37. Arnoldi, M.; Fritz, M.; Bauerlein, E.; Radmacher, M.; Sackmann,E.; Boulbitch, A. *Phys. Rev. E* **2000**, *62* (1), 1034.

38. Braet, F.; Rotsch, C.; Wisse, E.; Radmacher, M. *Appl. Phys. A: Mater. Sci. Proc.* **1998**, *66*, S575.

39. Xu, W.; Mulhern, P. J.; Blackford, B. L.; Jericho, M. H.; Firtel, M.; Beveridge, T. J. *J. Bacteriol.* **1996**, *178* (11), 3106.

40. Cross, S. E.; Jin, Y. S.; Rao, J.; Gimzewski, J. K. *Nat. Nanotechnol.* **2007**, *2* (12), 780.

41. Touhami, A.; Nysten, B.; Dufrene, Y. F. *Langmuir* **2003**, *19* (11), 4539.

42. Levy, R.; Maaloum, M. Nanotechnology **2002**, *13* (1), PII S0957- 4484 (02) 27598.

43. Hutter, J. L.; Bechhoefer, J. *Rev. Sci. Instrum.* **1993**, *64* (11), 3342.

44. A-Hassan, E.; Heinz, W. F.; Antonik, M. D.; D'Costa, N. P.; Nageswaran, S.; Schoenenberger, C. A.; Hoh, J. H. *Biophys. J.* **1998**, *74* (3), 1564.

45. (35) Burks, G. A.; Velegol, S. B.; Paramonova, E.; Lindenmuth, B. E.; Feick, J. D.; Logan, B. E. *Langmuir* **2003**, *19* (6), 2366.

46. Brochu, H.; Vermette, P. *Langmuir* **2008**, *24* (5), 2009.

47. Dulinska, I.; Targosz, M.; Strojny, W.; Lekka, M.; Czuba, P.; Balwierz, W.; Szymonski, M. *J. Biochem. Biophys. Methods* **2006**, *66* (1-3), 1.

48. Dimitriadis, E. K.; Horkay, F.; Maresca, J.; Kachar, B.; Chadwick, R. S. *Biophys. J.* **2002**, *82* (5), 2798.
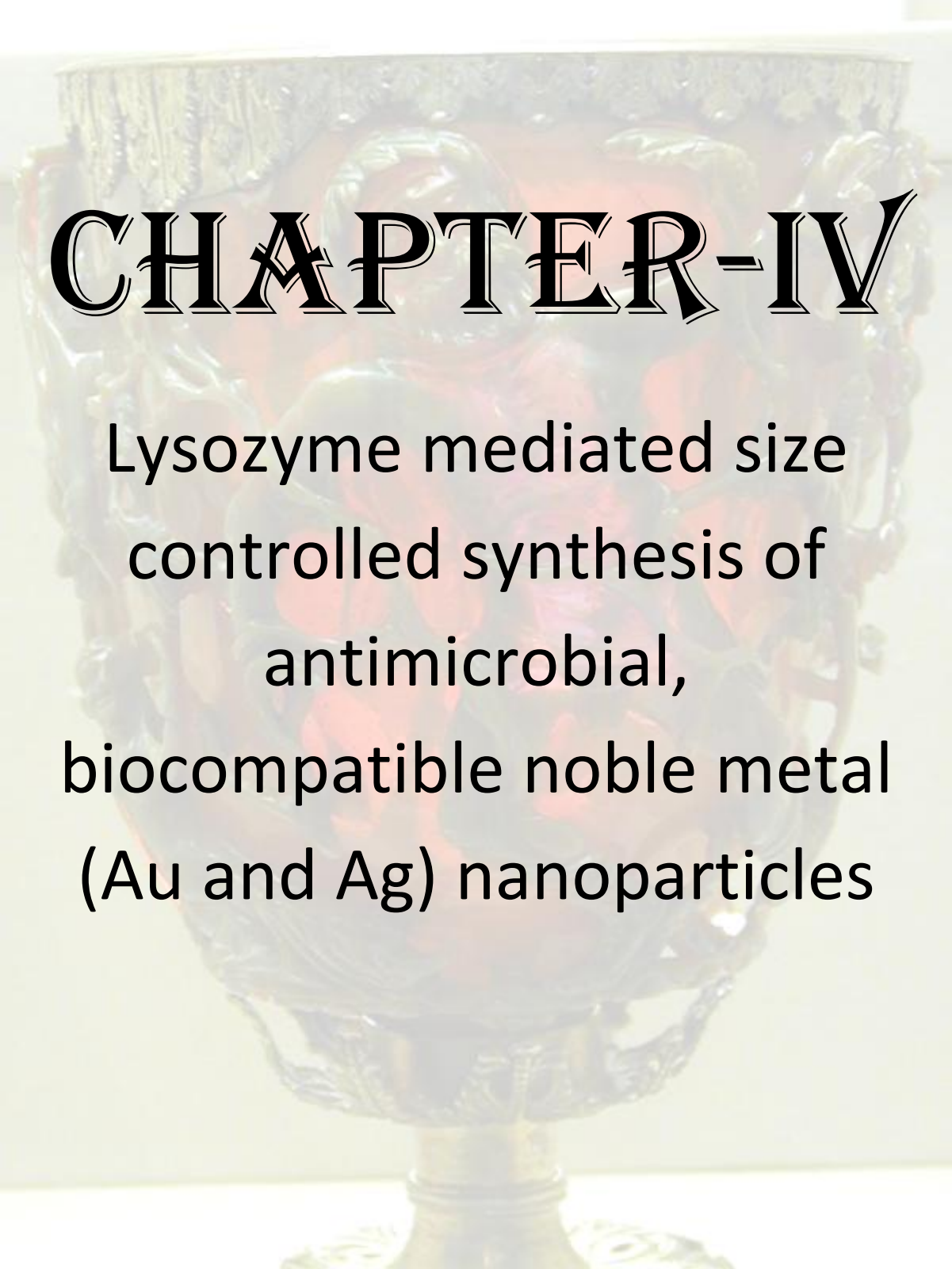
CHAPTER-IV

Lysozyme mediated size controlled synthesis of antimicrobial, biocompatible noble metal (Au and Ag) nanoparticles

Lysozyme mediated size controlled synthesis of antimicrobial, biocompatible noble metal (Au and Ag) nanoparticles
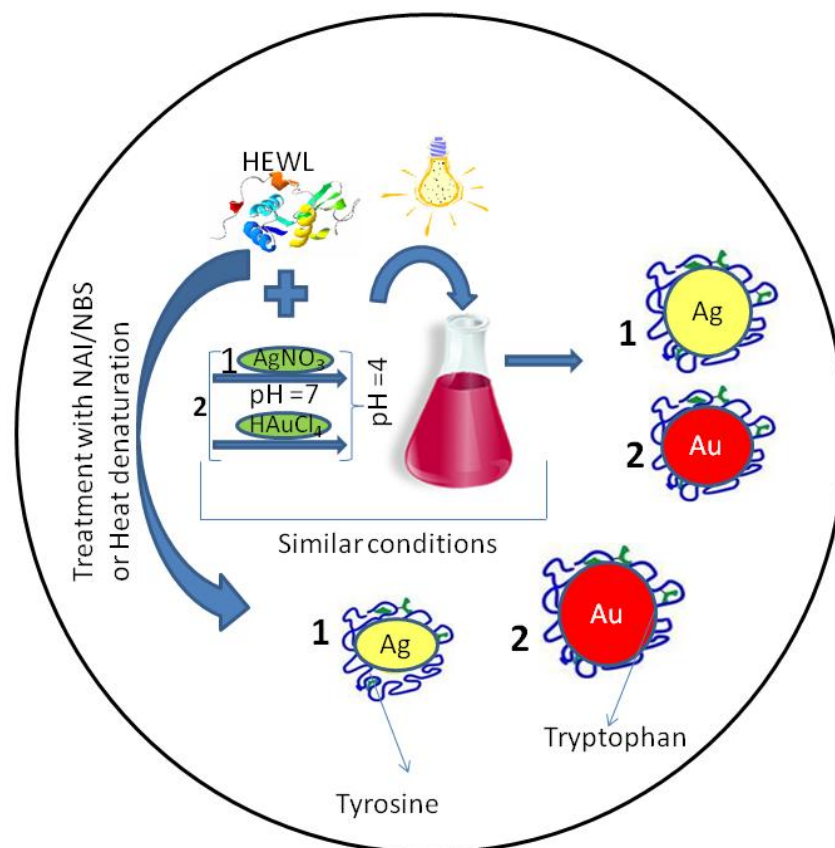
The study of interaction between inorganic materials and biomolecules such as proteins, enzymes, DNA etc. as well as living cells e.g. microbial or mammalian cells is an important concern for various applications ranging from bio-sensors, drug delivery, biofunctionalization for bone-implants up to green chemistry involving biomimetic synthesis of inorganic materials. Inspired by array of proteins present in nature, we chose lysozyme from hen egg protein as a model system to synthesize nanoparticles of noble metals to understand the mechanism of interaction as well as to use them for potential applications such as potent antibacterial agents. Here in this chapter we have discussed the synthesis mechanism of gold and silver nanocrystals at controlled pH and light conditions without using any known reducing agent. The synthesis of gold nanoparticles is assisted by the presence of low concentration of

Ag^+ ions through the galvanic exchange. As-synthesized lysozyme capped nanoparticles prepared by this method are biocompatible and retain antibacterial property. With increasing interest in the biofunctionalization of noble metal nanoparticles for various applications, it is important to precisely investigate the functional groups responsible for binding and probable structural changes in the biomolecules, as both are key factors affecting the bioactivity of these molecules. However, it is not an easy task to probe these properties; especially for the bigger molecules such as enzymes/proteins. Surface-enhanced Raman spectroscopy (SERS) has been used extensively in the detection of biomolecules and study of their conformation on the noble metal surfaces since its discovery because of its high sensitivity. This technique is capable of detecting changes in the secondary structure and the effects of surrounding environment on the biomolecule in the proximity of nanoscopic rough metal surfaces. In this chapter, we have demonstrated the use of this technique to precisely determine the functional groups responsible in the surface capping of gold and silver nanoparticles synthesized by the hen egg white- lysozyme.

4.1 Introduction

Noble metallic nanoparticles such as gold and silver have potential applications in the fields of physics, chemistry, biology and material science because of their shape and size dependent physical and chemical properties[1]. Several well established methods are known for synthesis of these nanoparticles[2-4] however chemical reduction of the metal salts by $NaBH_4$ or other reducing agents is still the most frequently used method among various synthetic routes. Nowadays people are focusing their efforts on fabrication of bioactive and biocompatible nanoparticles for a variety of applications. DNA[5], peptides[6], and proteins[7] have been conjugated to the protecting agents of nanoparticles through an intermediate or linking agents. Direct conjugation of biocompatible agents (lipid bilayers[8] and dendrimers[9]) and biomolecules (amino acid such as lysine[10,11]) to nanoparticles has been achieved in aqueous medium. Sun[12] and Yacaman[13] et al. have employed biomacromolecules e.g globular protein, bovine serum albumin in the preparation of bovine serum albumin (BSA)-conjugated silver sulfide (Ag_2S) and gold nanoparticles. Among all the biomolecules it is always fascinating to tag various kinds of enzymes (or biocatalyst). There are several reports in literature where different research groups have

immobilized different enzymes on the surface of nanoparticles (e.g. magnetic or metal nanoparticles) keeping their activity intact. Most of the enzymes e.g. glucose oxidase[14], cholesterol oxidase[15], Streptokinase[16,17] etc. are immobilized covalently on nanoparticles surface for use in clinical applications and sensors[15]. Major challenge with this techniques is to retain the enzyme activity after immobilization. Sometimes enhancement in enzyme activity is also seen as in case of DhlA-(FeAP)$_3$-(His)$_6$ and DhlA-(SiAP)$_2$-(His)$_6$ possibly due to positive conformational changes caused by different ways of folding of tagged DhlA. In addition changes in protein shape could also lead to change in rate of substrate diffusion and its binding characteristics subsequently the altered enzymatic activity[18].

Recently gold nanoparticles synthesized with R-amylase where enzyme acts both as reducing as well as capping agent, has been reported to retain the enzyme activity after the preparation [19]. We chose lysozyme from hen egg protein as a model system to synthesize nanoparticles of noble metals, gold and silver, to understand the mechanism of interaction as well as to assess their use in applications such as potent antibacterial and anti HIV[20] agents. Lysozyme is a well studied enzyme consisting of 129 amino acid residues with a molecular weight of 14.4 kDa. It catalyzes hydrolysis of β-1,4-linkages between N-acetylmuramic acid and N-acetyl-D-glucosamine residues in peptidoglycan present in the cell wall of gram positive bacteria and the linkage between N-acetyl-D-glucosamine residues in chitodextrins. It is a very well characterized biomolecule containing Tyrosine as one of the aromatic amino acids having phenoxy group which is considered to be responsible for interaction with the metal ions[21].

Currently some groups have claimed achieving control over shape and size of metal nanoparticle as well as their higher order assemblies by using small peptides[21,22]. Sandhage *et al*., have used selected peptides to synthesize metal oxide (TiO$_2$, SiO$_2$) at room temperature[23,24]. There are reports in literature where lysozyme has been used to synthesize antibacterial silica or titania nanoparticles of amorphous nature with diameters of hundreds of nanometers by a rapid, room-temperature precipitation method, with encapsulation of lysozyme within the nanoparticles[25]. Recently Eby et al. have synthesized antibacterial silver nanoparticles in organic solution using lysozyme as the reducing as well as capping agent and transferred it to aqueous solution maintaining its biological activity[26]. The use of proteins and peptides to

direct the in vitro syntheses of inorganic materials is attractive for a number of reasons; a few of these are highlighted here and detailed throughout this chapter. The first and the foremost potential benefit is the production of material under reaction conditions that are much milder than those used in traditional materials-processing techniques. Selected peptides and proteins can facilitate the syntheses of inorganic materials at or around the room temperature, in aqueous solutions, and at or near neutral pH. The reduction of energy input and avoidance of organic solvents to produce nanomaterials in the presence of proteins and peptides make bioenabled synthesis inherently "green" process. The second major advantage in exploiting biomolecules for materials synthesis is the exquisite control that proteins and peptides can impose on the size, shape, chemistry, and crystal structure of the inorganic product. This is important because these characteristics often dictate or determine the properties of the synthesized material and thirdly, the peptides and proteins offer the potential to produce materials with multiple functions and high specificity. For example, proteins and peptides may direct the formation of enzymatically active composites or generate materials that specifically recognize substrates and self-assemble[27].

When it comes to interaction of lysozyme with various nanomaterials, one of the previous work utilized α-Fe$_2$O$_3$ particles to adsorb lysozyme and α-lactalbumin on its surface using electrostatic interactions[28]. Based on the ion exchange interactions, lysozyme was tagged onto Fe$_3$O$_4$ nanoparticles coated with polyacrylic acid (PAA).[29] It should be noted here that in all these previous studies, people used Fourier transformed infrared spectroscopy (FTIR) to investigate the interaction of lysozyme molecules with the inorganic particles. However, using FTIR spectroscopy alone, these previous studies could not clearly indicate the binding mechanism (the functional group involved in the binding process) which is extremely important as the final application of biofunctionalized nanoparticles purely rests on this issue. Yang *et al.* studied lysozyme monolayer protected gold nanoparticles through FTIR but it was not conclusive as they were again unable to show the functional group responsible for surface capping[30]. As we know that FTIR signals can be masked by the O-H stretching and to avoid the O-H stretching, the sample is normally dried, but due to this drying process, we lose the desired information about the biomolecules as

drying up the molecules could also change the structure of the protein molecules on the surface.

In this chapter lysozyme mediated synthesis of antibacterial, biocompatible silver and gold nanoparticles were discussed where lysozyme acts as reducing as well as surface capping agent. Out of these materials, the synthesis of gold nanoparticles is assisted by the presence of meagre concentration of Ag^+ ions through the galvanic exchange. In this chapter, we have shown the use of surface-enhanced Raman scattering technique (SERS) to investigate the binding mechanism between enzyme and noble metal surfaces. The SERS technique is especially useful in the investigation of biomolecules due to its high sensitivity and fluorescence quenching when adsorbed on gold or silver surface. Moreover, this technique can be used to detect the effect of surrounding environment on the molecule. In case of protein studies, the conventional Raman spectroscopy can detect the presence of disulfide bond and protein conformation, which is quite difficult by any other spectroscopy technique. But Raman spectroscopy cannot predict the information of peptide backbone, disulfide bond geometry, and local environment effect on the side chain of the amino acid residues[31]. The SERS can detect protein sites in direct contact with the charged surface like silver or gold[31]. The presence of strong bands of any group in the spectra gives the information about the preferential interaction of the protein sites with the charged surface. Recently various types of surface enhancement based techniques have been a boon to the molecular detection and have enriched almost all branches of science where the proximity to the rough surfaces of noble metals is used to enhance the signal ranging from magnetooptic Kerr effect in Fe_3O_4 nanoparticles[32] to surface enhanced infrared absorption,[33-35] UV/vis absorption,[36] flurorescence,[37-40] circular-dichroism[41] and Raman spectroscopy[42-45]. Among these techniques, the surface-enhanced Raman spectroscopy (SERS) has been particularly popular recently as people are still discovering better and better enhancement by experimenting with the surface structure and type of metals. Below, we present the lysozyme mediated synthesis of antimicrobial, biocompatible silver and gold nanoparticles and our results on the surface enhanced Raman spectroscopy to study the protein functional moiety of lysozyme responsible to cap and interact with silver and gold nanoparticles surfaces.

4.2 MATERIALS AND METHODS

4.2.1 Materials

Lysozyme was purchased from Sigma-Aldrich Inc. This protein was used as received throughout nanoparticles synthesis procedure. Chloroauric acid and silver nitrate were purchased from Sisco Research Lab (SRL) and Merck, India respectively. For all the syntheses, we used deionized water from Milli-Q water purification system.

4.2.2. Experimental details

4.2.2.1 Nanoparticle synthesis procedure

Lysozyme (1mg/ml) was used to synthesize gold (pH 4.5) and silver (pH 7) nanoparticles. Silver nitrate (3 mM) and chloroauric acid (1 mM) were used as precursors for gold nanoparticles synthesis. Minimum concentration of silver nitrate required for gold nanoparticles synthesis is 0.1 mM. Silver nitrate (1 mM) was used as precursor for silver nanoparticles synthesis.

4.2.2.2 Removal of silver chloride (AgCl) impurity from nanoparticles solution

Lysozyme synthesized nanoparticles solution was treated overnight with 1% ammonium hydroxide followed by dialysis using dialysis membrane with molecular weight cut off, 12.5 kD. Dialysis was carried out for 24 hours against milli Q water at room temperature with three changes every 8 hours.

4.2.2.3 Modifications of lysozyme

4.2.2.3.1 Heat denaturation of lysozyme

Preparation of denatured lysozyme. For the denaturation of lysozyme, 1mg/ml solution was heated at 100 ºC for 10 minutes followed by quench cooling at 4 ºC. The final volume was made up by adding fresh water to maintain the said concentration.

4.2.2.3.2 Chemical modification of tyrosine residues of lysozyme with N-Acetylimidazole (NAI)

Freshly prepared aqueous solution of NAI was used for acetylation of tyrosine residues present in lysozyme. An aliquot from stock solution of NAI was added to

aqueous solution of lysozyme (1mg/ml) to the effective concentration of 10 mM. The reaction was incubated at room temperature for 30 minutes followed by dialysis for 24 hours against milli Q water with three changes every 8 hours to remove excess of NAI. The resulting modified lysozyme was used for synthesis of nanoparticles.

4.2.2.3.3 Chemical modifications of tryptohan residues of lysozyme with N-Bromosuccinimide (NBS)

Aqueous solution of NBS was freshly prepared using recrystallized NBS. Stock solution of NBS was added to aqueous solution of lysozyme (1mg/ml) to the effective concentration of 2 mM at room temperature for 30 minutes followed by dialysis for 24 hours as described above. The resulting modified lysozyme was used for synthesis of nanoparticles.

4.2.3 Cytotoxicity test i.e MTT (3,[4,5-dimethylthiazol-2-yl]-2,5-diphenyltetrazolium bromide) assay

To determine the toxicity of nanoparticles MTT assay was performed following Plumb[46] method with slight modification. In brief, the cells i.e. HEK 293T, HELA and CHO K1 (2000 cells/well in 100 μl of medium, Dulbecco modified eagles medium) were seeded in a 96 well plate and allowed to adhere for 24 h at 37 ℃ in a 5% CO_2 95% air atmosphere. The medium (Annexure-II) was replaced with serum-free medium containing different concentrations of lysozyme capped gold nanoparticles and incubated for 24 h at 37 ℃. The supernatant was removed and 100 μl serum-free medium with 0.5 mg/ml MTT were added to each well and re-incubated for another 3 h at 37 ℃. The MTT solution was carefully discarded and 100 μl of 2% SDS was added to each well and incubated for another 12 h. After 12 h, 10 μl of 5 N HCl was added in each well for solubilization of formazan crystals. After solubilisation the supernatants were carefully collected and centrifuged at 10000 rpm for 1 minute to get rid of nanoparticles and re-dispensed in new 96 well ELISA plates and absorbance was recorded at 570 nm, using a multiwell microplate reader (Spectromax 250 from Molecular Devices). The set of untreated samples (0 mM) was also run in parallel under identical conditions that served as the control.

4.3. Characterization techniques

Ultraviolet-visible absorbance was recorded on a Jasco UV-vis-NIR (Model V570) dual beam spectrophotometer operated at a resolution of 2 nm. Fluorescence spectra were recorded on a CARY Eclipse instrument from Varian with a slit width of 5 nm. Powder XRD patterns were carried out on a PHILIPS X'PERT PRO instrument equipped with X'celerator- a fast solid-state detector on drop coated sample on glass substrate. The sample was scanned using X'celerator with a total number of active channels of 121. Iron-filtered CuKα radiation (λ=1.5406 Å) was used. The XRD patterns were recorded in the 2θ range of 20°- 80°. Dynamic Light Scattering (DLS) measurements were performed on a Brookhaven Instruments Corp. with 90 Plus Particle Size Analyzer software version 3.94. Atomic Force Microscopy (AFM) samples were prepared on fresh and clean silicon wafer. AFM images were obtained using "E" scanner on Nanoscope IV (Veeco). The raw images obtained were offline processed using 5.303r2 software. Determination of nanoparticle shape and size were performed on FEI, Technai F30, electron microscope (TEM) operated at an accelerating voltage of 300 kV. Thermogravimetric analysis (TGA) for lysozyme synthesized metal nanocrystals was performed on Q5000 V2.4 Build 223 instrument by applying scan rate 10 ^{0}C min^{-1} in presence of nitrogen. Fourier Transform Infra red Spectroscopy (FTIR) was carried out on a Perkin–Elmer Spectrum One instrument operated in the diffuse reflectance mode at a resolution of 2 cm^{-1}. X-ray photoelectron spectroscopy (XPS) for nanoparticles were performed on VG MicroTech ESCA 3000 instrument at a pressure <1x10^{-9} Torr with an overall resolution of 1 eV. The spectra was recorded with unmonochromatic Mg K alpha radiation (photon energy = 1253.6 eV) at a pass energy of 50 eV and electron take off angle (angle between electron emission direction and surface plane) of 60°. Circular dichroism (CD) measurements were performed on a spectrophotometer Jasco 715 with a step resolution of 1 nm keeping sensitivity of 100 milli degree. In order to rule out the contribution from free or unbound protein present in each kind of nanoparticle solution, CD spectra were recorded for both lysozyme capped nanoparticle samples as well as unbound protein. In order to calculate the amount of nanoparticles present in different samples AAS (Atomic absorption spectroscopy) measurements were taken on Chemito-Atomic absorption spectrometer 201 with silver hollow cathode lamp. Elemental ananlysis of different metals was done by

elemental analyzer EA1108 (Carlo Erba Instruments). Raman spectroscopy measurements were recorded at room temperature on a HR 800 Raman spectrophotometer (Jobin Yvon, Horiba, France) using monochromatic radiation emitted by a He-Ne laser (633 nm), operating at 20 mW. The experiment was repeated at least three times to verify the consistency of the recorded spectra. The samples for the Raman studies were prepared simply by drop casting the liquid on the glass slide. For the crystalline lysozyme, the crystalline powder was dispersed on the glass slide.

4.4 Results and discussion

4.4.1. Proposed mechanisms for nanoparticle synthesis It

is known that tyrosine plays important role in electron transfer in the photosystem II (PS II) of photosynthesis, where a neutral tyrosyl radical is generated[47]. Sjodin et al proposed a proton coupled electron transfer for pH < 10 (below pK_a of tyrosine ~10) and single electron transfer was proposed for pH > 10 (above pK_a of tyrosine). Since we work around lower pH range, all tyrosine groups in protein will always be in protonated form and similar proton coupled electron transfer (pH < 10) could be responsible for the reduction of silver ions. It is worth mentioning here that there is always a possibility of formation of protein silver ion complex while reduction reaction takes place. This is because silver ions are known to form complex with amino acid like Asp, Glu, His, Cys, Lys and Met[48,49] having different side chain groups. The driving force for silver nanocrystal formation in protein solution comes from simple redox reaction where silver ions are reduced by accepting an electron from tyrosine residue, which becomes oxidized in the process[21]. The reaction mixture was kept in the presence of light at temperature of 40 ºC. The pH of the protein solution was adjusted to 4.5 and 7 for gold and silver respectively using 0.1 M NaOH. In order to study the effect of light in synthesis, same reaction was kept in dark keeping other parameters constant. Interestingly no nanoparticles formation was observed in absence of light supporting the above mentioned hypothesis. Comparative ultraviolet-visible absorption spectra of gold and silver nanoparticles collected after 96 hours of reaction followed by dialysis suggested formation of lysozyme capped noble metal nanoparticles as seen in figure 4.1(A). Appearance of

peaks at ~ 530 nm and 454 nm in the ultraviolet-visible spectroscopy indicates the formation for gold and silver nanocrystals respectively.
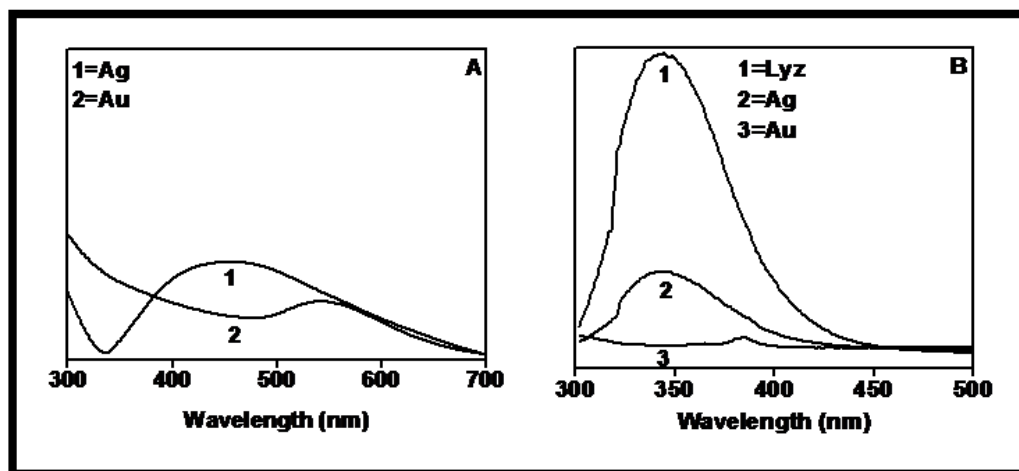

Figure 4.1: Ultraviolet-visible absorption spectra (A) for lysozyme capped gold and silver nanoparticles recorded after 96 hours of reaction. Appearance of peaks at ca. 530 nm and 454 nm indicates the formation of gold and silver nanoparticles. Photoluminescence emission spectra (B) for lysozyme capped gold and silver nanoparticles excited at 280 nm. Decrease in emission intensity indicates that aromatic amino acids like Tyrosine and tryptophan present in lysozyme got oxidized during synthesis of gold and silver nanoparticles. In case of silver nanoparticles slightly higher emission intensity indicates that only fraction of aromatic amino acid (tyrosine and tryptophan) residues got oxidized while some are still free

4.4.2. Identification of the key residues of lysozyme responsible for nanoparticle synthesis

Now the question arises how lysozyme is catalyzing the formation of nanoparticles in the aqueous medium. To explore the possibility of involvement of aromatic amino acids (Tyrosine and Tryptophan) in catalyzing the formation of nanoparticles, we compared the fluorescence signals from lysozyme and lysozyme capped nanoparticles by exciting these solutions at 280 nm. The aromatic amino acids such as tyrosine and tryptophan which act as internal fluorophores in the lysozyme molecule give characteristic emission spectra centered around 345 nm which is in the range of the reported value of 340 nm[50]. In figure 4.1(B), we have compared the emission spectra of the lysozyme alone with lysozyme capped silver and gold nanoparticles after 24 hours of reaction. In case of silver nanoparticles, fluorescence emission spectra peak is obtained in between 340-348 nm. When Ag^+ are incubated

with lysozyme at pH **7** and a temperature of 40 ºC, the Ag^+ ions could be present in the following forms: (1) free cationic form in solution and/or (2) strongly bound to lysozyme molecules probably by binding through COO^- groups (Asp and Glu) of lysozyme and/or (3) by complex formation with the nucleophilic groups in the residues, such as imidazole group (His), -SH (Cys), $-SCH_3$ (Met), and $-NH_2$ (Lys)[21]. The reducibility of the Ag-complex to form silver nanocrystals decreases with the increasing binding strength of the complex. The standard electrode potential of Ag^+/Ag redox is 0.8 V^{21}. However, this value is significantly different when the Ag ions are complexed. Generally, complexation lowers the redox potential and hence the reducibility of Ag ions [21]. From the graph presented in figure 4.1(B) it is clear that as the reaction progresses more and more Ag^+ bind to the phenoxy moiety of tyrosine probably resulting in change in the conformation of protein in such a way that tryptophan becomes closer to the residues like aspartate and glutamate hence the decreased emission intensity was observed[21] compared to free lysozyme at 345 nm. However in case of gold no significant emission spectra were observed in that region (345 nm). This could be due to differential affinities of silver and gold ions which can interact with side chain groups, such as amine, carboxyl and hydroxyl moieties of tryptophan and tyrosine residues or it could be due to the change in the conformation of protein in such a way that tryptophan becomes closer to the residues like aspartate and glutamate[51]. Now question arises, what is the effect of pH on structure of lysozyme used for different nanoparticles synthesis (i.e. gold and silver) since pH is known to be a crucial parameter influencing protein conformation. To answer the above question we compared the fluorescence signal of lysozyme with lysozyme capped different nanoparticles (i.e. gold and silver) under identical conditions (figure 4.2). These results clearly show that there is no drastic change in the structure of lysozyme itself at pH 4.5 and 7 used for synthesis of gold and silver nanoparticles. Further to confirm our results we used tyrosine and tryptophan solutions individually in same molar concentration as that of lysozyme (1mg/ml or 70 μM), mixed with gold and silver precursor salts to synthesize nanoparticles keeping other parameters constant (pH, temperature, concentration). Interestingly nanoparticle formation was not observed supporting the hypothesis for formation of silver ion complex with different aminoacids present in lysozyme subsequently lowering the reducibility of silver ions. We have shown temporal evolution of peaks
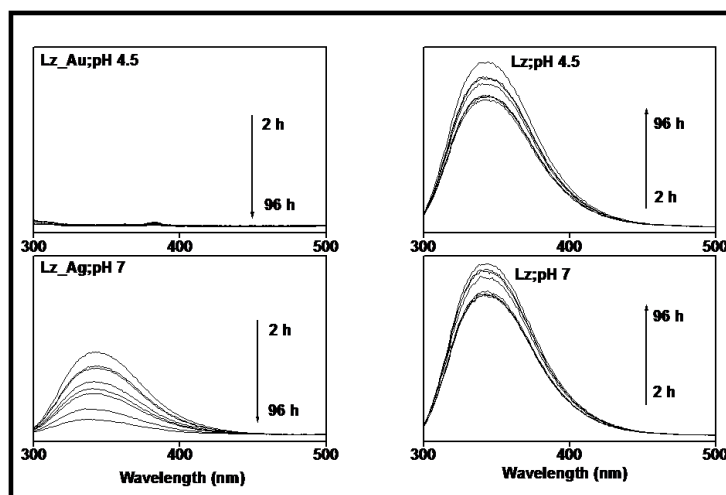
Figure 4.2. Fluorescence emission spectra for lysozyme (Lz) capped gold, silver nanoparticles (left column) and their corresponding controls (right column) taken at 2,3,6,24,36,48,72 and 96 h of reaction. Decrease in emission intensity in (left column) indicates the oxidation of tyrosine and tryptophan residues present in lysozyme as reaction progresses.

during gold and silver nanoparticles synthesis when native and heat denatured lysozyme were used (figure 4.3).
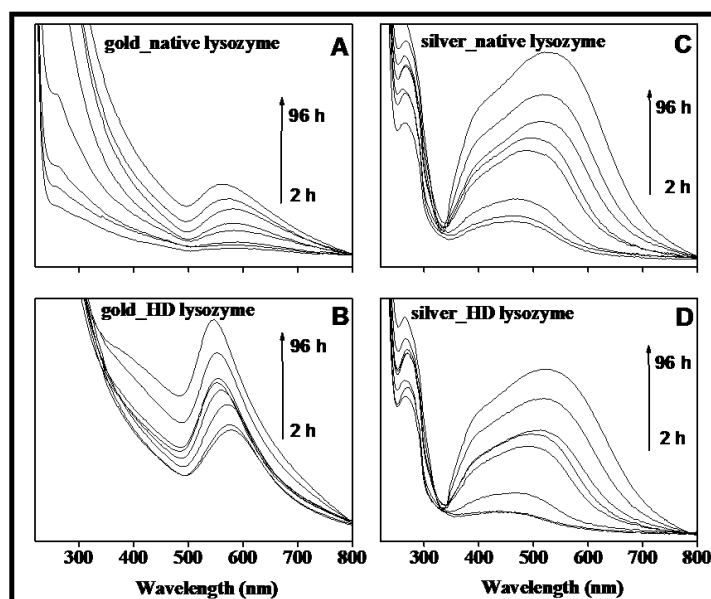

Figure 4.3: Ultraviolet-visible absorption spectra for gold (A,B) and silver nanoparticles recorded at 2,3,6,24,36,48,72 and 96 h of reaction(C,D) when native (A,C) and heat denatured, HD (B,D) lysozyme was used for synthesis indicating the temporal evolution of peaks as reaction progresses. Slightly blue shift in case of (B) indicates the enhanced binding of lysozyme with gold nanoparticles surface via its side groups like amino group of tryptophan residues as reaction progresses. Enhanced binding of lysozyme occurs because of the breaking of dimeric and trimeric forms of lysozyme into monomeric forms due to heating. Drastic increase in intensity of peaks at 280 nm in case of (A) indicates the opening of polypeptide (lysozyme) chain containing aromatic amino acids

It is clear from figure 4.3 that there is no change in the absorption spectra whether native (C) or heat denatured (D) lysozyme was used for silver nanoparticles synthesis. This is probably because there is no change in the availability of tyrosine which is responsible for the reduction of silver ions. Further it is important to note that there is evolution of three peaks at ca. 524 nm, 422 nm and 347 nm corresponding to in plane dipole, out of plane dipole and quadruple plasmon resonance indicating the formation of plate like structure[52]. Interestingly after treatment with 1% ammonium hydroxide all peaks vanished except the peak at ca. 450 nm indicating the disappearance of plate like structure (Figure 4.1A). This is because insoluble silver chloride becomes solublised after treatment with ammonium hydroxide and get removed after dialysis (figure 4.4). On the other hand in case of gold nanoparticles there is distinct change in the absorption spectra when native and denatured lysozyme was used for synthesis. This is because in case of heat denatured lysozyme amine groups of tryptophan become free to bind with gold nanoparticles, as a result of which there is slight blue shift in spectra as reaction progresses and the particles formed have more or less uniform size (sharp peak) compared to native lysozyme where particles are polydispersed (broad peak). It is interesting to note that
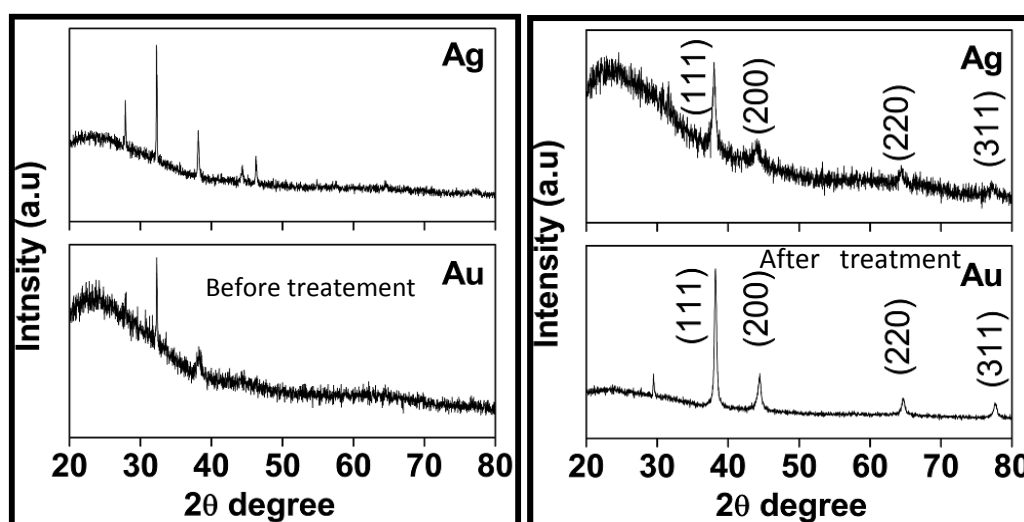

Figure 4.4: XRD pattern of as-prepared sample (untreated) showing the presence of silver chloride in both samples

as time progresses there is remarkable increase in the intensity of peak at 280 nm probably because aromatic amino acids e.g. tyrosine and tryptophan become more exposed to the outer environment as reaction progresses (figure 4.3A,B).

4.4.3. Size controlled synthesis of nanoparticles by chemical modification of lysozyme with NAI and NBS In

order to confirm our results we specifically blocked tyrosine and tryptophan residues in native and heat denatured lysozyme by treating lysozyme with N-acetylimidazole (NAI) and N-bromosuccinimide (NBS) respectively, dialysed for 24 hours and then used for synthesizing nanoparticles of gold and silver. Ultra-violet visible spectroscopy data clearly suggests that in absence of free tyrosine there is no silver nanoparticle formation (figure 4.5A), but at the same time in case of heat denatured
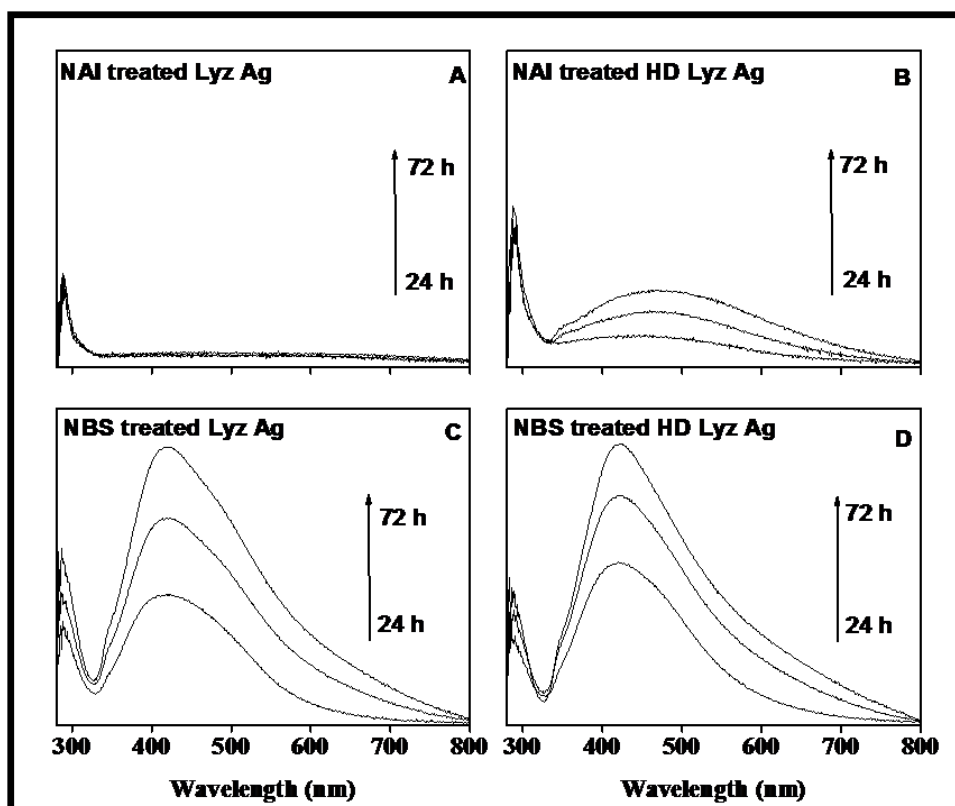

Figure 4.5: Ultraviolet-visible absorption spectra of silver nanoparticles synthesized by chemically modified native and heat denatured (HD) lysozyme (N-acetylimidazole i.e NAI and N-bromosuccinimide i.e NBS treated) collected in real time manner, clearly indicating the role of tyrosine in synthesis

lysozyme treated with NAI , there is occurrence of broad absorbance peak at ~ 450 nm (figure 4.5B) suggesting the formation of silver nanoparticles. This is probably due to presence of some free tyrosine residue that is left unblocked due to folding/unfolding of lysozyme during heat treatment. These findings were further confirmed by appearance of clear absorbance peak at 420 nm when NBS treated

native and heat denatured lysozyme was used for synthesis of silver nanoparticles (figure 4.5C,D). It is interesting to note here that when native and heat denatured lysozyme was used for synthesis of silver nanoparticles there is occurrence of three peaks at ca.524 nm, 422 nm and 347 nm indicative of formation of plate like structure which is absent in case of chemically modified native and heat denatured lysozyme (NAI and NBS treated). Therefore we can say that by controlling the availability of tyrosine and tryptophan present in lysozyme in a reaction mixture we can precisely control the size of silver nanoparticles produced. Similarly role of
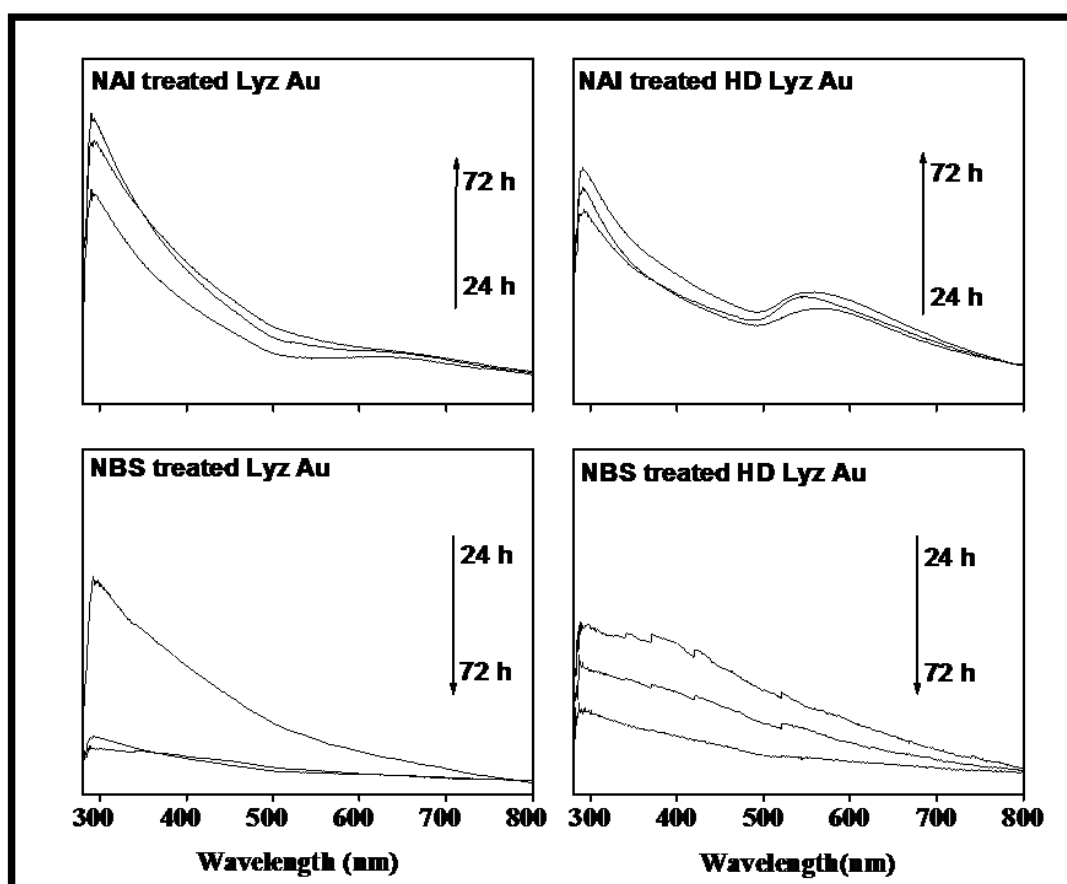

Figure 4.6: Ultraviolet-visible absorption spectra of gold nanoparticles synthesized by chemically modified lysozyme (N-acetylimidazole i.e NAI and N-bromosuccinimide i.e NBS treated) collected in real time manner, clearly indicating the role of tryptophan in synthesis

tryptophan was clearly demonstrated in gold nanoparticles synthesis where there is occurrence of broad absorption peak between 550-600 nm in case of NAI treated heat denatured lysozyme (figure 4.6B) but completely absent in case of NBS treated both native and heat denatured lysozyme which is in accordance with our previous results (figure 4.6C,D). These results clearly suggest that besides tyrosine,

tryptophan is very important residue for gold nanoparticle synthesis. Interestingly we observed quenching of fluorescence signal at 340 nm with respect to time in case of silver nanoparticle synthesized using NAI treated native and heat denatured lysozyme. This quenching (figure 4.7) is not because of the interaction of silver ions with tryptophan but probably because of the change in the structure of lysozyme in such a way that tryptophan becomes closer to amino acids residues like aspartate or
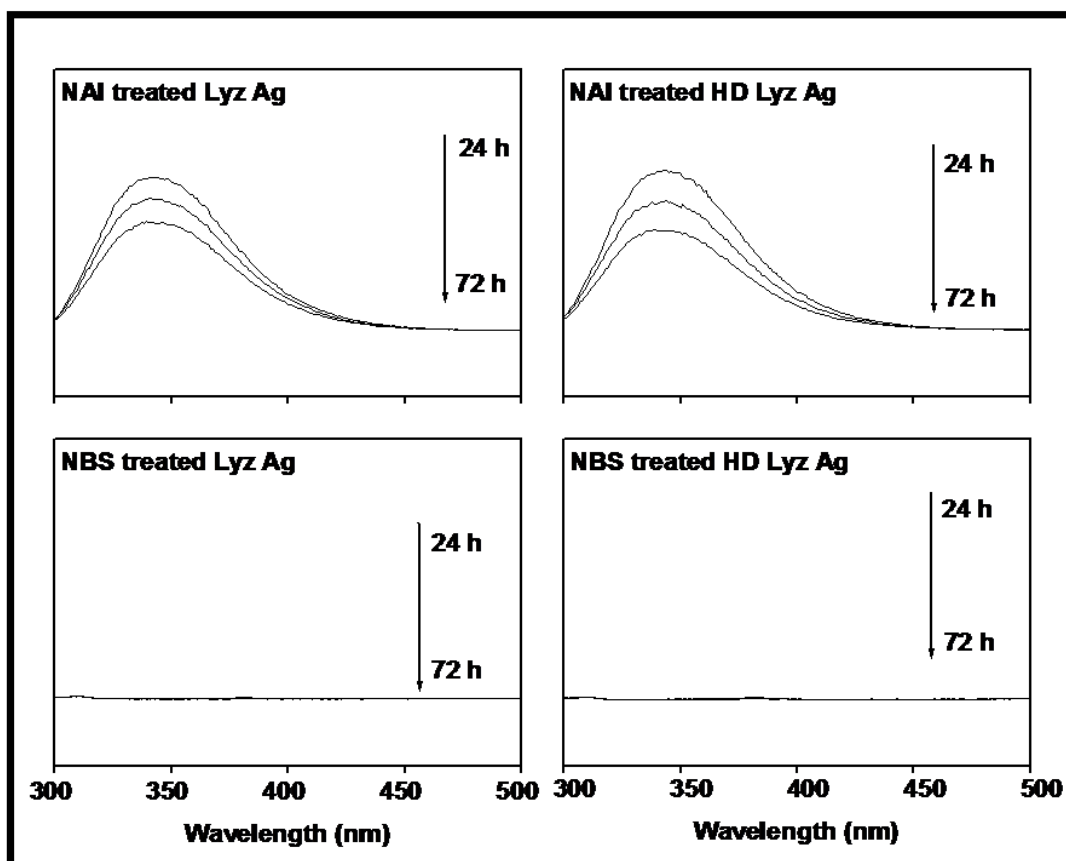

Figure 4.7: Photoluminiscence emission spectra of silver nanoparticles synthesized by chemically modified lysozyme (N-acetylimidazole i.e NAI and N-bromosuccinimide i.e NBS treated) collected in real time manner, clearly indicating the involvement of tyrosine in synthesis and hence quenching of emission at 345 nm is observed as reaction progresses

glutamate. These amino acids are known to quench the fluorescence emission signal arising from tryptophan present in protein when excited at 280 nm. Similarly there is complete absence of fluorescence signal when NBS treated native and heat denatured lysozyme was used for silver nanoparticles synthesis not because of the interaction of silver ions with tryptophan but because of the complete blocking of all tryptophan residues present in lysozyme with NBS as depicted in graph (figure 4.7). To rule out

the possibilty of quenching because of interaction of silver ions with tryptophan residues present in lysozyme we have shown the fluorescence emission spectra of NAI and NBS treated native and heat denatured lysozyme excited at 280 nm, (figure 4.8) where complete quenching of fluorescence signal at 340 nm can be clearly seen in case of NBS treated native and heat denatured lysozyme compared to NAI treated lysozyme.
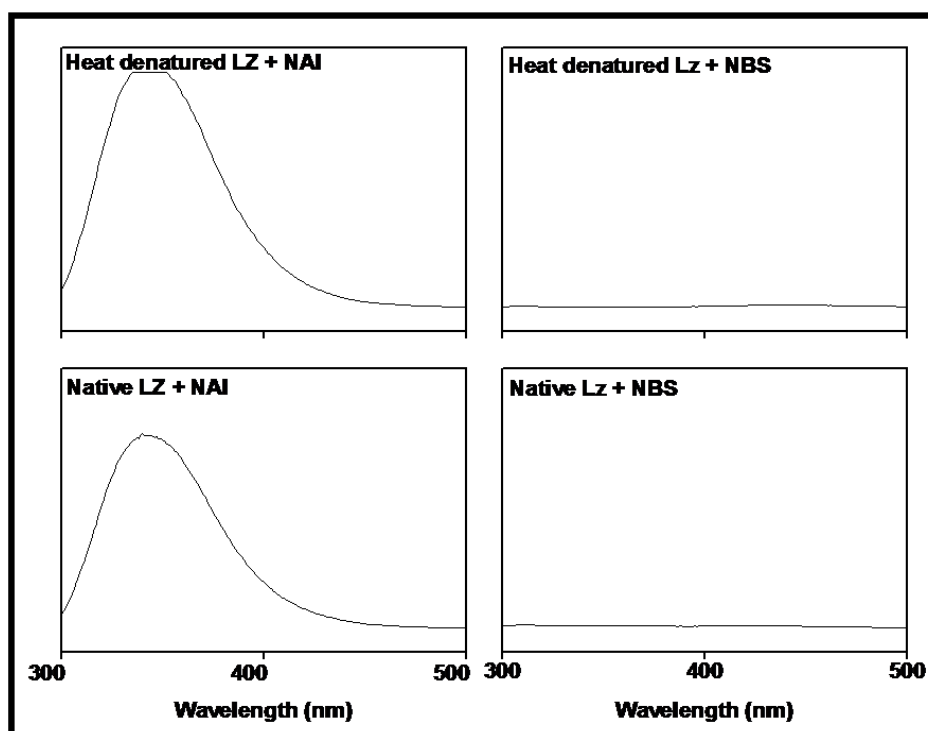

Figure 4.8: Photoluminiscence emission spectra of chemically modified lysozyme excited at 280 nm (N-acetylimidazole i.e NAI and N-bromosuccinimide i.e NBS treated) indicating the presence of emission signal at 345 nm due to aromatic amino acids (tryptophan)

4.4.4. Determining changes in the secondary/tertiary structure of lysozyme present on nanoparticles surface

To probe whether there is any change in the secondary or tertiary structure of protein during tyrosine or tryptophan modifications we have carried out circular dichroism (CD) studies on NAI and NBS treated native and heat denatured lysozyme and compared them with native lysozyme CD spectra as shown in figure 4.9(A). Identical CD spectra in case of NAI treated native and heat denatured lysozyme clearly indicates that there is no major change in the structure of lysozyme due to these treatments. On the other hand NBS treated native and heat denatured lysozyme

shows major changes in the secondary structure (alpha helix) of lysozyme as shown in figure 4.9(A). This is because of the presence of larger number of tryptophan
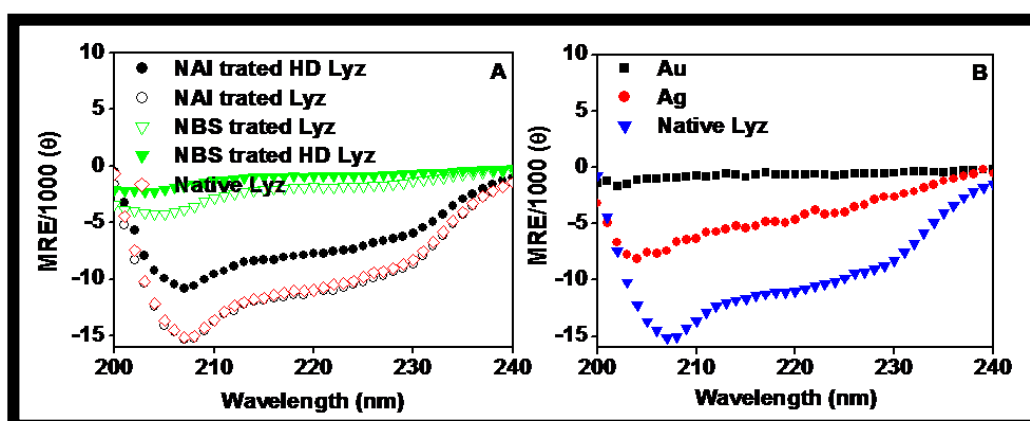

Figure 4.9: Comparative Circular Dichroism (CD) spectra (A) of native lysozyme (Lyz) along with other chemically modified lysozyme, clearly indicating no change in its secondary structure after treatment with chemical modifiers like N-acetylimidazole i.e NAI but remarkable change is observed after treatment with N-bromosuccinimide i.e NBS. Graph showing considerable change in the secondary structure of lysozyme (B) in case of lysozyme capped gold and silver nanoparticles

residues (six) in lysozyme. Similarly we have carried out circular dichroism studies with lysozyme synthesized gold and silver nanoparticles to probe the conformational changes on lysozyme after their synthesis, shown in figure 4.9(B). These curves clearly show that there is drastic change in the alpha helices of lysozyme present on gold and silver naoparticles surface compared to native lysozyme.

4.4.5. Determination of crystallinity, shape and size distribution of nanoparticles

Further to confirm the crystallinity of these metal naoparticles XRD studies were carried out. Presence of peaks at $2\theta=38.23$, 44.32 64.51 and 77.63 corresponding to the (111),(200) (220) and (311) planes confirms the crystalline nature of silver nanoparticles (PCPDF # 40783). Similarly occurrence of peaks at $2\theta = 38.2$, 44.3, 64.5 and 77.6 corresponding to (111), (200), (220) and (311) planes confirms the crystalline nature of gold nanoparticles (PCPDF # 40784). Formation of silver chloride was seen in all the samples (figure-4.4) These chloride ions come from lysozyme itself, as it was prepared by crystallizing in buffer containing NaCl. Silver

chloride was removed from each colloidal solution by treating it with 1% ammonium hydroxide followed by dialysis for 24 hour. The XRD pattern shown in figure 4.10 was recorded after dialysis.
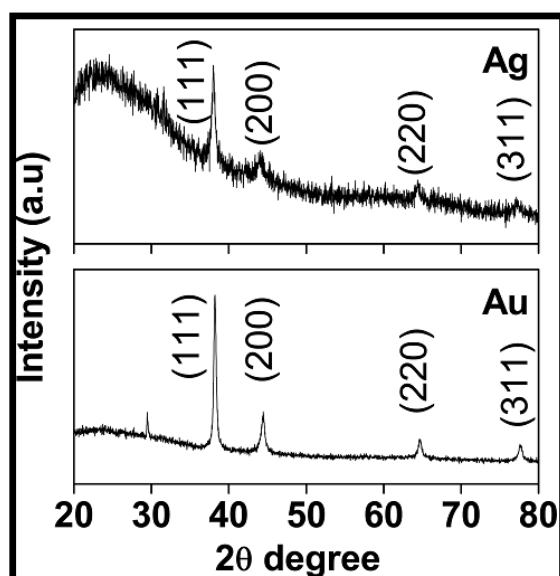

Figure 4.10: X-ray diffraction (XRD) pattern for nanocrystalline gold and silver nanoparticles synthesized by lysozyme recorded after treatment with 1% ammonium hydroxide followed by dialysis for 24 hours

Formation of gold nanoparticles was assisted by silver through galvanization/transmetallation reaction[53,54]. In order to determine the size of the nanoparticle DLS experiments were carried out with dialysed samples. It is interesting to note that in all these samples atleast two different particle size populations were seen (Figure 4.11). This is probably because there are two different
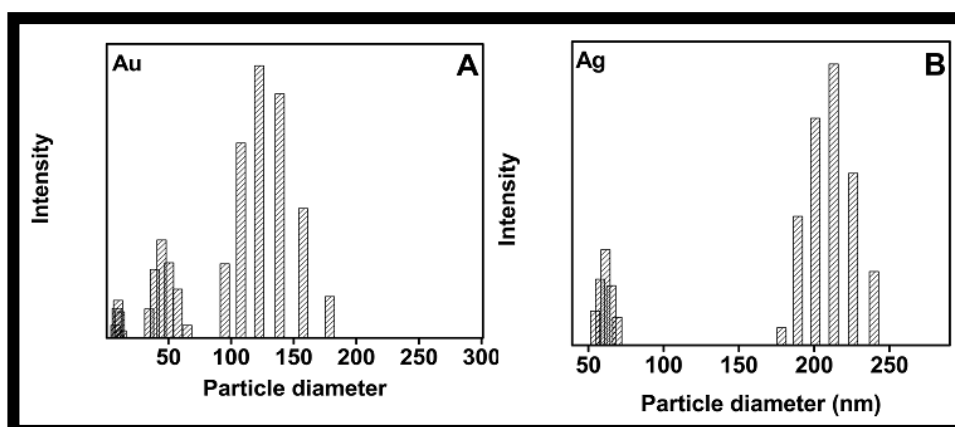

Figure 4.11: Average particle size (hydrodynamic radii) calculated by Dynamic light scattering (DLS) measurements for gold (A) and silver (B) nanoparticles. Presence of multimodal size distribution indicates the presence of protein aggregates of different sizes in every sample

mechanisms (whose reaction rates could be similar/different) operating simultaneously for nanoparticle formation. For example in case of silver both tyrosine and silver chloride are responsible for silver nanoparticle formation which is similar to formation of metallic silver during the conventional photographic process, where silver halide is used as a semiconductor to capture incident light[55]. Other possibility for bimodal/trimodal distribution is due to the presence of unbound protein which may exist in different forms e.g dimers, trimers etc. These findings were further supported by SDS PAGE (15%) results. Samples were prepared by collecting the supernatant obtained by centrifuging the nanoparticle solution at 10000 rpm for 20 minutes at 4°C. Occurrence of bands at 49.1 kDa indicates that commercially available lysozyme itself contain proteins in some aggregate form (figure 4.12). Similarly for gold nanoparticles both small and large populations were seen. The particle size calculated by DLS is much larger than the particle size
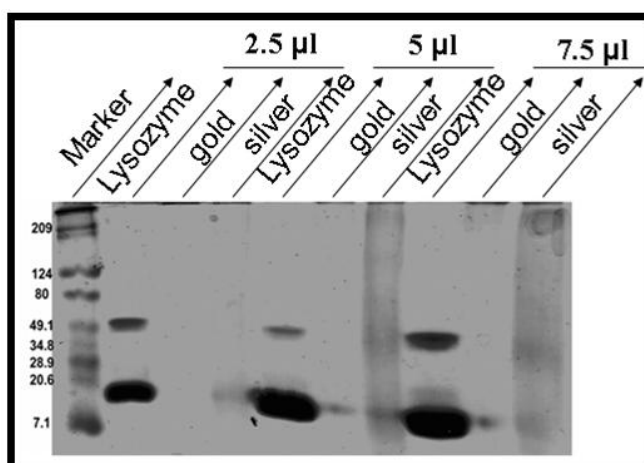

Figure 4.12: SDS PAGE (15%) showing the presence of lysozyme on the surface of nanoparticles. Samples are prepared by collecting the supernatant obtained by centrifugation (12000 rpm for 20 minutes at 4 °C). As the loading volume increases the respective bands also gets intensified. Presence of smear in case of silver nanoparticles indicates the denaturation of proteins. Occurrence of bands at 49.1 kDa indicates that commercially available lysozyme itself contain proteins in trimer form supporting DLS measurements results

estimated by Transmission electron microscopy which is obvious because DLS gives us the hydrodynamic radius which is average of all the particles including protein aggregates (lysozyme dimers, trimers etc.). These data were further supported by

Atomic force microscopy images where both small and large particles were clearly seen (figure 4.13).
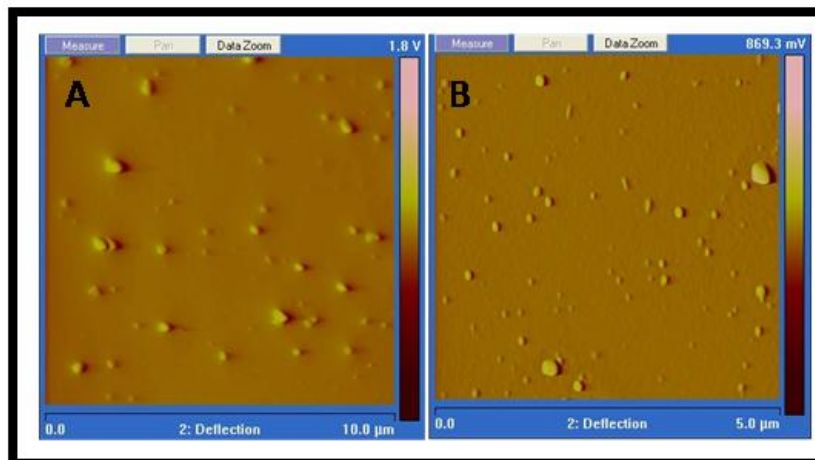
Figure 4.13: AFM images for gold (A) and silver (B) nanoparticles. Presence of particles of different sizes supports the DLS data which shows multimodal size distribution

Further to determine the size and shape of nanoparticles transmission electron microscopy was done for each sample (Figure 4.14). In case of gold, the
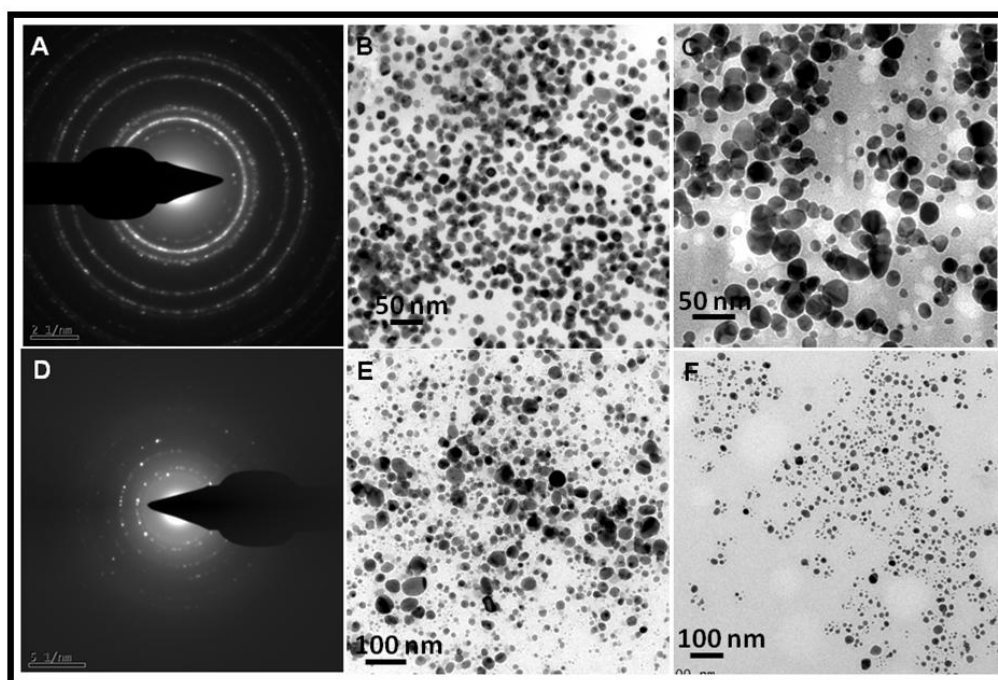
Figure 4.14: Selected area electron diffraction i.e., SAED (A,D) and their corresponding Transmission electron microscopy (TEM) images (B,E) of nanoparticles synthesized by lysozyme. TEM micrographs (C,F) of nanoparticles synthesized by modified (Heat and NBS treated for gold and silver nanoparticles respectively) lysozyme. Upper and lower panel represents gold and silver nanoparticles

nanoparticles were evenly distributed and were of uniform size as shown in figure 4.14 B. The average particle size calculated for gold nanoparticles synthesized by native lysozyme was 18 nm (Figure 4.14B) whereas those synthesized by heat denatured lysozyme was larger (Figure 4.14C). These samples were prepared by collecting the pellet after centrifuging different colloidal solution at 10000 rpm for 10 minutes at 4 °C. This is the probable reason why only similar sized nanoparticles are seen in gold whereas in case of silver even the smaller sized particles are 25-30 nm which get settled at this speed (Figure 4.14E). Hence both small and large sized particles were seen in their corresponding transmission electron microscopy images but when the same nanoparticles were synthesized by NBS treated lysozyme average particle size reduces to 15nm (Figure 4.14F).

4.4.6. Identification of charge, stability and loading amount of lysozyme present on nanoparticles surface

Further to determine the charge on the nanoparticle Zeta potential measurements were done for these samples which can be correlated with their stability. The measured values are -30 mV and -34 mV for gold and silver nanoparticles. The presence of negative charge in both samples in spite of different pH optima indicates that this negative charge is coming from the lysozyme itself where chloride ions are present. This was further confirmed by running 1% agarose gel where all the these samples migrate towards positive electrode (figure 4.15).
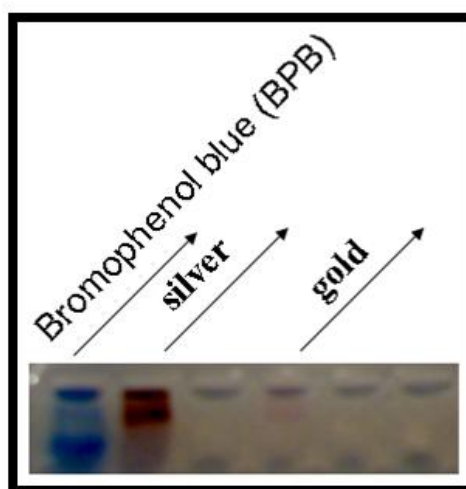

Figure 4.15: 1 % Agarose gel image showing movement of nanoparticles in the direction of bromophenol blue indicating the presence of negative charge on its surface supporting zeta potential measurements results

In order to quantitatively determine the amount of protein bound to nanoparticles, protein estimation was done using Lowry method using BSA as protein standard. The samples were prepared by centrifugation of the nanoparticles solution at 10000 rpm for 10 minutes and resuspending the pellet in equal volume of water. Results indicated approximately 15% − 20% protein loading, which is less than the amount calculated by thermogravimetric analysis (TGA). For these measurements samples were lyophilized to powder dry form. Higher values of weight loss (Figure 4.16) were recorded for gold (40%) and silver (88%) because the samples for TGA measurements had unbound protein also.
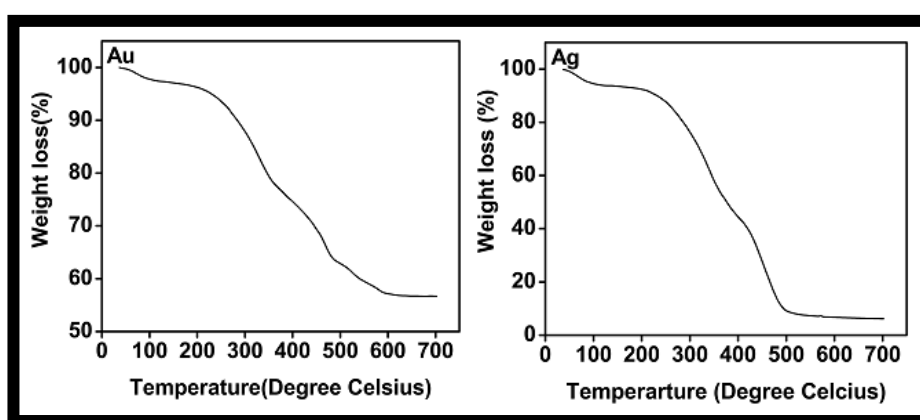
Figure 4.16:. Graph showing percentage weight loss for lysozyme capped gold (Au) and silver (Ag) nanoparticles measured by thermogravimetric analysis (TGA)

In this chapter we have shown that lysozyme is acting both as capping and reducing agent in all these synthesis procedures. To confirm this hypothesis FTIR were performed. FTIR samples for these studies were prepared by removing the unbound proteins by centrifuging at 10000 rpm for 10 minutes at 4 °C and drop casting metal nanoparticles (pellet) on silicon wafer. Occurrence of bands at 1682 cm^{-1}, 1552 cm^{-1} and 3306 cm^{-1} (Figure 4.17) corresponding to Amide-I, Amide-II and NH stretch in all samples indicate the presence of proteins on the surface of all these metal nanoparticles[14]. There is a slight shift in these bands compared to bare lysozyme due to binding of protein to nanoparticles surface.
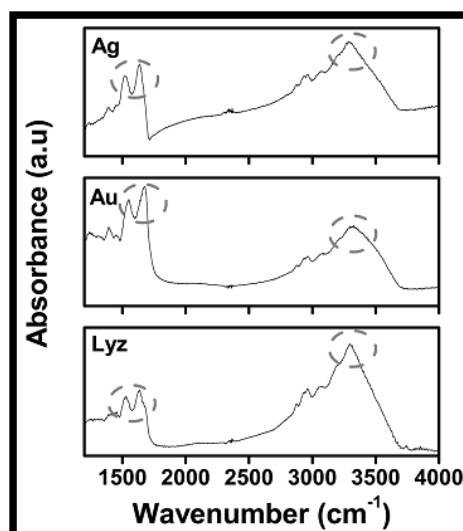
Figure 4.17: Fourier transform infra red (FTIR) spectra showing the presence of intact Amide-I, Amide-II and NH stretch in case of lysozyme (Lyz) capped gold (Au) and silver (Ag) nanoparticles

4.4.7. Oxidation state determination of lysozyme capped nanoparticles

Further to determine the purity of these nanoparticles X-ray photoelectron spectroscopy (XPS) was done. As-obtained XPS core level spectra were background corrected using the Shirley algorithm and chemically distinct species were resolved using a nonlinear least squares fitting procedure. The core level binding energies (B.E.) were aligned with the carbon binding energy of 285 eV. In figure 4.18 we have shown the background corrected XPS spectra for gold (A) and silver (B)
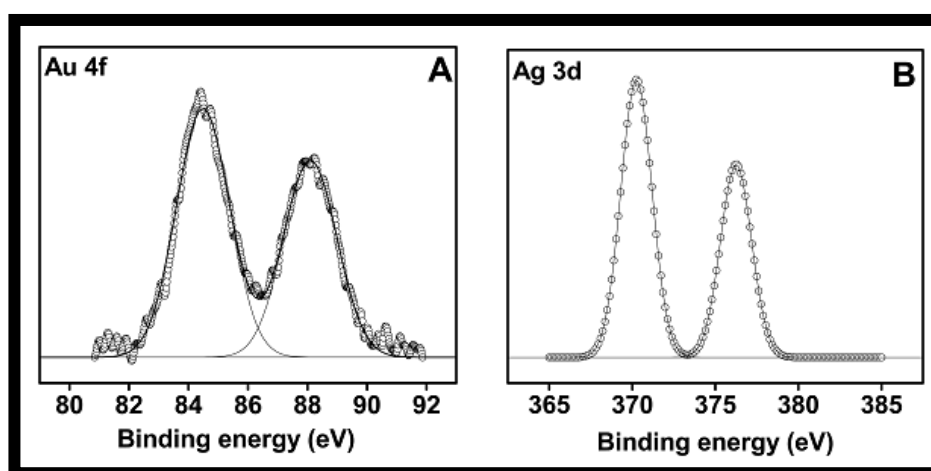
Figure 4.18: X-ray Photoelectron Spectroscopy curves for lysozyme capped gold (A) and silver (B) nanoparticles

nanoparticles. Figure 4.18A shows the splitting of Au 4f spectrum into two spin–orbit components. The Au $4f_{7/2}$ and $4f_{5/2}$ peaks occuring at a binding energy (BE) of 84.4 and 88.1 eV, respectively, and are assigned to metallic gold[56]. Figure 4.18B shows the splitting of Ag 3d spectrum, into two spin–orbit components. The Ag $3d_{5/2}$ and $3d_{3/2}$ peaks occurred at a B.E of 370.1 and 376.1 eV, respectively, corresponding to metallic silver[56]. It is important to note that there is shift of 2 eV in case of silver nanoparticles because of the presence of electronegative atom chlorine attached to lysozyme. Interestingly there is no shift in the case of gold probably because of more (comparatively) binding of protein with silver nanoparticles as previously seen in TGA curves (Figure 4.16).

4.4.8. Determination of biofunctionality and biocompatibility of lysozyme capped nanoparticles

Finally to confirm wheather bioactivity of lysozyme is maintained or not after synthesis of metal nanoparticles, antibacterial assay was performed against gram positive bacterium, *B. subtilis.* It is important to note here that we have used the 24 hour dialysed nanoparticle
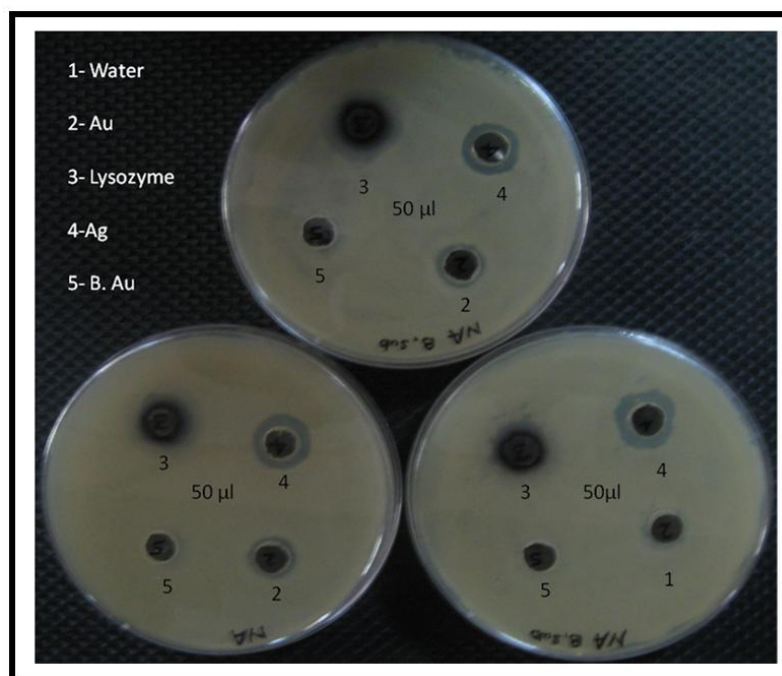

Figure 4.19: Antibacterial activity of lysozyme functionalized gold and silver nanoparticles performed against *Bacillus subtillis.* For comparison, we have used borohydrate reduced gold and lysozyme solution as control. Presence of zone of inhibition in case of nanoparticles solution indicates that lysozyme is still active after getting immobilised on to the surface of nanoparticles

solution for each well and compared it with lysozyme (well-1) and borohydride reduced gold (well-5) solution (Figure 4.19). Presence of clearance zone in case of gold and silver indicate that lysozyme bioactivity was retained after nanoparticle synthesis. Now the questions arises wheather these nanoparticles are biocompatible/cytocompatible, also can they be used for future biological applications like drug delivery or not? To check this possibility MTT assay was performed with gold nanoparticles on three different cell lines (CHO K1, HELA and HEK 293T). MTT results showed that lysozyme capped gold nanoparticles are non toxic to these cells till 40 mM compared to control (Figure 4.20A). Only in case of
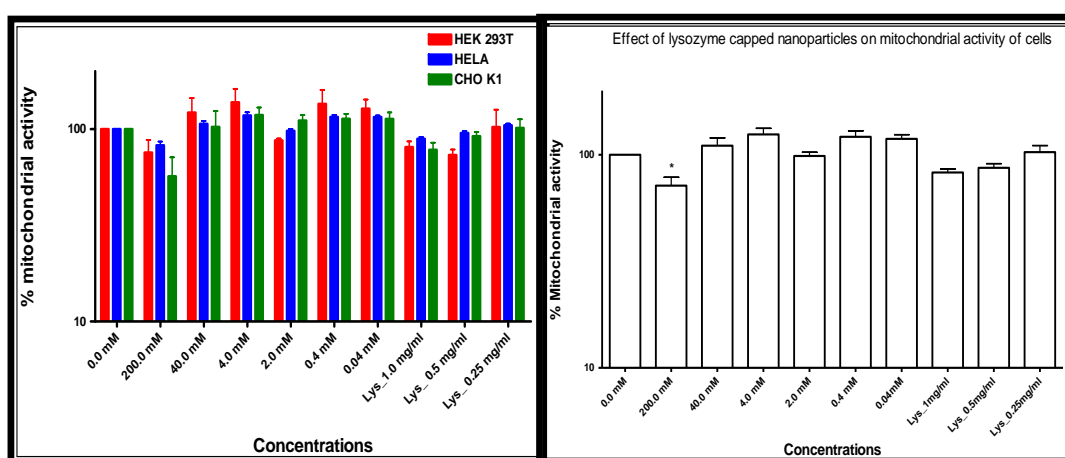
Figure 4.20: MTT graph showing the effect of lysozyme capped gold nanoparticles on viability of different cells at various concentrations (A). Lower panel (B) shows the overall effect of gold nanoparticles on viability of cells at different concentrations calculated by one way analysis of variance (ANOVA) and Dunnett test using GraphPad Prism Software (Ver 4.0). (*) for p < 0.05

higher concentration of nanoparticles i.e 200 mM (Figure 4.20B) statistical significant decrease in percentage viability of cells was observed. These results clearly suggests that gold nanoparticles prepared by this method are biocompatible and can be used for other biological applications. The cell viability in percentage could be calculated as:

$$(\text{A570 of treated samples}/\text{A570 of untreated samples}) \times 100$$

where, A570 is the absorbance at 570 nm[57]. The data presented are the mean $\pm$ standard deviation (SD) from three independent experiments.

4.4.9. Surface enhanced Raman spectroscopic studies for lysozyme capped gold and silver nanoparticles

As discussed earlier, FTIR was not the best technique to study the biomoleules in their natural state as the O-H stretching could mask the desired modes and to avoid the O-H stretching, the sample for FTIR measurements was dried out of the solution which could change the conformation of the protein molecule on the surface giving inconclusive results. Therefore, we studied the samples using Raman spectroscopy. For this purpose, it was important for us to characterize first, the lysozyme itself in detail in various conditions to understand and compare the changes in conformation of lysozyme before and after surface capping and then analyse of the presence of lysozyme on gold and silver nanoparticles. Initially we compared the Raman spectra for the as-received solid lysozyme crystals with the lysozyme in the native and denatured state in the solution phase without further purification. For native lysozyme in aqueous medium, the commercially available lysozyme was dissolved in deionized water. We observed that after dissolving the lysozyme crystals in the water, the solution pH was about 4.5. Denatured lysozyme solution was prepared by heating the lysozyme solution to 100 ^{o}C for 5 min followed by quench-cooling it at 4 ^{o}C for 10 minutes. In figure 4.21 we compared the Raman spectra for all the three samples (as-received solid lysozyme crystals, lysozyme in the native and denatured state in the solution phase) and details on the Raman peaks were tabulated in table 4.1. In all the three spectra a common peak at around 429 cm^{-1} was observed which was assigned to the vibration of the amino acid residues of phenylalanine or tyrosine. Further, we assigned the band situated around 760 cm^{-1} to symmetric benzene/pyrrole in-phase breathing mode in tryptophan and symmetric ring breathing mode in tyrosine and phenylalanine. The band at 1010 cm^{-1} was assigned to the symmetric benzene/pyrrole out-of-phase breathing in tryptophan and the band at 1550 cm^{-1} was due to the symmetric phenyl ring mode in Tryptophan[58-60], which appeared in the solid crystals (marked by star), but disappeared or was less intense in the case of native and denatured lysozyme solution (panel a and b). It may be due to the fact that the phenyl ring or the pyrrole ring of the amino acids which were responsible for this vibration were quenched in the aqueous environment due to the formation of hydrogen bonds with the water molecules. It was reported that in Raman spectra, the S-S vibration band were observed around 509 cm^{-1}.[61]
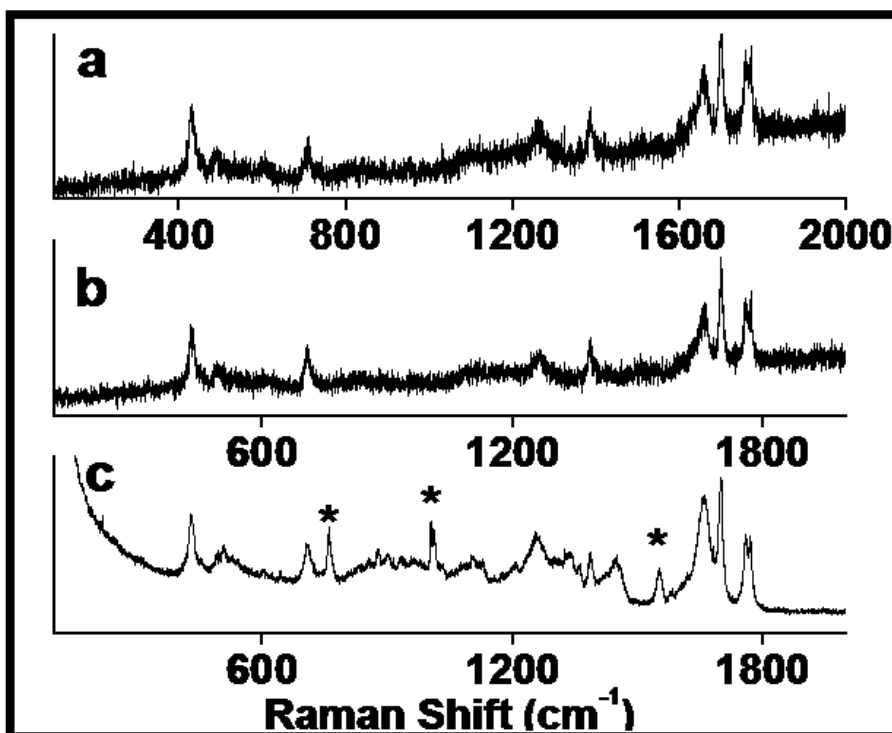
Figure 4.21: Comparison of Raman spectra of (a) denatured lysozyme in solution (b) native lysozyme in solution and (c) lysozyme solid crystals recorded at room temperature

Solid Lysozyme	Native Lysozyme	Denatured Lysozyme	Tentative Assignment
429	429	429	Phe or Tyr
509	509	509	S-S
760	760	760	Trp or His
936	936	936	C_α-C-N (Peptide backbone)
1010	1010	1010	
1235-1310	1235-1310	1235-1310	Trp
1550	1550	1550	Amide III
1640-1680	1640-1680	1640-1680	Trp, His Amide I

Table 4.1: Raman shifts for lysozyme in various forms

Here in our study, the S-S vibration band was present in all the three cases, showing that even the denaturization did not affect the disulfide bond. In literature, there was

a contradiction on this issue. Brunner and Sussner *et al.* reported that there is disappearance of S-S bond vibration upon heat denaturation at 76 $^{\circ}$C[62]. However, Chen et al. in similar experiment clarified that there was no change in S-S bond vibration upon denaturation. It is well understood that there was no change in S-S bond upon reversible thermal denaturation of lysozyme and other protein molecules seen in our results. It was reported in literature that amide I bands corresponding to alpha helix, beta sheet and random coil appeared in Raman spectra between 1640 cm^{-1} to 1680 cm^{-1}, whereas in our studies they appeared as a broad peak in this range which confirmed the intactness of amide I bond in lysozyme in all three conditions[63]. The amide III band due to alpha helix, beta sheet and random coil appeared in the region of 1235 to 1310 cm^{-1}.[63] However, in present case, it also appeared as a broad peak. The band around 936 cm^{-1} which appeared in all three cases was assigned to the skeleton stretching of peptide, that confirmed the presence of the alpha helix conformation of the lysozyme molecule in all three conditions. After characterizing in detail the basic Raman signatures of lysozyme in various cases, next we investigated our lysozyme synthesized gold and silver nanoparticles. For this purpose, the as-synthesized nanoparticles were purified first by dialysis using a 12.4 kDa (Mol.wt.cut off) cellulose dialysis membrane purchased from Sigma Aldrich (D9652-100FT) to remove any unreacted gold or silver salt. For the Raman spectroscopy, dialyzed nanoparticles were drop casted on glass slides and dried at room temperature. In figure 4.22 we have compared the
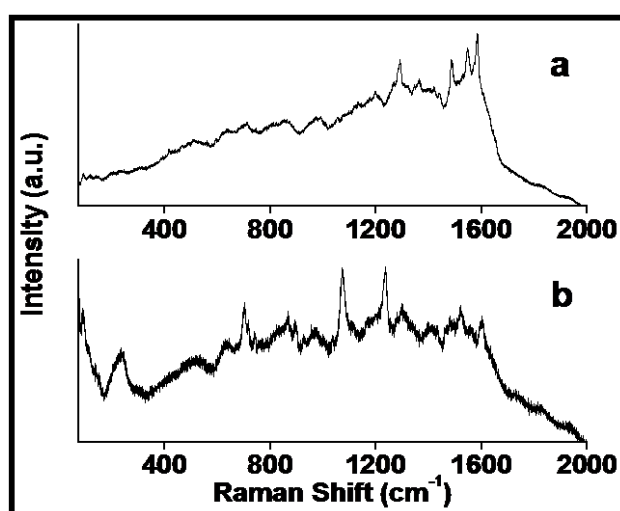

Figure 4.22: Raman spectra of (a) lysozyme capped gold nanoparticles and (b) lysozyme capped silver nanoparticles recorded at room temperature

Raman spectra for both Au and Ag nanoparticles and the Raman shifts were tabulated in table 4.2. By comparing the Raman spectra for lysozyme itself in various forms and lysozyme synthesized Ag/Au nanoparticles (figures 4.21 and 4.22), it was clear that there was an enhancement (due to the proximity of the lysozyme molecules with metallic surfaces) in the intensity of some peaks with small shift as seen in figure 4.22. In the case of lysozyme capped silver nanoparticles, the presence of peak around 236 cm^{-1} indicated the binding of lysozyme molecules with the surface of Ag nanoparticles through moiety containing N-atom[64].

Lysozyme capped silver nanoparticles		Lysozyme capped gold nanoparticles	
Raman Shift (cm^{-1})	Tentative assignment	Raman Shift (cm^{-1})	Tentative Assignment
206	Ag-N	509 (w)	S-S
509 (w)	S-S	1289	Amide III
704	Trp, Tyr and Phe	1484	Phe, Tyr, Trp
866		1545	Trp or His
1072	Tyr	1583	Tyr
1235	C-N		
1519 and 1598	Amide III		
	Phe, His, Trp, Phe or Tyr		

Table 4.2: Raman shifts for lysozyme capped silver and gold nanoparticles

The absence of sharp band around 509 cm^{-1} in both curves in figure 4.22 which was assigned to the disulfide bond (Table 4.1) suggested that it was not interacting with the Ag and Au nanoparticles during capping. The peak around 1640-1680 cm^{-1} which was assigned to amide I band of alpha helix, beta sheet and random coil of lysozyme molecule were also absent in lysozyme capped silver and gold nanoparticles spectra, probably due to the fact that these functional groups were not involved in interaction with silver and gold nanoparticles surface. In the case of lysozyme capped silver

nanoparticles, a sharp intense peak at 704 cm^{-1} was observed which was assigned to symmetric benzene/pyrrole in-phase breathing in tryptophan and symmetric ring breathing in tyrosine and phenylalanine which suggested that in our samples, the benzene and pyrrole ring might be either standing up or tilting at an angle with respect to the Ag nanoparticles surface. It was also observed that Raman shift was moved to higher wave numbers, clearly indicating that there was some interaction between the Ag nanoparticles surface and these amino acid residues. Further appearance of sharp intense peak at 866 cm^{-1} which was assigned to the vibration of the tyrosine residue, confirmed the interaction of tyrosine with the Ag nanoparticles surface. In this case also there was a slight shift in the peak position which might be due the interaction of the amino acid residue with the Ag nanoparticles surface. Other sharp and intense peaks at 1519 and 1598 cm^{-1} were assigned to the vibration of phenylalanine, histidine, tryptophan and phenylalanine or tyrosine residues, further suggesting the involvement of these amino acid residues with the Ag nanoparticles surface during capping of the lysozyme molecule. Amide I and III which are the backbone of the protein molecule could be studied by Raman spectra. Amide III had a large contribution from the C-N-H in plane bending and C-N stretching mode. In case of Raman spectra of lysozyme capped silver nanoparticles, sharp and intense peaks were obtained at 1072 and 1235 cm^{-1} which were assigned to the C-N stretching and amide III respectively. The observation of these sharp and intense peaks clearly indicated that there was significant interaction of the amide III of the lysozyme molecule with the silver nanoparticles. Other peaks for the amino acid residues are also seen in the spectra but they were very weak in intensity and might not contribute in interacting with metallic surfaces. Here, we do not rule out the possibility of binding of silver nanoparticles with the carboxyl groups as it is reported in literature that –COOH group along with –NH$_2$ groups might be involved in the binding[65,66] of fatty acid with silver surfaces.

In case of lysozyme capped gold nanoparticles, a sharp and intense peak was observed at 1583 cm^{-1} which was assigned to the tyrosine residue of the lysozyme molecules. The presence of this peak showed the interaction of the tyrosine moiety of the lysozyme molecule with the gold nanoparticles during capping of the nanoparticles. Other two sharp and intense peaks were observed in the spectra at 1545 and 1484 cm^{-1}, which were assigned to symmetric phenyl ring mode in tryptophan or histidine and vibration of the phenylalanine, histidine, and tryptophan.

Intensity of these peaks showed that the amino acid residues phenylalanine, tyrosine, tryptophan and histidine might be playing a major role in capping of the lysozyme molecule on nanoparticles surface. Other bands for the amino acid residues were also observed in the spectra but they were less intense. A sharp and intense peak was observed at 1289 cm^{-1} which was assigned to the amide III band. The presence of this intense band in the spectra suggested the involvement of the amino group of the protein molecule with the nanoparticles surface. In both the cases we observed a broad hump around 509 cm^{-1} which indicated the intactness of the disulfide bond. However, as both the native and denatured lysozyme showed similar type of spectra, it was very difficult to conclude whether the lysozyme on Au and Ag was in native or denatured form.

5.0. Conclusion

A simple facile method has been developed for synthesis of metal nanoparticles (gold and silver) utilizing the reduction abilities of amino acids present in lysozyme. Our experimental results prove that hydroxyl groups in tyrosine residues and the imino groups in tryptophan residues were found to be responsible for silver and gold nanoparticles formation respectively. Formation of gold nanoparticles was assisted by silver through galvanization/transmetallation reaction. Further by controlling the availability of tyrosine and tryptophan in lysozyme by suitable chemical treatment we can precisely control the size of nanoparticles. It is interesting to note that gold nanoparticles prepared by this method are biocompatible and retains antibacterial property. These nanoparticles can be used for future applications like drug delivery, bioimaging etc by functionalizing it with ligand/molecule of our choice using different functional groups present on the proteins.

5.1 References

1. Burda, C.; Chen, X. B.; Narayanan, R.; El-Sayed, M. A. *Chem. Rev.* **2005,** *105* (4), 1025.

2. Shipway, A. N.; Katz, E.; Willner, I. *Chemphyschem.* **2000,** *1* (1), 18.

3. Roucoux, A.; Schulz, J.; Patin, H. *Chem. Rev.* **2002,** *102* (10), 3757.

4. Daniel, M. C.; Astruc, D. *Chem. Rev.* **2004,** *104* (1), 293.

5. Mirkin, C. A. *Inorg. Chem.* **2000,** 39 (11), 2258.

6. Whaley, S. R.; English, D. S.; Hu, E. L.; Barbara, P. F.; Belcher, A. M. *Nature.* **2000**, *405*, 665.

7. Mamedova, N. N.; Kotov, N. A.; Rogach, A. L.; Studer, J. *Nano Lett.* **2001,** *1 (6)*, 281.

8. Zhang, L. X.; Sun, X. P.; Song, Y. H.; Jiang, X.; Dong, S. J.; Wang, E. A. *Langmuir.* **2006,** *22* (6), 2838.

9. Haba, Y.; Kojima, C.; Harada, A.; Ura, T.; Horinaka, H.; Kono, K. *Langmuir.* **2007,** *23* (10), 5243.

10. Zhong, Z. Y.; Luo, J. Z.; Ang, T. P.; Highfield, J.; Lin, J. Y.; Gedanken, A. *J. Phy. Chem. B.* **2004,** *108 (47)*, 18119.

11. Selvakannan, P. R.; Mandal, S.; Phadtare, S.; Pasricha, R.; Sastry, M. *Langmuir.* **2003,** *19* (8), 3545.

12. Meziani, M. J.; Sun, Y. P. *J. Am. Chem. Soc.* **2003,** *125 (26)*, 8015.

13. Burt, J. L.; Gutierrez-Wing, C.; Miki-Yoshida, M.; Jose-Yacaman, M. *Langmuir.* **2004,** *20 (26)*, 11778.

14. Rossi, L. M.; Quach, A. D.; Rosenzweig, Z. *Anal.Bioanal.Chem.* **2004,** *380 (4)*, 606.

15. Kouassi, G. K; Irudayaraj, J; McCarty, G. *J. Nanobiotechnol.* **2005**, *3 (1)*, 1.

16. Koneracka, M.; Kopcansky, P.; Timko, M.; Ramchand, C. N. *J. mol. cat B: enz.* **2002,** *18*, 13.

17. Fernandes, E. G. R.; De Queiroz, A. A. A.; Abraham, G. A.; San Roman, J. *J. Mater. Sc-Mater. in Med.* **2006,** *17 (2)*, 105.

18. Gray, J. J. *Curr. Opin. Struc. Biol.* **2004,** *14 (1)*, 110.

19. Rangnekar, A.; Sarma, T. K.; Singh, A. K.; Deka, J.; Ramesh, A.; Chattopadhyay, A. *Langmuir.* **2007,** *23 (10)*, 5700.

20. Lee-Huang, S.; Huang, P. L.; Sun, Y. T.; Kung, H. F.; Blithe, D. L.; Chen, H. C. *Proc. Natl. Acad. Sci. USA.* **1999,** *96 (6)*, 2678.

21. Xie, J. P.; Lee, J. Y.; Wang, D. I. C.; Ting, Y. P. *Acs Nano.* **2007,** *1 (5)*, 429.

22. Slocik, J. M.; Govorov, A. O.; Naik, R. R. *Supramol. Chem.* **2006,** *18 (5)*, 415.

23. Dickerson, M. B.; Jones, S. E.; Cai, Y.; Ahmad, G.; Naik, R. R.; Kroger, N.; Sandhage, K. H. *Chem. Mater* **2008,** *20 (4)*, 1578.

24. Sowards, L. A.; Whitlock, P. W.; Brott, L. L.; Naik, R. R.; Stone, M. O. *Abstr. Am. Chem. Soc.* **2001,** *221*, 232.

25. Luckarift, H. R.; Dickerson, M. B.; Sandhage, K. H.; Spain, J. C. *Small.* **2006,** *2 (5)*, 640.

26. Eby, D. M.; Schaeublin, N. M.; Farrington, K. E.; Hussain, S. M.; Johnson, G. R. *Acs Nano.* **2009,** *3 (4)*, 984.

27. Dickerson, M. B.; Sandhage, K. H.; Naik, R. R. *Chem. Rev.* **2008,** *108,* 4935.

28. Haynes, C. A.; Norde, W. *J. Coll. and Interf. Sc.* **1995**, *169*, 313.

29. Liao, M. H.; Chen, D. H. *Biotechnol. Letts.* **2002**, *24*, 1913.

30. Yang, T.; Li, Z.; Wang, L.; Guo, C. L.; Sun, Y. J. *Langmuir* **2007**, *23*, 10533.

31. Koglin, E.; Squaris, J. M. *Topics in Curr. Chem.* **1986**, *134*, 39.

32. Shemer, G.; Markovich, G. *J. Phy. Chem. B.* **2002**, *106*, 9195.

33. Knoll, B.; Keilmann, F. *Nature.* **1999**, *399*, 134.

34. Wang, H.; Kundu, J.; Halas, N. J. *Angew. Chem.-International Edition.* **2007**, *46*, 9040.

35. Kosower, E. M.; Markovich, G.; Raichlin, Y.; Borz, G.; Katzir, A. *J. Phy. Chem. B.* **2004**, *108*, 12633.

36. Elghanian, R.; Storhoff, J. J.; Mucic, R. C.; Letsinger, R. L.; Mirkin, C. A. *Science.* **1997**, *277*, 1078.

37. Chu, L. Q.; Forch, R.; Knoll, W. *Angew. Chem.-International Edition.* **2007**, *46*, 4944.

38. Aslan, K.; Lakowicz, J. R.; Geddes, C. D. *Anal. and Bioanal. Chem.* **2005**, *382*, 926.

39. Antunes, P. A.; Constantino, C. J. L.; Aroca, R. F.; Duff, J. *Langmuir.* **2001**, *17*, 2958.

40. Kuhn, S.; Hakanson, U.; Rogobete, L.; Sandoghdar, V. *Phy. Rev. Letts.* **2006**, *97.*

41. Lieberman, I.; Shemer, G.; Fried, T.; Kosower, E. M.; Markovich, G. *Angew. Chem.-International Edition.* **2008**, *47*, 4855.

42. Fleischmann, M.; Hendra, P. J.; Mcqillan, A. J. *Chem. Phy. Letts.* **1974**, *26*, 163.

43. Garcia Vidal, F. J.; Pendry, J. B. *Phy. Rev. Letts.* **1996**, *77*, 1163.

44. Michaels, A. M.; Nirmal, M.; Brus, L. E. *J. Am. Chem. Soc.* **1999**, *121*, 9932.

45. Gersten, J. *J. Chem. Phy.* **1980,** *73*, 3023.

46. Plumb, J. A.; Milroy, R.; Kaye, S. B. *Cancer Res.* **1989**, *49*, 4435.

47. Sjodin, M.; Styring, S.; Akermark, B.; Sun, L. C.; Hammarstrom, L. *J. Am. Chem. Soc.* **2000**, *122*, 3932.

48. Merril, C. R.; Harrington, M.; Alley, V. *Electrophoresis.* **1984**, 5, 289–297.

49. Rabilloud, T. *Electrophoresis.* **1990**, *11*, 785.

50. Imoto, T.; Rupley, J. A.; Tanaka, F.; Forster, L. S. *Proc. Nat. Acad. Sci. USA.* **1972,** *69 (5)*, 1151.

51. Chen, Y.; Barkley, M. D. *Biochemistry.* **1998**, *37*, 9976.

52. Jin, R. C.; Cao, Y. C.; Hao, E. C.; Metraux, G. S.; Schatz, G. C.; Mirkin, C. A. *Nature.* **2003**, *425*, 487.

53. Shukla, S.; Pasricha, R.; Sastry, M. *J.N.N.* **2009**, *9*, 6401.

54. Murawala, P.; Phadnis, S. M.; Bhonde, R. R.; Prasad, B. L. V. *Colloids Surf. B: Biointerfaces.* **2009**, *73*, 224.

55. Zhang, L. Z.; Yu, J. C.; Yip, H. Y.; Li, Q.; Kwong, K. W.; Xu, A. W.; Wong, P. K. *Langmuir.* **2003**, *19*, 10372.

56. Fadley, C. S.; Shirley, D. A. *J. Res. Natl. Bur. Stand.,* **1970**, *74*, 543.

57. Singh, S.; D'Britto, V.; Prabhune, A. A.; Ramana, C. V.; Dhawan, A.; Prasad, B. L. V.; *New J. Chem.* **2010**, *34*, 294.

58. Blanch, E. W.; Hecht, L.; Barron, L. D. *Methods.* **2003**, *29*, 196.

59. Urabe, H.; Sugawara, Y.; Ataka, M.; Rupprecht, A. *Biophy. J.* **1998**, *74*, 1533.

60. Ionov, R.; Hedoux, A.; Guinet, Y.; Bordat, P.; Lerbret, A.; Affouard, F.; Prevost, D.; Descamps, M. In *5th International Discussion Meeting on Relaxations in Complex Systems* Lille, France, **2005**, p 4430-4436.

61. Grabbe, E. S.; Buck, R. P. *J. Am. Chem. Soc.* **1989**, *111*, 8362.

62. Brunner, H.; H., S. *Biochimica et Biophysica Acta (BBA)-Protein Structure.* **1972**, *271*, 16.

63. Ishizaki, H.; Balaram, P., Ed. *Biophys. J.* **1981**, *36*, 509.

64. Nabiev, I. R.; Savchenko, V. A.; Efremov, E. S. *J. Raman. Spec.* **1983**, *14*, 375.

65. Singh, S.; Patel, P.; Jaiswal, S.; Prabhune, A. A.; Ramana, C. V.; Prasad, B. L. V. *New J. Chem.* **2009**, *33*, 646.

66. Wang, W.; Chen, X.; Efrima, S. *J. Phy. Chem. B.* **1999**, *103*, 7238.
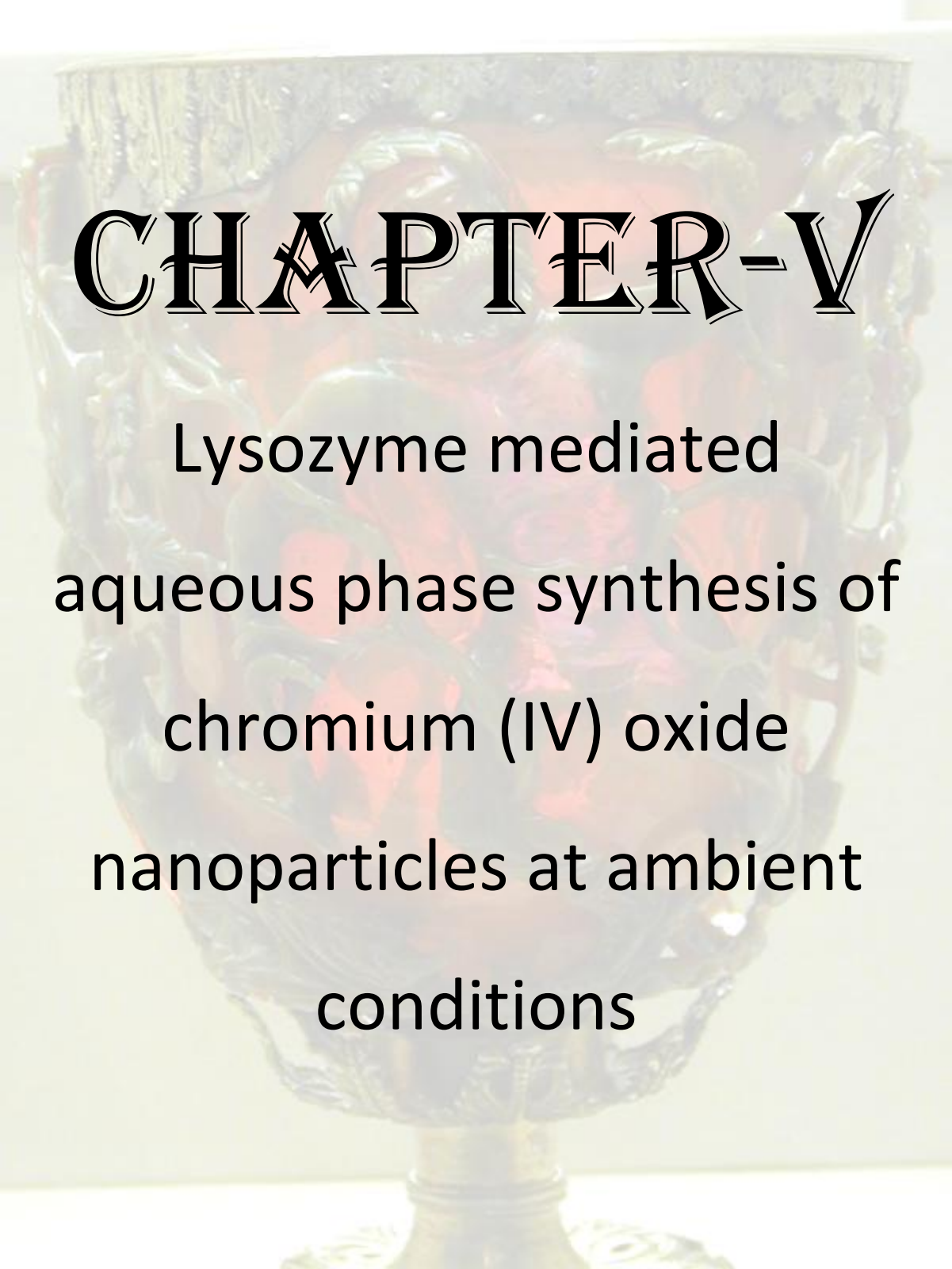
CHAPTER-V

Lysozyme mediated

aqueous phase synthesis of

chromium (IV) oxide

nanoparticles at ambient

conditions

Lysozyme mediated aqueous phase synthesis of chromium (IV) oxide nanoparticles under ambient conditions
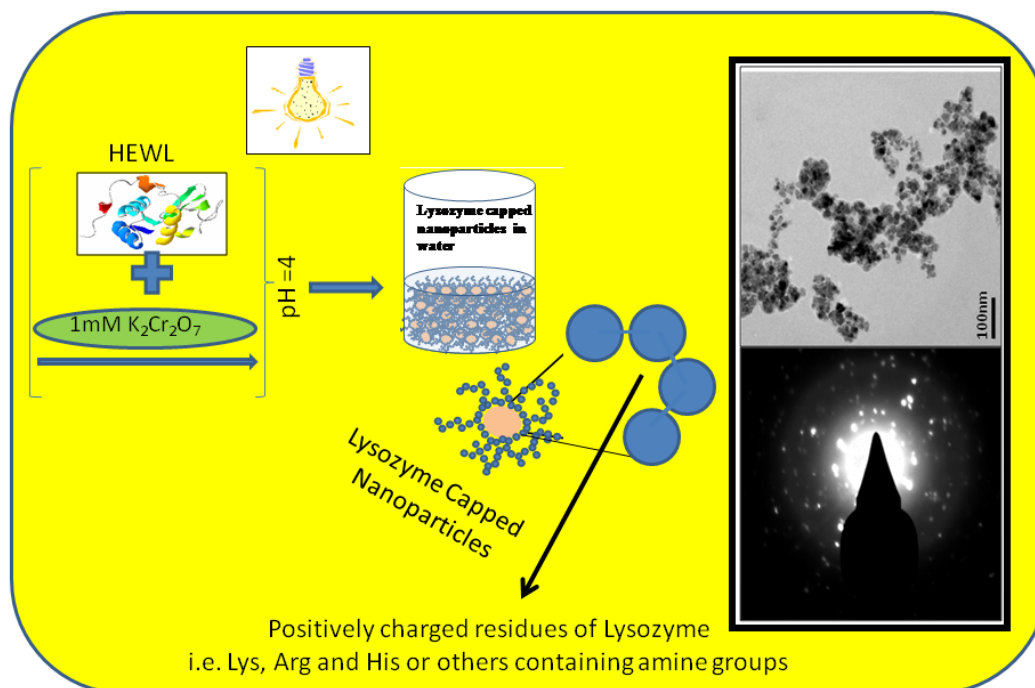
Biomimetic synthesis is a powerful tool for the synthesis of nanomaterials with complex shape, hierarchical organization and controlled size, shape and polymorph under ambient conditions in aqueous environments. Increased understanding of biomineralization mechanisms has greatly enhanced the possibilities of biomimetic mineralization approaches to synthesize new materials. Biological materials naturally display a variety of functional structures highly organized at the nanoscale. Various bioassemblies have been shown to be template for complex, multidimensional inorganic nanoarchitectures that are typically not available by conventional synthetic methodologies. In addition to the various naturally occurring templates, the powerful techniques developed in life sciences are interesting tools for engineering approaches towards material science. Besides structural and morphological control during synthesis, biotemplating procedures may add another dimension to inorganic materials such as biofunctionality. Here in this chapter lysozyme mediated synthesis of chromium (IV) oxide at ambient conditions is discussed where lysozyme is acting both as capping as well as reducing agent. The chromium dioxide nanoparticles prepared by this method are smaller than 10 nm and shows paramagnetic behaviour.

5.1 Inrtoduction

Study of interaction between proteins and inorganic materials has been the focus of research in various fields, e.g. biomedicine, biochemistry, biophysics, and materials chemistry. Materials can be synthesized using either physical, chemical or biological route, however biological synthesis is gaining popularity among scientists because of various advantages like green approach, size control, synthesis of unstable phases under ambient conditions which are difficult to stabilize by other routes without using higher temperature or pressure. Micro-organisms synthesize highly organized inorganic materials with remarkable properties by uptake of the necessary precursors from the local environment followed by incorporation into functional structures and materials under ambient conditions. Although the mechanisms of in vivo crystallization processes are often not known fully at the molecular level, proteins play a key role in the formation of inorganic matter. However, this in vivo synthesis is typically limited to certain materials e.g. magnetite, silica, or calcium carbonate. Biomineralization-based techniques have emerged as alternative to traditional materials syntheses as they offer ambient fabrication conditions with high degree of compositional specificity. Biomolecules, such as proteins, peptides and single-stranded DNA, are some of the most underused, yet powerful and versatile building blocks[1–3]. Their molecular recognition properties are unmatched to conventional synthetic analogues[4]. So far, many smart inorganic materials have been prepared, which include virus-based synthesis of magnetic and semiconducting nanowires[5], bacterial surface layers as template for the synthesis of CdS superlattices[6], DNA assisted synthesis of gold particle nanowires[7], and biotemplate synthesis of metal nanowires[8]. Fully investigating and exploiting these selective biomolecules might be of great importance in the development of novel materials, especially in the areas of medicine and nanotechnology[9,10]. Nowadays scientists are using known biomineralization agents to fabricate non-natural compositions of materials. A typical example of this is the use of silicateins, which were isolated from the sponge *Tethya aurantia* catalytically produce SiO_2,[11] Anatase phase TiO_2[12] and $GaOOH$[13]. This example demonstrates the possible generality of the enzymatic methods for metal oxide material production. Similarly Feldheim and colleagues, reported the production of metal oxide nanomaterials, TiO_2 and SiO_2, from the non-material based proteases, papain and trypsin[14]. Both enzymes possess a catalytic triad that is

similar to that of silicatein-α, with papain possessing a cysteine and trypsin possessing a serine at the active site. Synthesis of TiO_2 was possible using either of the enzymes whereas SiO_2 was synthesized from papain only. These results are surprising as papain, with a cysteine at the active site can produce SiO_2 while trypsin, whose active site more closely mimics that of silicatein, cannot. Results obtained so far implies that the positioning of the active site with respect to the solution and the materials precursors may play an important role. Presence of highly exposed active site to drive non-specific reactions may be required to allow for efficient materials processing[15]. Some of the sequence characteristics native to biomineralizing proteins are also present in proteins, such as hen egg white lysozyme (HEWL) or bovine serum albumin (BSA), making them popular candidates for biomimetic studies[16-28]. Hen egg white lysozyme possesses an excess of positively charged residues, making it an adequate analog to the Long Chain Poly Amines or the R5 peptide. Indeed, HEWL has found application in the synthesis of silica, as well as titania (a nonbiogenic material).[23-25] Besides lysozyme, a variety of other commercially available enzymes, including R-amylase and pepsin, have been utilized as templates for the production of nanomaterials[26,29]. Inspired by the variety of proteins present in nature, we chose lysozyme (hen egg white) as a model system to synthesize chromium (IV) oxide nanoparticles to understand the mechanism of interaction. Lysozyme is a protein with relatively high stability and is responsible for breaking down the polysaccharide walls of many types of bacteria.[30] Furthermore it has also been confirmed that it shows chelating interactions with metal ions[31-32]. Thus it is reasonable to expect the function of lysozyme in the formation of inorganic nanomaterials. This protein has also been found to be a new morphology-directing agent to direct the growth of single crystal bismuth sulfide and oxide nanowires. Although the exact mechanism of the reactions is not well known, there is no doubt that the bio-molecules used must have played an important role in the formation of the one dimensional (1D) nanostructures. The biomolecules, irrespective of whether they are sugars or protein, peptide and amino acids have several functional groups such as –OH, $-NH_2$, and –COOH, which have strong coordination ability toward the inorganic ions. These bio-molecules might react with inorganic species through the functional groups to form special intermediates, and then direct the growth and/or the assembly of the 1D nanostructures by their special structures. For example starch molecules have been reported to be chain like structures with many hydroxyl (–OH)

groups on their surfaces[33,34]. During the synthesis of Te nanowires, these –OH groups might react with TeO_4^{2-} groups through hydrogen bonds to form chain like intermediate compounds. Thus the long chains of starch could serve as directing template for the growth of tellurium nanowires. This biomolecule-assisted method expands the application of biomolecules to the green synthesis of other nanostructures and could promise for extension to topologically more intricate structures in addition to the generation of other 1D nanomaterials. Lysozyme has not been so far used that profoundly in aqueous phase synthesis of nanomaterials except few[35-38]. Here we report the lysozyme mediated aqueous phase synthesis of Chromium (IV) oxide nanoparticles which are smaller than 10 nm and show paramagnetism at lower temperature. Chromium (IV) oxide is unique rutile-type transition metal dioxides[39] which exhibits ferromagnetic (Tc = 395 K) and metallic properties[40]. These properties make this oxide the most desirable material for magnetic recording medium in the form of tapes. The chromium ions in CrO_2 are in the Cr^{+4} state with a magnetic moment of $2\mu_B$ per ion. The two $3d$ electrons occupy spin-split $t2g$ subbands, one localized and the other in a half-filled band. They are strongly coupled by the on-site exchange interaction JH ~1 eV^{41}. Surface of CrO_2, generally has a native oxygen rich layer of thermodynamically stable Cr_2O_3 which is generally few atomic layer thick[42]. Cr_2O_3 orders antiferromagnetically below 307 K^{43}. The characterization of native oxide Cr_2O_3 surface layer on CrO_2 films by Cheng *et al* revealed that CrO_2 might polarize the Cr_2O_3 layer[44]. The native Cr_2O_3 surface layer acts as a tunnel barrier[45] and is useful for applications with desirable magneto transport properties. At the temperature higher than 288°C, CrO_2 start decomposing into the Cr_2O_3[40].

5.2 Materials and methods

Chemicals: Lysozyme was purchased from Sigma-Aldrich Inc. This protein was used as received through out nanoparticles synthesis. Potassium dichromate ($K_2Cr_2O_7$) was purchased from S. D. fine-chemicals India and used as received.

UV-Visible Spectroscopy measurement. Ultraviolet-visible absorbance was recorded on a Jasco UV-vis-NIR (Model V570) dual beam spectrophotometer operated at a resolution of 2 nm.

Fourier transform infrared spectroscopy (FTIR). Fourier Transform Infra red Spectroscopy (FTIR) was carried out on a Perkin–Elmer Spectrum One instrument operated in the diffuse reflectance mode at a resolution of 2 cm^{-1}. To obtain good signal to noise ratio, 128 scans of the film were taken in the range $450 – 4000$ cm^{-1}.

X ray Diffraction pattern (XRD). Powder XRD patterns were recorded using PHILIPS X'PERT PRO instrument equipped X'celerator, a fast solid-state detector on drop-coated sample on glass substrate. The sample was scanned using X'celerator with a total number of active channels of 121. Iron-filtered Cu Kα radiation (λ=1.5406 Å) was used. XRD patterns were recorded in the 2θ range of 20°- 80°.

Thermogravimetric analysis (TGA) and DTA. Thermogravimetric analysis (TGA) for lysozyme synthesized CrO_2 was performed on Q5000 V2.4 Build 223 instrument by applying scan rate 10°C min^{-1} in presence of air.

X-ray photoemission spectroscopy (XPS). X-ray photoelectron spectroscopy (XPS) for nanoparticles were performed on VG MicroTech ESCA 3000 instrument at a pressure <1x10^{-9} Torr with an overall resolution of 1 eV. The spectra was recorded with unmonochromatic Mg K alpha radiation (photon energy = 1253.6 eV) at a pass energy of 50 eV and electron take off angle (angle between electron emission direction and surface plane) of 60°.

Transmission Electron Microscopy (TEM) measurements. Determination of nanoparticle shape and size were performed on FEI, Technai F30, electron microscope (TEM) operated at an accelerating voltage of 300 kV. For this purpose, samples were prepared by drop-coating the particles suspended in aqueous medium on carbon coated copper grids. Selected area electron diffraction (SAED) analysis was carried-out on the same grids.

Magnetic measurement. For magnetization vs. magnetic field measurements, we used a Physical Property Measurement System (PPMS) from Quantum Design Inc., San Diego, CA., equipped with a 7 T superconducting magnet and a vibrating sample magnetometer operating at 40 Hz.

5.3 Results and discussion

5.3.1 Synthesis of lysozyme capped chromium (IV) oxide nanoparticles. 10 mM of $K_2Cr_2O_7$ was added to aqueous solution (3mg/ml) of

lysozyme at pH= 4.5 so that the effective concentration of $K_2Cr_2O_7$ in the reaction mixture becomes 1mM . This solution was incubated at a temperature of 40°C for three days. The reaction mixture was centrifuged at 12000 rpm for 20 minutes. The pellet collected was used for further characterization of materials.

5.3.2 UV-visible absorption spectroscopy measurements

First evidence for the formation of nanoparticles was seen in UV-visible absorption spectra which indicates the appearance of absorption bands at ~ 350 nm which is absent in case of precursor $K_2Cr_2O_7$ as shown in figure 5.1.
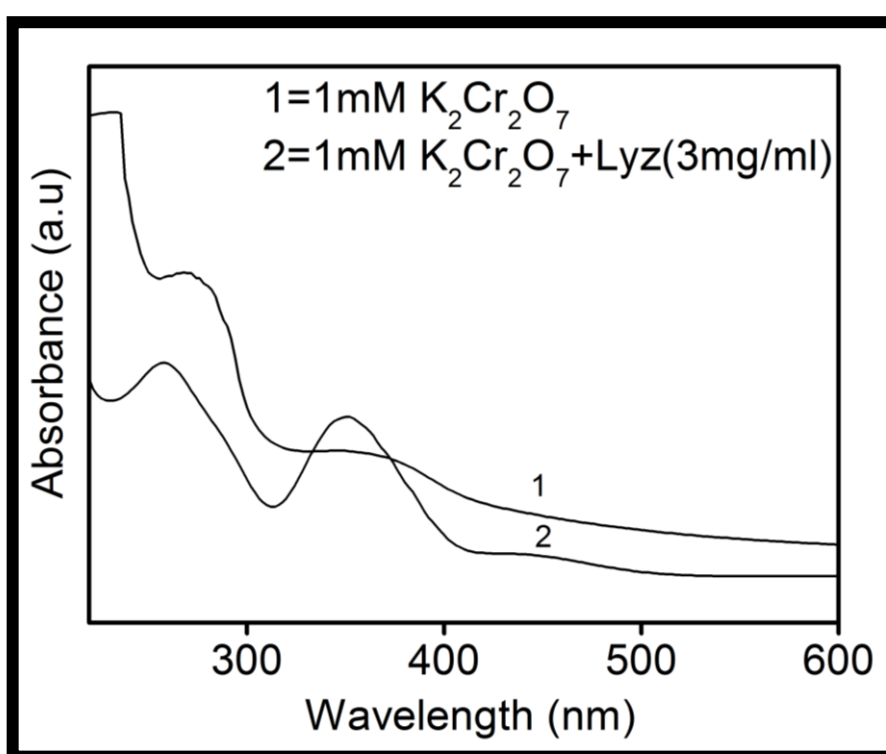

Figure 5.1: UV-visible absorption spectroscopy for precursor salt (1) and precursor with 3mg/ml lysozyme (2)

5.3.3 FTIR spectroscopy measurements

To determine which phase (oxide) of chromium oxide was formed, Fourier Transform Infrared Spectroscopy (FTIR) measurements were recorded. Further to investigate the presence of stretching/vibration bands present in Chromium oxide species lysozyme capped nanoparticles were drop casted on silicon wafer and measurements were taken in diffuse reflectance mode. Occurrence of bands at ~ 900 cm^{-1} in case of curve 3 indicates the presence of OCrO species in the sample as

shown in figure-5.2. It should be noted here that this band is absent in other two curves ($K_2Cr_2O_7$-1 and lysozyme-2). However it is necessary to ascertain which of the chromium oxides (CrO_2, CrO_3, Cr_2O_3) is responsible for the band in this region. In literature it is reported that in between ~ 900-1000 cm^{-1} along with CrO_2 other
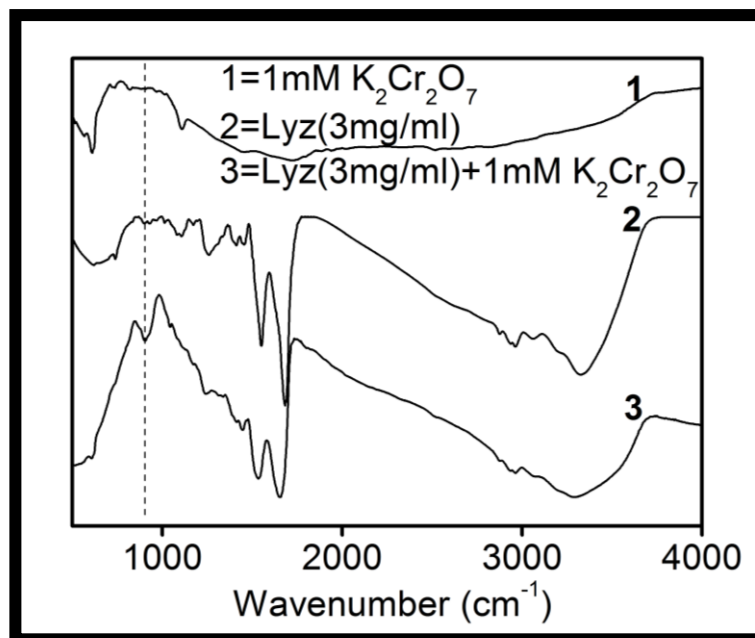

Figure 5.2: FTIR spectra of Precursor (1), lysozyme (2) and lysozyme capped CrO$_2$ nanoparticles (3)

oxides of chromium e.g. CrO_3, Cr_2O_3 also show bands in this region[46]. Therefore it is difficult to establish CrO_2 among different oxides of chromium on the basis of FTIR data only.

5.3.4 X-ray diffraction spectra analysis

To determine the crystallinity of CrO_2 nanoparticles XRD studies were performed on as-synthesized nanoparticles. The room-temperature XRD pattern obtained from as-synthesized nanoparticle shows tetragonal phase having cell parameter a= b=4.419, c=2.915, $\alpha= \beta=\gamma=90^o$ with space group P42mnm is shown in figure-5.3. The CrO_2 particles tends to develop 1-3 nm thick layer of more stable Cr_2O_3 layer which can not be picked up by the XRD data.[47] Further to confirm that the peaks shown in lysozyme capped CrO_2 is because of the diffraction from CrO_2 nanoparticles, room temperature XRD pattern of precursors i.e. lysozyme and $K_2Cr_2O_7$ was also collected to compare with the standard CrO_2 material as reported in PCPDF database (figure-

5.3). From figure-5.3 it can be clearly seen that the peaks observed in lysozyme capped CrO_2 nanoparticles are not present in precursors.
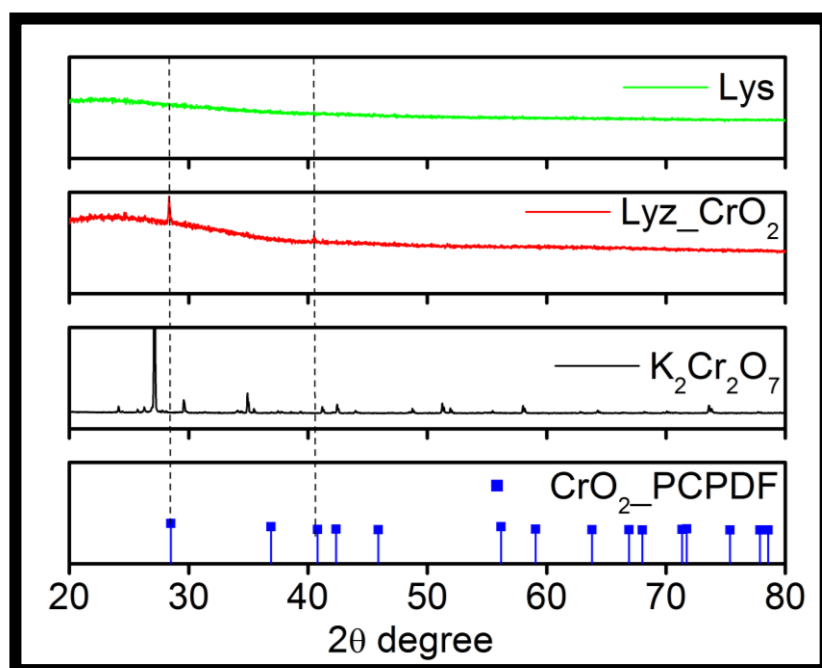

Figure 5.3: X-ray diffraction (XRD) pattern of crystalline CrO₂ nanoparticles synthesized by lysozyme at different concentration (1&2), precursor salt (3) and bulk CrO₂ as reported in PCPDF Database

5.3.5 X-ray Photo-electron Spectroscopy (XPS) measurements:

To determine the purity of these nanoparticles X-ray photoelectron spectroscopy (XPS) measurements were recorded. As-obtained XPS core level spectra were background corrected using the Shirley algorithm and chemically distinct species were resolved using a nonlinear least squares fitting procedure. The core level binding energies (B.E.) were aligned with the carbon binding energy of 285 eV. Background corrected XPS spectra for lysozyme capped CrO_2 nanoparticles, commercially available Cr_2O_3 and $K_2Cr_2O_7$ were shown in figure 5.4. XPS spectra of Cr2p can be split into two curves due to spin orbital splitting i.e. $Cr2p^{1/2}$ aand $Cr2p^{3/2}$ at a binding energy of 585.8 eV and 575.9 eV respectively corresponding to CrO_2 which matches with its reported literature value[48]. An additional peak is observed at a binding energy of 577.3 eV which could be due to presence of Cr (III) species found in $Cr(OH)_3$[49]. It is clearly observed in figure 5.4 that the intensity of Cr (IV)

peak is more compared to Cr (III) peak implying that Cr (IV) species is formed as major product along with Cr (III) species. Since CrO_2 is difficult to stabilize in air/water where oxygen is present in abundance, there is always a possibility of formation of few atomic layers of Cr_2O_3 at the surface which is also
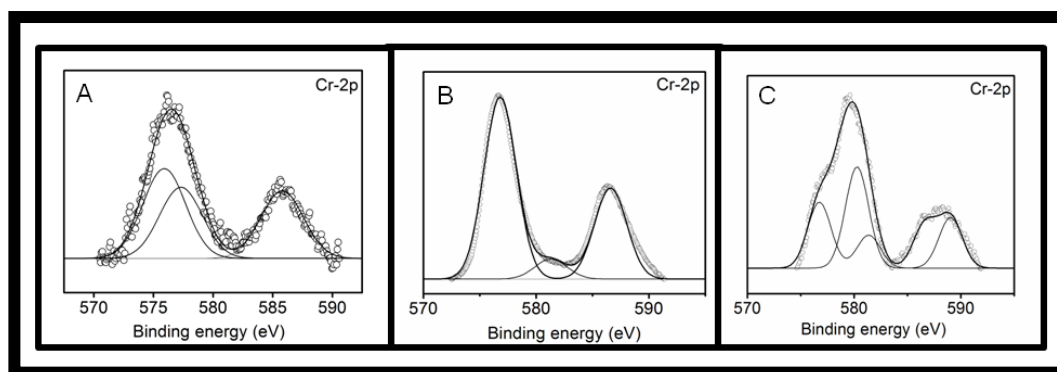

Figure 5.4: Graph showing X-ray photoelectron spectra (XPS) of Cr-2p species present in CrO₂ nanoparticles synthesized by lysozyme (A), commercially available Cr₂O₃ (B) and K₂Cr₂O₇(C)

thermodynamically more stable at room temperature[42]. Unfortunately it is very difficult to distinguish Cr_2O_3 from CrO_2 on the basis of XPS only because both of them give peaks at approximately same binding energy[47]. Further to check the presence of Cr_2O_3 in the sample (lysozyme capped CrO_2 nanoparticles), background corrected XPS spectra of Cr-2p present in commercially available Cr_2O_3 and the precursor used ($K_2Cr_2O_7$) was also plotted as shown in figure 5.4. From the figures it can be clearly stated that most of the peaks corresponding to Binding energies of 576.8, 581.6 and 586.7 eV are common in both panel (B) and (C) but none of the peaks present in panel (A) are found in either panel (A) or (B). This suggests that lysozyme capped nanoparticles is indeed chromium (IV) oxide with some impurities of other oxides of Chromium i.e $Cr(OH)_3$[49]. It is interesting to note that the chromium (IV) 2p peaks for CrO_2 do not follow a simple trend of increasing BE with increasing formal oxidation state. These effects have been attributed to differences in the crystal structure, ionic character, and electronic properties of these oxides[50].

5.3.5 Thermal measurements

Thermogravimetric analysis (TGA) of as-synthesized CrO_2 nanoparticles is shown in figure 5.5. As pointed out earlier the as-synthesized nanoparticles are capped with

lysozyme that prevent them from aggregation. The presence of this coating even after intense centrifugation is proven by the observation of almost 80% weight-loss during heating the particles up to 700 °C, which is attributed to the loss of moisture and biomolecules bound on the nanoparticle surface. Weight loss shown in figure 5.5 is a multi step process. First loss starts at beginning and continues up to 280 °C and is
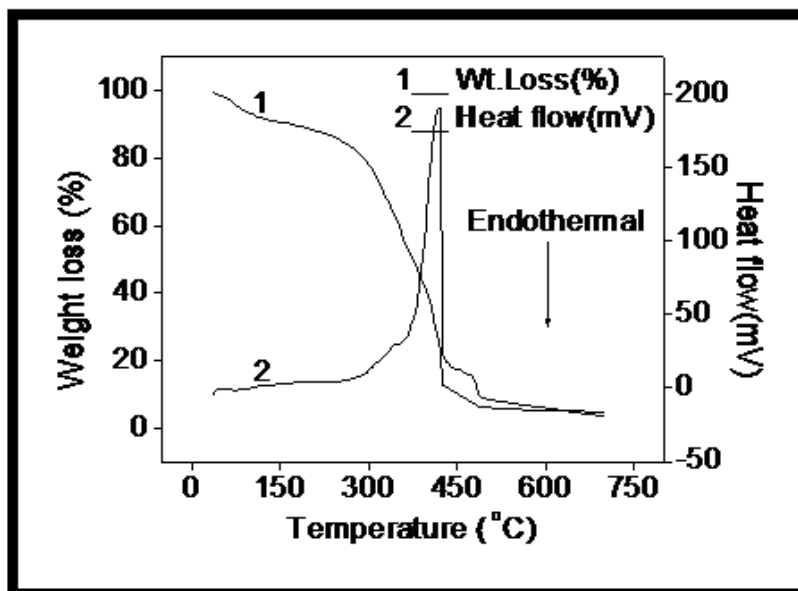

Figure 5.5: Graph showing TGA-DTA curve of lysozyme capped crystalline CrO₂ nanoparticles

attributed to the complete loss of moisture and partial removal of biomolecules (lysozyme). Second major weight loss starts at around 300 °C and continues up to 420 °C. This loss is also marked by appearance of an sharp exothermic peak (as shown by Differential Thermal Analysis curve) corresponding to rutile phase conversion of CrO_2 to corundum phase Cr_2O_3. The temperatures and profiles of these exotherms varied with the heating rate[51,52]. Above 420 °C third weight loss was observed which is attributed to complete decomposition of CrO_2 to Cr_2O_3.

5.3.6 Differential scanning calorimetry (DSC) measurements

To confirm the phase purity of lysozyme capped CrO_2 nanoparticles DSC measurements were performed on these as synthesized particles. As temperature increases at constant rate there is endothermic removal of moisture till 120 °C as

shown in figure 5.6. Further as heating continues biomolecules present on the surface of CrO_2 nanoparticles start degrading. At temperature around (280-320) °C, strong endothermic peak attributing to phase conversion of CrO_2 into Cr_2O_3 was observed. Around 400 °C it shows the occurrence of exothermic peak indicating the decomposition of CrO_2 into Cr_2O_3 which was also observed in TGA curve. These measurements were done in presence of nitrogen (inert atmosphere). It is interesting to note that Curie temperature (T_c) around 120 °C was not observed in the DSC curve because the lysozyme capped nanoparticles were very small (less than 10 nm) and showed paramagnetic behaviour as discussed in magnetic measurement results.
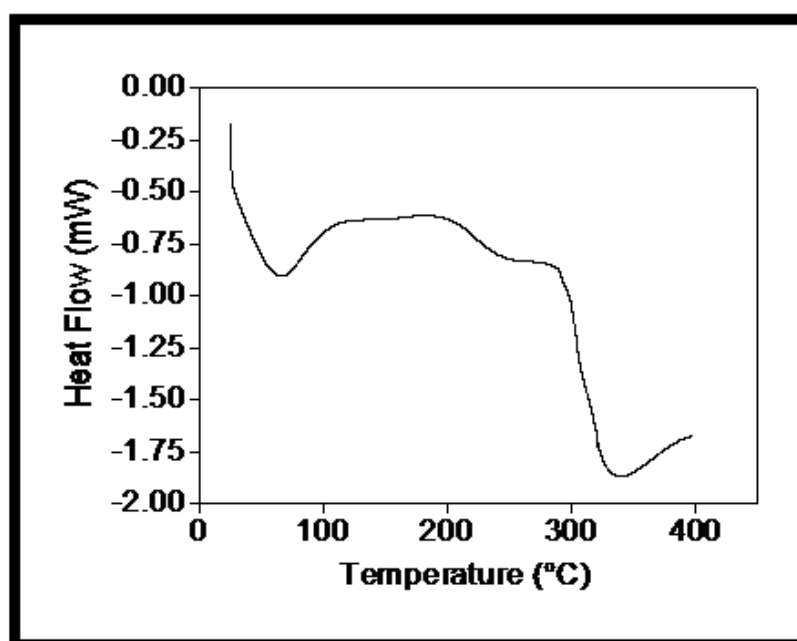

Figure 5.6: DSC curve of lysozyme capped crystalline CrO₂ nanoparticles

5.3.7 Transmission electron microscopic analysis

Finally to determine the shape, size and crystallinity of lysozyme capped CrO_2 nanoparticles, transmission electron microscopy analysis was performed on drop casted carbon coated, copper TEM grids. Electron micrograph shown in figure 5.7 suggests, that these particles are clusters of small nanoparticles which are polycrystalline in nature as evident from the diffraction image which sows combination of diffuse ring and dot pattern (SAED). These clusters are approximately 10 nm or less than that and are irregular in shape.
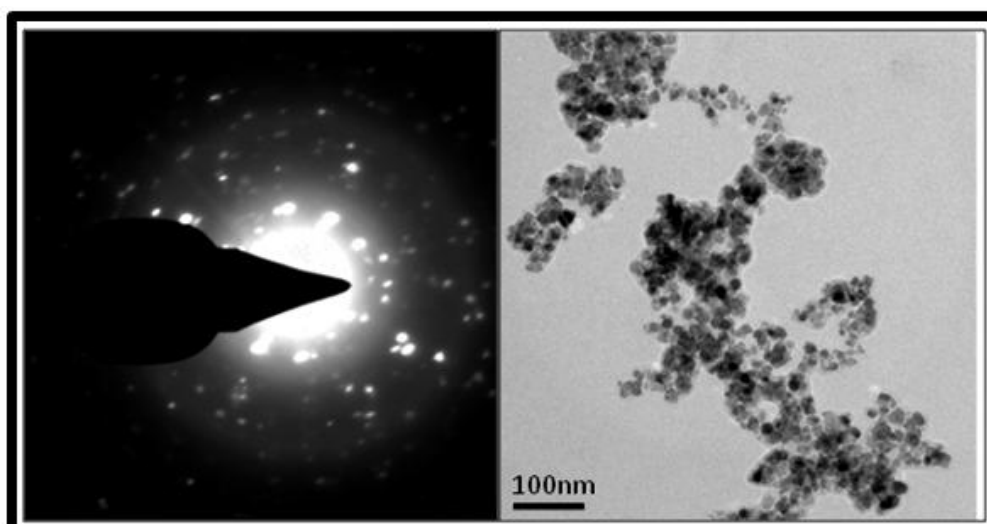
Figure 5.7: Transmission electron micrograph showing SAED (Selected Area Electron Diffraction) and its corresponding images of lysozyme capped crystalline CrO$_2$ nanoparticles

5.3.8 Magnetic measurements

To probe the magnetic property of the lysozyme capped CrO$_2$ particles we performed field dependence of magnetization at 5 K. M-H loop show that magnetization does not saturate up to 50 kOe magnetic field because this magnetic field is too low to saturate the magnetization (figure 5.7). No opening up of M-H loop at low temperature indicates the superparamagnetic nature of the sample. As seen from the TEM image the crystallite are very small in size and they agglomerate to form the larger clumps. The small crystallite below single domain size of the particles may be responsible for the superparamagnetic nature of the sample[53].
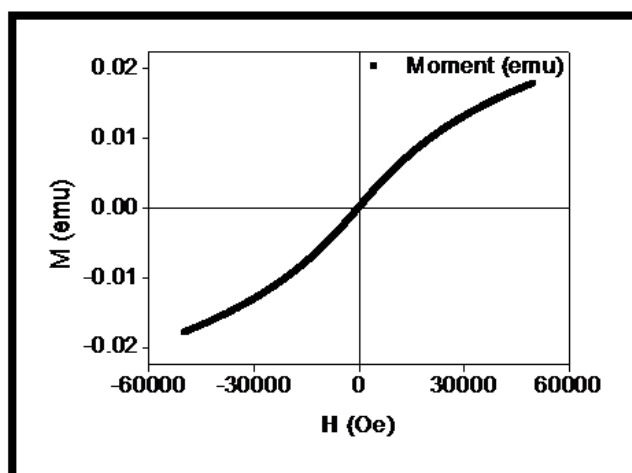

Figure 5.7: Magnetization versuss magnetic field measurements of lysozyme capped CrO$_2$ nanoparticles at 5 K

5.4 Conclusion

A simple facile method has been developed for the aqueous phase synthesis of Chromium (IV) oxide nanoparticles utilizing the chelation and complexation abilities of amino acids present in the lysozyme. Being metastable it is very difficult to stabilize pure CrO_2 in water. Since these nanoparticles are very small in size (<10 nm) and they are passivated with thick layer of protein (lysozyme), as indicated by thermo gravimetric studies (TGA), it is very difficult to get magnetic signals without diamagnetic background. Chromium (IV) oxide is unique rutile-type transition metal dioxides which exhibits ferromagnetic (Tc = 395 K) and metallic properties. These nanoparticles cannot be heated to remove proteins because the Curie temperature for CrO_2 is very low i.e. 288°C. Other way is to remove these background signals manually after magnetic measurements. Here in this chapter we have reported the lysozyme mediated aqueous phase synthesis of mixed phase of chromium oxide comprising CrO_2 and $Cr(OH)_3$ with Chromium (III) oxide present mainly on the surface. Here lysozyme is acting both as capping as well as reducing agent. These nanoparticles show paramagnetic behaviour.

5.5 References

1. Hartgerink, J. D.; Beniash E.; Stupp, S. I. *Science.* **2001**, *294*, 1684.

2 . Dujardin, E.; Hsin, L. B.; Wang, C.R.C.; Mann, S. *Chem. Commun.* **2001**, 1264.

3. Lee, S. W.; Mao, C. B.; Flynn, C. E.; Belcher, A. M. *Science.* **2002**, *296*, 892.

4. Mirkin, C. A.; Taton, T. A. *Nature.* **2000**, *408*, 626.

5. Mao, C.; Solis, D. J.; Reiss, B. D.; Kottmann, S. T.; Sweeney, R. Y.; Hayhurst, A.; Georgiou, G.; Iverson, B.; Belcher, A. M. *Science.* **2004**, *303*, 213.

6. Shenton, W.; Pum, D.; Sleytr, U. B.; Mann, S. *Nature.* **1997**, *389*, 585.

7. Patolsky, F.; Weizmann, Y.; Lioubashevski, O.; Willner, I. *Angew. Chem. Int. Ed.* **2002**, *41*, 2323.

8. Knez, M.; Bittner, A. M.; Boes, F.; Wege, C.; Jeske, H.; MaiB, E.; Kern, K. *Nano Lett.* **2003**, *3*, 1079.

9. Storhoff, J. J.; Lazarides, A. A.; Mucic, R. C.; Mirkin, C. A.; Letsinger, R. L.; Schatz, G. C. *J. Am. Chem. Soc.* **2000**, *122*, 4640.

10. Niemeyer, C. M.; Adler, M.; Gao, S.; Chi, L. *Angew. Chem. Int. Ed.* **2000**, *39*, 3055.

11. Cha, J. N.; Shimizu, K.; Zhou, Y.; Christiansen, S. C.; Chmelka, B. F.; Stucky, G. D. Morse, D. E. *Proc. Natl. Acad. Sci. U. S. A.* **1999**, *96*, 361.

12. Sumerel, J. L.; Yang, W. ; Kisailus, D.; Weaver, J. C.; Choi, J. H.; Morse, D. E. *Chem. Mater.* **2003**, *15*, 4804.

13. Kisailus, D.; Choi, J. H.; Weaver, J. C.; Yang, W.; Morse, D. E. *Adv. Mater.* **2005**, *17*, 314.

14. Smith, G. P.; Baustian, K.; Ackerson, C. J.; Feldheim, D. L. *J. Mater. Chem.* DOI:10.1039/b909286b.

15. Marc R. Knecht. *J. Mater. Chem.* **2009**, *19*, 8276.

16. Baeuerlein, E. *Biomineralization., Progress in Biology, Molecular Biology, and Application*; Wiley-VCH Verlag GmbH & Co. KGaA:Weinheim, Germany, **2004**.

17. Baeuerlein, E. *Handbook of Biomineralization, Biological Aspects and Structure Formation*; Wiley-VCH Verlag GmbH & Co. KGaA: Weinheim, Germany, **2007**.

18. Sumper, M.; Kroger, N. *J. Mater. Chem.* **2004**, *14*, 2059.

19. Muller, W. E. G.; Belikov, S. I.; Tremel, W.; Perry, C. C.; Gieskes, W. W. C.; Boreiko, A.; Schroder, H. C. *Micron.* **2006**, *37*, 107.

20. Muller, W. E. G.; Krasko, A.; Le Pennec, G.; Schroder, H. C. *Microsc. Res. Tech.* **2003**, *62*, 368.

21. Weaver, J. C.; Morse, D. E. *Microsc. Res. Tech.* **2003**, *62*, 356.

22. Yang, L.; Xing, R.; Shen, Q.; Jiang, K.; Ye, F.; Wang, J.; Ren, Q. *J.Phys. Chem. B.* **2006**, *110*, 10534.

23. Coradin, T.; Coupe´, A.; Livage, J. *Colloids Surf. B.* **2003**, *29*, 189.

24. Shiomi, T.; Tsunoda, T.; Kawai, A.; Mizukami, F.; Sakaguchi, K. *Chem. Mater.* **2007**, *19*, 4486.

25. Luckarift, H. R.; Dickerson, M. B.; Sandhage, K. H.; Spain, J. C. *Small* **2006**, *2*, 640.

26. Rangnekar, A.; Sarma, T. K.; Singh, A. K.; Deka, J.; Ramesh, A.; Chattopadhyay, A. *Langmuir.* **2007**, *23*, 5700.

27. Brelle, M. C.; Torres-Martinez, C. L.; McNulty, J. C.; Mehra, R. K.; Zhang, J. Z. *Pure Appl. Chem.* **2000**, *72*, 101.

28. Xie, J.; Lee, J. Y.; Wang, D. I. C. *J. Phys. Chem. C* **2007**, *111*, 10226.

29. Chiu, T. C.; Chiou, S. H.; Hsieh, M. M.; Chen, Y. T.; Chang, H. T. *J. Nanosci. Nanotechnol.* **2005**, *5*, 2128.

30. Kimball, J. W. Biology, 6th, Addison-Wesley Pub. Co.,**1994**.

31. Sesta, B.; Gente, G.; Iovino, A.; Laureti, F.; Michiotti, P.; Paiusco, O.; Palacios, A. C.; Persi, L.; Princi, A.; Sallustio, S.; Sarnthein-Graf, C.; Capalbi, A.; Mesa, C. L. *J. Phys. Chem. B.* **2004**, *108*, 3036.

32. Mehta, S. B.; Shah, M. L. *Asian J. Chem.* **2002**, *14*, 236.

33. Kimball JW (1994) Biology, 6th edn. Addison-Wesley Publishing Company, Mass., USA.

34. Hu HW (1990) Organic chemistry, 2nd edn. High Education Publisher, Beijing, China.

35. Luckarift, H. R.; Dickerson, M. B.; Sandhage, K. H.; Spain, J. C. *small*. **2006**, *2*, 640.

36. Gao, F.; Lu, Q.; Komarneni, S. *Chem. Comm.* **2005**, 531.

37. Eby, D. M.; Schaeublin, N. M.; Farrington, K. E.; Hussain, S. M.; Johnson, G. R. *ACS Nano*. **2009**, *3 (4)*, 984.

38. Das, R.; Jagannathan, R.; Sharan, C.; Kumar, U.; Poddar, P. *J. Phys. Chem. C*, **2009**, *113 (52)*, 21493.

39. Rogers, D. B.; Shannon, R. D.; Sleight, A. W.; Gillson, J. L. *Inorg.Chem.* **1969**, *8*, 841.

40. Chamberland, B. L.; CRC *Crit. Rev. Solid State Mater. Sci.* **1977**, *7*, 1.

41. Gupta, A.; Li, X. W.; Xiao, G. *J. Appl. Phys.* 1 May **2000**, Vol. 87, No. 9.

42. Robbert, P. S.; Geisler, H.; Ventrice, C. A.; Van Ek, J.; Chaturvedi, S.; Rodriguez, J. A.; Kuhn, M.; Diebold, U. *J. Vac. Sci. Technol. A.* **1998**. *16*, 990.

43. Brand, E.; Kellett, D.; Enever, M. D.; Fellows, J. T.; Egdell, R. G. *J. Mater. Chem.* **2005**, *15*, 1141.

44. Cheng, R.; Xu, B.; Borca, C. N.; Sokolov, A.; Yang, C. S.; Yuan, L.; Liou, S. H.; Doudin, B.; Dowben, P. A. *Appl. Phys. Lett.* **2001,** *79*, 3122.

45. Hwang, H. Y.; Cheong, S. W. *Science* **1997,** *278*, 1607.

46. Jeiowska-Trzebiatowska, B.; Hanuza, J.; Wojciechowski, W.; Nawojska, J. *Inorganica Chimica Acta.* June, **1968**.

47. Dai, J.; Tang, J.; Xu, H.; Spinu, L.; Wang, W.; Wang, K.; Kumbhar, A.; Li, M.; Diebold, U. *Appl. Phys. Lett.* **2000**, *77*, No. 18.

48. Wagner, C.D.; Moulder, J.F.; Davis, - L.E.; Riggs, W.M. Perking-Elmer Corporation, Physical Electronics Division.

49. Stypula, B.; Stoch, J. *Corrosion Science*, **1994**, *36*, 2159.

50. Hanafi, Z. M.; Ismail, F. M.; Mohamed, A. K. Z. *Phys. Chem.*(Munich) **1996**, *194*, 61.

51. Richardson, R. T. *J. Mater. Sc. Letts.* **1989**, *8*, 1264.

52. Chen, Y.J.; Zhang, X. Y.; Li, Z. Y. *Chemical Physics Letters.* **2003**, *375*, 213.

53. Cullity, B. D.; Graham, C. D. Introduction to magnetic materials, *John Wiley & Sons*, Inc., Publication.
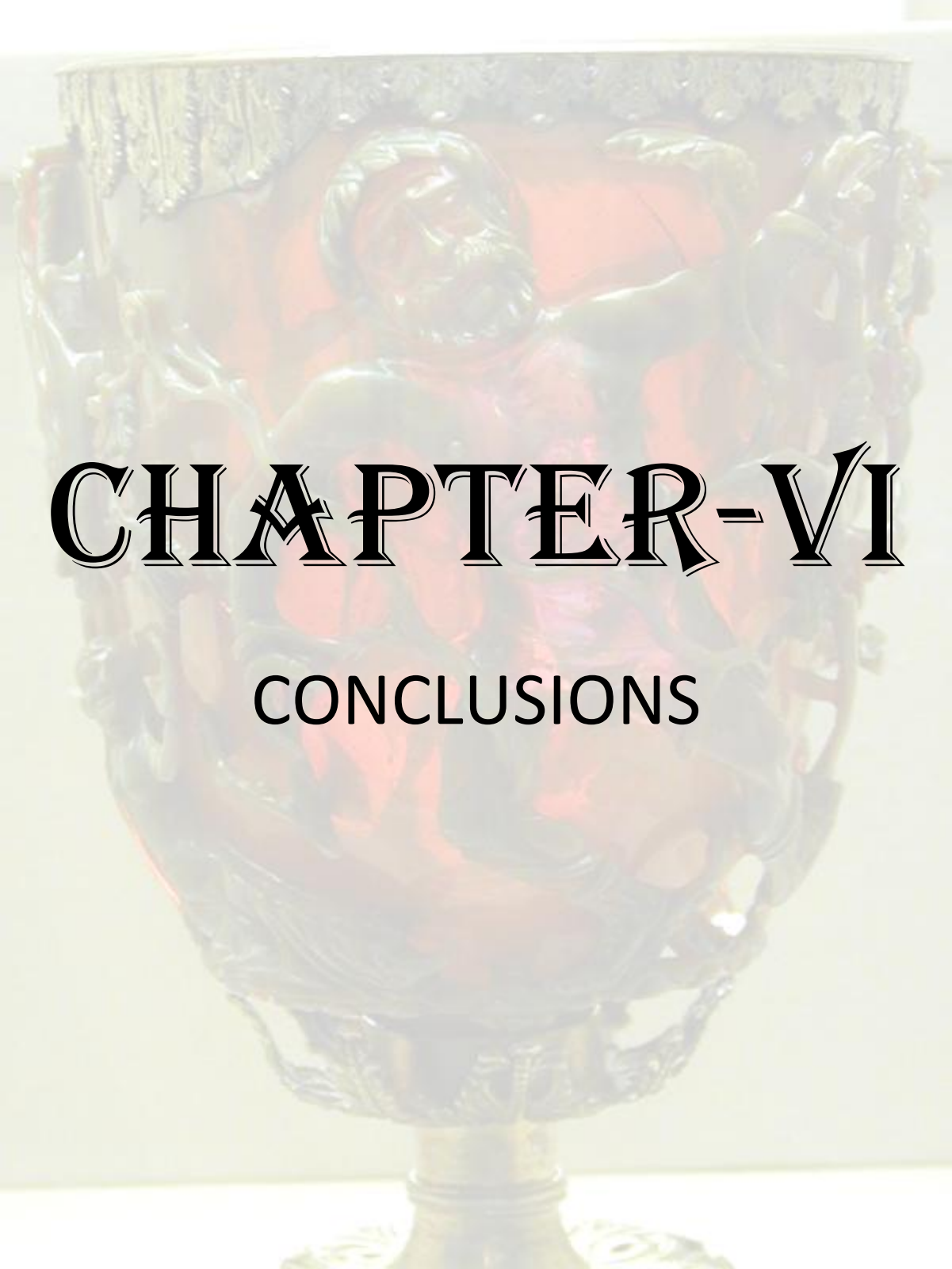
CHAPTER-VI

CONCLUSIONS

Conclusions

(Images courtesy: Various sources at http://images.google.com)

This chapter contains conclusions of the salient features of the work described in this thesis and the scope for future potential developments in this field**.**

6.1 Summary of the work

Nature provides inspiration for designing materials and systems, which derive their functions from highly organized structures. Biological hard tissues are hybrid materials having both inorganics within a complex organic matrix, the molecular scaffold controlling inorganic structures. Biocomposites incorporate both biomacromolecules such as proteins, lipids and polysaccharides, and inorganic materials, such as hydroxyapatite, silica, magnetite and calcite. The ordered organization of hierarchical structures in organisms begins via the molecular recognition of inorganics by proteins that control interactions and followed by the highly efficient self-assembly across scales. Following the molecular biological principle, proteins could also be used in controlling materials formation in practical engineering via self-assembled, hybrid, functional materials structures. In molecular biomimetics, material-specific peptides could be the key in the molecular engineering of biology-inspired materials. With the recent developments of

nanoscale engineering in physical sciences and the advances in molecular biology, we now combine genetic tools with synthetic nanoscale constructs to create a novel methodology. We first tactfully select and/or design peptides with specific binding to functional solids, tailor their binding and assembly characteristics, develop bifunctional peptide/protein constructs with both material binding and biological activity, and use these as molecular synthesizers, erectors and assemblers.

In this thesis, we have described the bioinspired synthesis of metal/metal-oxide nanomaterials. We observe that the marine isolate i.e *Brevibacterium casei* on exposure to 1mM cobalt acetate extracellularly forms 6 nm, spinnel structure, ferromagnetic Co_3O_4 nanoparticles passivated by proteins of microbial origin. During this synthesis process Scanning Electron Microscopy real time kinetics revealed that these bacteria tend to aggregate or form clusters and this tendency increases gradually until 72 h compared to control cells where individual cells are clearly visible even after 72 h. We attributed this behaviour to a kind of stress response where many bacterial strains produce excess extracellular exopolysaccharide, slime, or form capsule to protect themselves against metal ions. Further SDS PAGE analysis revealed that there were over expression of two proteins in treated bacterial cells which corresponds to ∼ 30 and 65 kDa, belonging to oxido-reductase family of enzymes. Here we report for the first time that Co^{2+} was supplied to the bacterial system in the form of cobalt acetate, but the nanoparticles formed showed the presence of both Co^{2+} and Co^{3+}ions. Such type of oxidation/reduction mechanism has been reported for other metals as well; for example arsenite oxidase converts As(III) to As(V) and arsenate reductase converts As(V) to As(III).

After biochemical analysis we were interested in determining the biophysical properties of these bacterial cells during synthesis of nanoparticles. For this we have used Atomic Force Microscopy which is a very sensitive surface technique. We performed force-distance spectroscopy measurements on these cells to obtain information like changes in the surface-topography, surface-adhesion, indentation-depth, and Young's modulus of a metal-tolerant marine bacterium, *Brevibacterium casei* after the exposure to the Co^{2+} during biosynthesis of nanoparticles. Significant changes in the morphology as well as elastic and adhesive properties of the *Brevibacterium casei* where an increase in the adhesive properties and the

indentation depth of the bacterial surfaces and a decrease in the cell stiffness after several hours of exposure to the cobalt acetate was observed.

In most of the microbial syntheses either some enzymes or biomolecules are involved. Therefore we have chosen hen egg white lysozyme to synthesize metal/metal-oxide nanoparticles. We developed a simple facile method for synthesis of metal nanoparticles (gold and silver) utilizing the reduction abilities of amino acids present in the lysozyme. Our experimental results prove that hydroxyl groups in tyrosine residues and the amine group in tryptophan residues were found to be responsible for silver and gold nanoparticles formation respectively. Formation of gold nanoparticles was assisted by silver through galvanization/transmetallation reaction. Further by controlling the availability of tyrosine and tryptophan in lysozyme by treatment with amino acid specific chemical regents we could precisely control the size of nanoparticles. Further our *invitro* results prove that gold nanoparticles prepared by this method are biocompatible and retain antibacterial property. We have also shown the use of Surface Enhanced RAMAN spectroscopy to precisely determine the functional groups responsible in the surface capping of gold and silver nanoparticles synthesized by the hen egg white- lysozyme.

Further we have extended the same method to synthesize metastable CrO_2 in aqueous phase. Being metastable we got mixed phase comprising CrO_2 and $Cr(OH)_3$, with Chromium (III) oxide present mainly on the surface.. We can say that a simple facile method has been developed for the aqueous phase synthesis of Chromium (IV) oxide nanoparticles utilizing the chelation and complexation abilities of amino acids present in the lysozyme. These nanoparticles are smaller than 10 nm and shows paramagnetic behaviour.

6.2 Scope for future work

One of the most challenging aspects of microbial synthesis of nanomaterials is to identify the proteins/enzymes and their corresponding DNA fragment which actually governs the biochemical pathway. This would lead to synthesis of respective nanomaterials in bulk quantity and thus biotechnologists would be able to fulfil the industrial needs.

The Atomic Force Microscopy measurements can be done under physiological conditions in fluid cell to give a more accurate and real picture of changes in the nanomechanical properties of bacterial cells due to interaction with metal ions. Similar force spectroscopy measurements can be performed on mammalian cells to see the effect of nanoparticles/metal ions on them. This kind of information is very useful for biological application purpose.

Further lysozyme mediated synthesis approach that we have used for synthesizing metal/metal-oxide nanoparticles can be extended for synthesizing metal alloys (Au-Ag) or core shell particles which has got different properties and application. Similarly lysozyme mediated synthesis can be tried at different temperature to see its shape and size controlling properties.

Invio toxicity studies of nanomaterials can be done in order to put forth well-accepted mechanism which can be developed into technology.

Annexure-I

Composition of culture media

Zobell medium

Ingredients	Gms / Litre
Peptic digest of animal tissue	5.000
Yeast extract	1.000
Ferric citrate	0.100
Sodium chloride	19.450
Magnesium chloride	8.800
Sodium sulphate	3.240
Calcium chloride	1.800
Potassium chloride	0.550
Sodium bicarbonate	0.160
Potassium bromide	0.080
Strontium chloride	0.034
Boric acid	0.022
Sodium silicate	0.004
Ammonium nitrate	0.0016
Disodium phosphate	0.008
Sodium fluorate	0.0024
Final pH	(at 25°C) 7.6±0.2

Phylogenetic tree
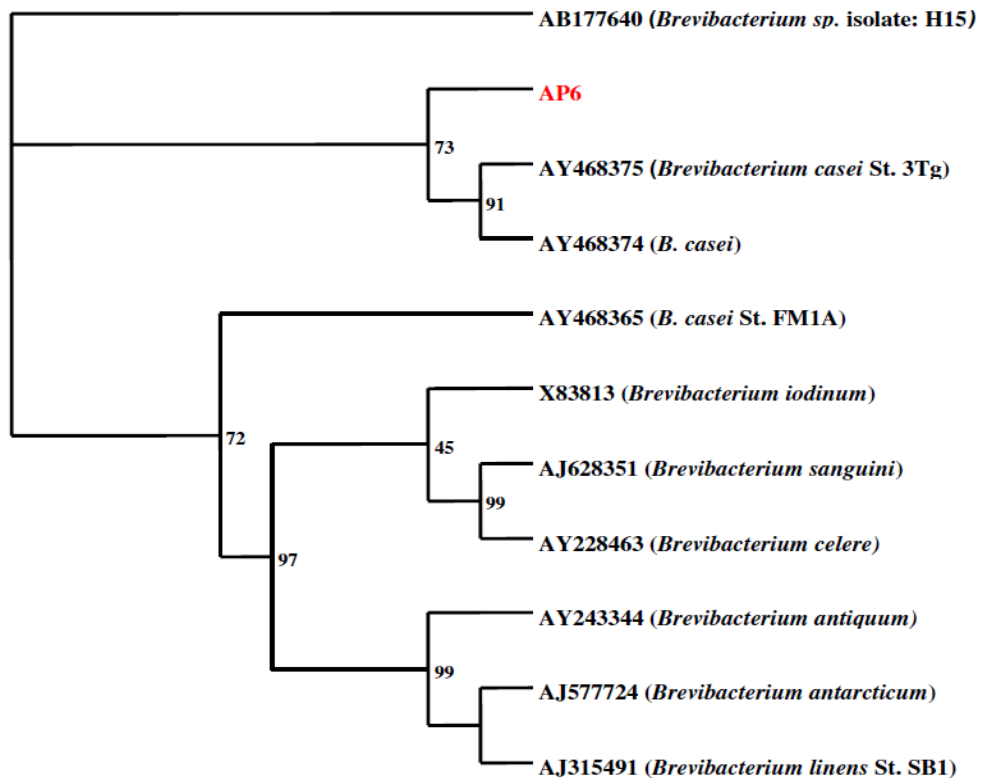
Annexure-II

Medium used for cytotoxicity assay: (DMEM)

Composition of Dulbecco's Modified Eagle Medium (DMEM)

Ingredients   g/l

Glucose   4.5

L-Glutamine   Traces

Sodium bicarbonate   3.7

Sodium pyruvate: 3.7

Annexure-III

LIST OF PUBLICATIONS

- Extracellular Bacterial Synthesis of Protein Functionalized Ferromagnetic Co_3O_4 Nanocrystals and Imaging of Self-Organization of Bacterial Cells under Stress after Exposure to Metal Ions. *Chem. Mater.* **2008,** *20,* 1484–1491.

- Real-Time Nanomechanical and Topographical Mapping on Live Bacterial Cells *Brevibacterium casei under Stress Due to Their Exposure to Co^{2+} Ions during* Microbial Synthesis of Co_3O_4 Nanoparticles. *J. Phys. Chem. B **2009, 113, 7927– 7933**.*

- Mechanistic Study of Surface Functionalization of Enzyme Lysozyme Synthesized Ag and Au Nanoparticles Using Surface Enhanced Raman Spectroscopy. *J. Phys. Chem. C, **2009, 113, 21493–21500.***

- Human Blood Vessel–Derived Endothelial Progenitors for Endothelialization of Small Diameter Vascular Prosthesis. *PLoS ONE,* **2009**, 11 e7718.

- Biomimetic approach towards size controlled synthesis of biocompatible antibacterial metal nanoparticles in aqueous phase using lysozyme. (Communicated)

- Lysozyme mediated aqueous phase synthesis of CrO_2 nanoparticles. (Communicated)